NORTH WEST SHELF
JOINT ENVIRONMENTAL
MANAGEMENT STUDY

Biogeochemical modelling of Australia's North West Shelf

NWSJEMS
TECHNICAL REPORT No. 8

- M. Herzfeld
- J. Parslow
- P. Sakov
- J. Andrewartha

June 2006

CSIRO

GOVERNMENT OF WESTERN AUSTRALIA
Department of Environment

National Library of Australia Cataloguing-in-Publication data:

Biogeochemical modelling of Australia's North West Shelf.

Bibliography.
Includes index.
ISBN 1 921061 56 1 (pbk.).

1. Biogeochemical cycles - Western Australia - North West Shelf. I. Herzfeld, M. (Michael), 1966- . II. CSIRO. Marine and Atmospheric Research. North West Shelf Joint Environmental Management Study. III. Western Australia. (Series : Technical report (CSIRO. Marine and Atmospheric Research. North West Shelf Joint Environmental Management Study) ; no. 8).

577.7099413

Biogeochemical modelling of Australia's North West Shelf.

Bibliography.
Includes index.
ISBN 1 921061 57 X (CD-ROM).

1. Biogeochemical cycles - Western Australia - North West Shelf. I. Herzfeld, M. (Michael), 1966- . II. CSIRO. Marine and Atmospheric Research. North West Shelf Joint Environmental Management Study. III. Western Australia. (Series : Technical report (CSIRO. Marine and Atmospheric Research. North West Shelf Joint Environmental Management Study) ; no. 8).

577.7099413

Biogeochemical modelling of Australia's North West Shelf.

Bibliography.
Includes index.
ISBN 1 921061 58 8 (pdf).

1. Biogeochemical cycles - Western Australia - North West Shelf. I. Herzfeld, M. (Michael), 1966- . II. CSIRO. Marine and Atmospheric Research. North West Shelf Joint Environmental Management Study. III. Western Australia. (Series : Technical report (CSIRO. Marine and Atmospheric Research. North West Shelf Joint Environmental Management Study) ; no. 8).

577.7099413

NORTH WEST SHELF
JOINT ENVIRONMENTAL
MANAGEMENT STUDY

Final report

North West Shelf Joint Environmental Management Study Final Report.

List of technical reports

NWSJEMS Technical Report No. 1
Review of research and data relevant to marine environmental management of Australia's North West Shelf.
A. Heyward, A. Revill and C. Sherwood

NWSJEMS Technical Report No. 2
Bibliography of research and data relevant to marine environmental management of Australia's North West Shelf.
P. Jernakoff, L. Scott, A. Heyward, A. Revill and C. Sherwood

NWSJEMS Technical Report No. 3
Summary of international conventions, Commonwealth and State legislation and other instruments affecting marine resource allocation, use, conservation and environmental protection on the North West Shelf of Australia.
D. Gordon

NWSJEMS Technical Report No. 4
Information access and inquiry.
P. Brodie and M. Fuller

NWSJEMS Technical Report No. 5
Data warehouse and metadata holdings relevant to Australia's North West Shelf.
P. Brodie, M. Fuller, T. Rees and L. Wilkes

NWSJEMS Technical Report No. 6
Modelling circulation and connectivity on Australia's North West Shelf.
S. Condie, J. Andrewartha, J. Mansbridge and J. Waring

NWSJEMS Technical Report No. 7
Modelling suspended sediment transport on Australia's North West Shelf.
N. Margvelashvili, J. Andrewartha, S. Condie, M. Herzfeld, J. Parslow, P. Sakov and J. Waring

NWSJEMS Technical Report No. 8
Biogeochemical modelling on Australia's North West Shelf.
M. Herzfeld, J. Parslow, P. Sakov and J. Andrewartha

NWSJEMS Technical Report No. 9
Trophic webs and modelling of Australia's North West Shelf.
C. Bulman

NWSJEMS Technical Report No. 10
The spatial distribution of commercial fishery production on Australia's North West Shelf.
F. Althaus, K. Woolley, X. He, P. Stephenson and R. Little

NWSJEMS Technical Report No. 11
Benthic habitat dynamics and models on Australia's North West Shelf.
E. Fulton, B. Hatfield, F. Althaus and K. Sainsbury

NWSJEMS Technical Report No. 12
Ecosystem characterisation of Australia's North West Shelf.
V. Lyne, M. Fuller, P. Last, A. Butler, M. Martin and R. Scott

NWSJEMS Technical Report No. 13
Contaminants on Australia's North West Shelf: sources, impacts, pathways and effects.
C. Fandry, A. Revill, K. Wenziker, K. McAlpine, S. Apte, R. Masini and K. Hillman

NWSJEMS Technical Report No. 14
Management strategy evaluation results and discussion for Australia's North West Shelf.
R. Little, E. Fulton, R. Gray, D. Hayes, V. Lyne, R. Scott, K. Sainsbury and D. McDonald

NWSJEMS Technical Report No. 15
Management strategy evaluation specification for Australia's North West Shelf.
E. Fulton, K. Sainsbury, D. Hayes, V. Lyne, R. Little, M. Fuller, S. Condie, R. Gray, R. Scott,
H. Webb, B. Hatfield, M. Martin, and D. McDonald

NWSJEMS Technical Report No. 16
Ecosystem model specification within an agent based framework.
R. Gray, E. Fulton, R. Little and R. Scott

NWSJEMS Technical Report No. 17
Management strategy evaluations for multiple use management of Australia's North West Shelf
– Visualisation software and user guide.
B. Hatfield, L. Thomas and R. Scott

NWSJEMS Technical Report No. 18
Background quality for coastal marine waters of the North West Shelf, Western Australia.
K. Wenziker, K. McAlpine, S. Apte, R.Masini

CONTENTS

ACRONYMS

ACRONYMS

ACOM	Australian Community Ocean Model
AFMA	Australian Fisheries Management Authority
AFZ	Australian Fishing Zone
AGSO	Australian Geological Survey Organisation now Geoscience Australia
AHC	Australian Heritage Commission
AIMS	Australian Institute of Marine Science
AMSA	Australian Maritime Safety Authority
ANCA	Australian Nature Conservation Agency
ANZECC	Australian and New Zealand Environment and Conservation Council
ANZLIC	Australian and New Zealand Land Information Council
APPEA	Australian Petroleum, Production and Exploration Association
AQIA	Australian Quarantine Inspection Service
ARMCANZ	Agricultural Resources Management council of Australia and New Zealand
ASIC	Australian Seafood Industry Council
ASDD	Australian Spatial Data Directory
CAAB	Codes for Australian Aquatic Biota
CAES	Catch and Effort Statistics
CALM	Department of Conservation and Land Management (WA Government)
CAMBA	China Australia Migratory Birds Agreement
CDF	Common data format
CITIES	Convention on International Trade in Endangered Species
CTD	conductivity-temperature-depth
CMAR	CSIRO Marine and Atmospheric Research
CMR	CSIRO Marine Research
COAG	Council of Australian Governments
ConnIe	Connectivity Interface
CPUE	Catch per unit effort
CSIRO	Commonwealth Science and Industrial Research Organisation
DCA	detrended correspondence analysis
DIC	Dissolved inorganic carbon
DISR	Department of Industry, Science and Resources (Commonwealth)
DEP	Department of Environmental Protection (WA Government)
DOM	Dissolved organic matter
DPIE	Department of Primary Industries and Energy
DRD	Department of Resources Development (WA Government)
EA	Environment Australia
EEZ	Exclusive Economic Zone
EIA	Environmental Impact Assessment
EPA	Environmental Protection Agency
EPP	Environmental Protection Policy
ENSO	El Nino Southern Oscillation
EQC	Environmental Quality Criteria (Western Australia)
EQO	Environmental Quality Objective (Western Australia)
ESD	Ecologically Sustainable Development
FRDC	Fisheries Research and Development Corporation
FRMA	Fish Resources Management Act
GA	Geoscience Australia formerly AGSO
GESAMP	Joint Group of Experts on Scientific Aspects of Environmental Protection
GIS	Geographic Information System
ICESD	Intergovernmental Committee on Ecologically Sustainable Development
ICS	International Chamber of Shipping
IOC	International Oceanographic Commission
IGAE	Intergovernmental Agreement on the Environment
ICOMOS	International Council for Monuments and Sites
IMO	International Maritime Organisation
IPCC	Intergovernmental Panel on Climate Change

IUNC	International Union for Conservation of Nature and Natural Resources
IWC	International Whaling Commission
JAMBA	Japan Australian Migratory Birds Agreement
LNG	Liquified natural gas
MarLIN	Marine Laboratories Information Network
MARPOL	International Convention for the Prevention of Pollution from Ships
MECO	Model of Estuaries and Coastal Oceans
MOU	Memorandum of Understanding
MPAs	Marine Protected Areas
MEMS	Marine Environmental Management Study
MSE	Management Strategy Evaluation
NCEP - NCAR	National Centre for Environmental Prediction – National Centre for Atmospheric Research
NEPC	National Environmental Protection Council
NEPM	National Environment Protection Measures
NGOs	Non government organisations
NRSMPA	National Representative System of Marine Protected Areas
NWQMS	National Water Quality Management Strategy
NWS	North West Shelf
NWSJEMS	North West Shelf Joint Environmental Management Study
NWSMEMS	North West Shelf Marine Environmental Management Study
ICIMF	Oil Company International Marine Forum
OCS	Offshore Constitutional Settlement
PFW	Produced formation water
P(SL)A	Petroleum (Submerged Lands) Act
PSU	Practical salinity units
SeaWiFS	Sea-viewing Wide Field-of-view Sensor
SOI	Southern Oscillation Index
SMCWS	Southern Metropolitan Coastal Waters Study (Western Australia)
TBT	Tributyl Tin
UNCED	United Nations Conference on Environment and Development
UNCLOS	United Nations Convention of the Law of the Sea
UNEP	United Nations Environment Program
UNESCO	United Nations Environment, Social and Cultural Organisation
UNFCCC	United Nations Framework Convention on Climate Change
WADEP	Western Australian Department of Environmental Protection
WADME	Western Australian Department of Minerals and Energy
WAEPA	Western Australian Environmental Protection Authority
WALIS	Western Australian Land Information System
WAPC	Western Australian Planning Commission
WHC	World Heritage Commission
WOD	World Ocean Database
www	world wide web

TECHNICAL SUMMARY

A numerical biogeochemical model was applied to the North West Shelf to investigate the primary productivity dynamics of the region. A subsurface chlorophyll *a* maximum (SCM) of 1 to 1.5 mg Chl*a* m^{-3} was found below the mixed layer at depths of approximately 70 m. Surface concentrations of chlorophyll and nitrate were low. The SCM is maintained by a balance between nitrate uptake by phytoplankton, fed by nitrate fluxes into the SCM, and nitrate export in particulate form. The depth of the SCM is where phytoplankton can minimise growth by minimising light and nitrate limitation. The SCM will relocate closer to the surface as light availability decreases or the nitrogen flux increases, and vice versa. Also, any change in the grazing of zooplankton on phytoplankton results in a change in the SCM depth, where increased grazing leads to a shallower SCM.

The flux of nitrogen into the SCM was primarily due to vertical processes, with vertical diffusion responsible for the largest background flux of nitrate. Vertical advection can locally increase nitrate supply into the SCM. Horizontal fluxes of nitrate do not directly contribute to the supply of nitrate into the SCM, but are important in maintaining a high concentration pool of nitrate at depth.

Variability of the SCM occurs on timescales of the spring neap tide. Surface chlorophyll concentration is highest in an offshore band and during spring tides when mixing is more vigorous the chlorophyll concentration in this band increases and its position moves further offshore. This is a combination of the SCM becoming shallower due to higher turbidity decreasing light availability, and larger bottom boundary layers creating deeper zones of surface to bottom mixing. Variability of the SCM is also observed on seasonal timescales. The SCM is more distinct with a surface signature closer inshore in the wet season, and more dispersed with surface signature offshore in the dry. The seasonal variability is attributed to changes in mixed layer depth resulting from atmospheric forcing.

The impact of the passage of a tropical cyclone (Tropical Cyclone Bobby, February, 1995) on the SCM was investigated. Primary productivity only increases by small amounts during such an event. Increased, deeper mixing due to the large wind stress and upwelling near the centre due to divergence competes with a deepening nutricline, resulting in little new nitrate brought to the surface. Subsequent to the cyclone passage, vertical motion of the nutricline at the near inertial period can lead to increases in nitrate concentration and productivity above and within the SCM. Greater increases are observed further offshore.

1. INTRODUCTION

A comprehensive review of the biochemistry of the North West Shelf (NWS) is presented by Heyward et al. (2006), including a summary of existing data sets related to primary productivity investigations. Research into the dynamics of primary and secondary productivity has been hampered by the lack of high frequency long term data records. Existing studies indicate that the standing crop of phytoplankton is nitrogen limited on the NWS, with the source of nitrate being nutrient rich water residing on the continental slope below the surface mixed layer. There exists very little nitrate in surface waters and terrestrial inputs are negligible. Enhanced productivity in the mixed layer is attributed to sub-pycnocline fluxes of nitrogen resulting from several processes, including upwelling on time scales of the semidiurnal tide to lower frequencies (>35 hours), horizontal and vertical mixing due to the barotropic tide and internal tide activity, and the effect of tropical cyclones (Holloway et al. 1985). It is rare for nitrate rich slope water to intrude onto the shelf further than the 50 m isobath as a result of these processes. These fluxes of nitrogen are roughly constant throughout the year.

Primary productivity resulting from these nitrogen fluxes is maximum in a subsurface chlorophyll maximum (SCM) at the base of the mixed layer or in the bottom mixed layer. However, inshore (<50 m depth) the SCM is not observed and the depth integrated standing crop is significantly less than offshore. Tidal mixing allows benthic biota to access this pool of phytoplankton over the shelf region. Surveys show a reasonable degree of coherence in the long-shore distribution of chlorophyll over the southern NWS (Tranter & Leech, 1987).

There exists a marked seasonality in the physics of the NWS due to the presence of the Leeuwin Current, which has maximum flows in the southern NWS from February to June (Holloway & Nye, 1985). This variability in the physics of the NWS is not mirrored in the phytoplankton distributions (Tranter & Leech, 1987). There is limited seasonal variability in the observed distribution of phytoplankton, which tend to be more vertically concentrated in summer and more dispersed in winter. The Leeuwin Current actually acts to damp any seasonal variability in nutrient supply by lowering the pycnocline in the winter (when stratification is weak and up slope intrusions would ordinarily be greatest) and thus inhibiting exchange of nutrient rich deep water with the surface. Vertical sections of density and nitrate across the shelf from near Port Hedland to 300 km offshore, derived from seasonal climatologies (Ridgway et al. 2002), for the maximum (May) and minimum (Dec) periods of Leeuwin Current flow are displayed in figures 1.1 to 1.4.

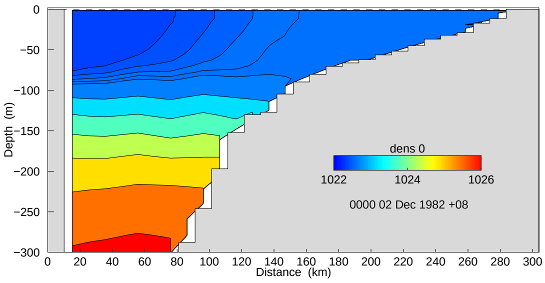

Figure 1.1: σ_t section (kg m^{-3}) December.

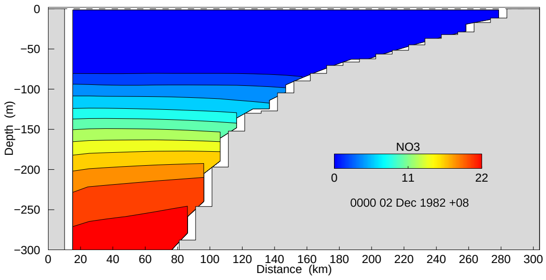

Figure 1.2: NO_3 section (μmol) December.

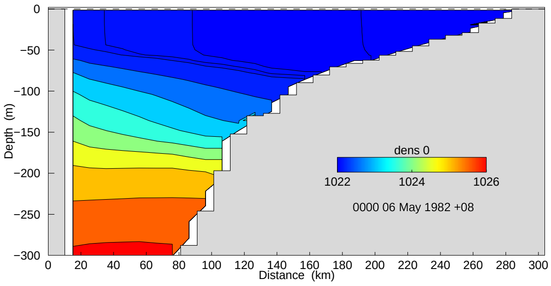

Figure 1.3: σ_t section (kg m^{-3}) May.

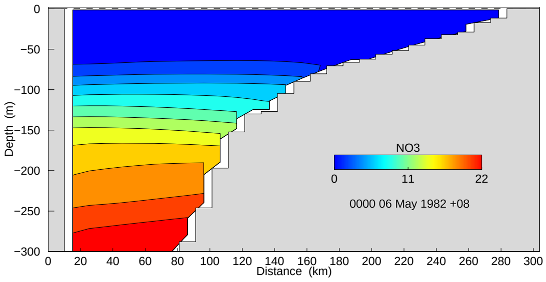

Figure 1.4: NO_3 section (μmol) May.

The May density section clearly shows the downwelling situation expected when the Leeuwin Current flows, where the isopycnals slope down towards the coast. The mixed layer is approximately 50 m deep in this case. The summer density sections exhibit an uplift of isopycnals over the slope region associated with weak upwelling, also displaying a much shallower pycnocline (e.g. the 1023.5 kg m^{-3} contour is almost 50 m shallower). Although the effect of the Leeuwin Current is clearly observed, the corresponding sections of nitrate do not show any intrusion of nutrient onto the shelf, presumably due to the moderating influence of the Leeuwin Current upon upwelling in the winter. Holloway and Nye (1985) suggest that weak upwelling is possible in both winter and summer as a result of southwesterly winds overcoming the steric height gradient associated with the dominant south-west flow, i.e. upwelling is a function of both wind strength and direction, and the strength of the Leeuwin Current. It is unlikely that these episodic events would be captured in the nitrate climatology, but they should, however, be captured in a dynamical model of the region. The nitrate sections also clearly exhibit the low levels of NO_3 in the surface layer and the very large concentrations at depth which act as the source of nitrogen in the region.

The lack of a highly resolved temporal and spatial data set for the NWS shelf region leaves many questions about nutrient cycling and primary productivity within the region unresolved. A numerical biogeochemical model is used here to investigate the primary productivity and nutrient cycling dynamics of the NWS region and provide insight into the key processes controlling the spatial and temporal patterns of primary production. Given the available data sets, only limited calibration of the model has been possible, and the model and conclusions should be regarded as preliminary in nature. Section 2 describes the model used and section 3 outlines how the model was implemented and calibrated. Various aspects of the results and dynamics are then discussed in section 4 followed by concluding remarks.

2. THE MODEL

The model used to investigate the primary productivity and nutrient dynamics on the NWS is a general dynamical process model of biogeochemical and ecological processes developed by CSIRO for estuaries and coastal waters. This model is based on the National Estuarine Audit Model (Baird et al. 2003), which in turn represents an extension of the Port Phillip Bay model (Murray & Parslow, 1999). The model represents the cycling of nitrogen, phosphorous and carbon through both pelagic and benthic ecosystems. The ecological model has three modules: water column, sediment (one layer), and epibenthos.

The water column module describes a simple planktonic food web. The model currently includes two phytoplankton functional groups: small phytoflagellates and large bloom-forming phytoplankton with nominal cell diameters of 5 µm and 20 µm respectively.

These classes can be considered to represent flagellates and diatoms. There are in turn two size classes of zooplankton (0.025 and 1 mm diameter) which graze respectively on small and large phytoplankton. The model represents a range of forms of nonliving particulate and dissolved organic matter, as well as inorganic nutrient species, dissolved inorganic carbon (DIC) and dissolved oxygen.

The sediment module represents the breakdown of particulate and dissolved organic matter through microbial and detritivore activity that consumes oxygen and releases DIC and inorganic nutrients. The sediment and water column modules include the processes of nitrification and denitrification.

The epibenthic module represents two functional classes of attached macrophytes: macroalgae, which take up nutrients from the water column, and seagrass, which take up nutrients from the sediment pore water. A schematic view of nitrogen cycling through water column, sediment and epibenthic components is shown in figure 2.1.

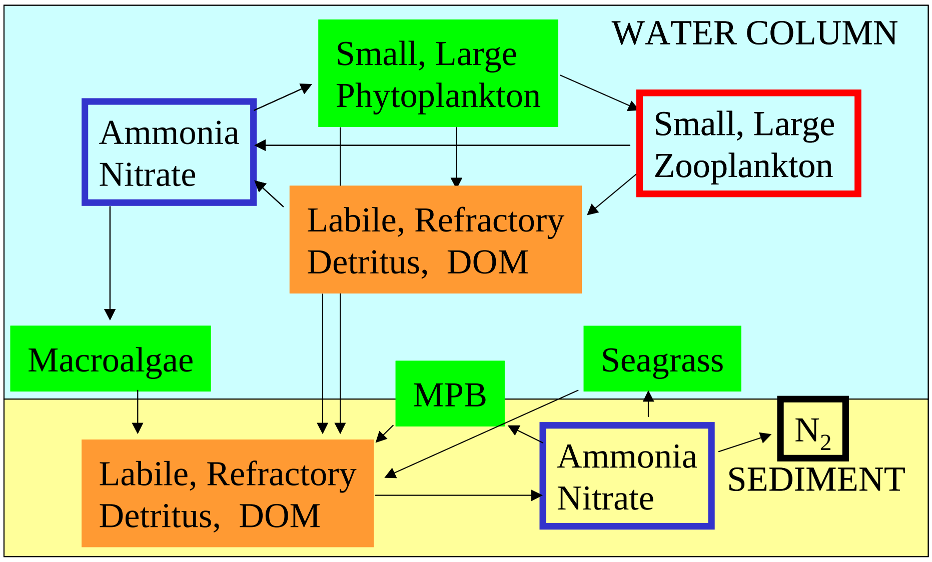

Figure 2.1: A schematic picture of nitrogen cycling in the model through pelagic, benthic and epibenthic components.

3. MODELLING STRATEGY

3.1 Approach

The area of the North West Shelf modelled focuses on the region from North West Cape to just north of Port Hedland. The continental shelf and slope are resolved throughout the domain (figure 3.1.1). The shelf is wide in the north-eastern section of the domain but becomes very narrow and steep near the southern boundary. The biogeochemical model is coupled directly to the hydrodynamic model, hence the spatial discretisation of the study region is identical to that used in the hydrodynamic model. The time-step used for the biochemical model is, however, different to the hydrodynamic model, and is typically longer. The equations representing the biochemical processes are integrated over the chosen time-step using an adaptive integration scheme suitable for stiff systems, which adjusts the number of sub-steps to achieve prescribed accuracy. While there are no stability restrictions on this time-step, time scales attributed to certain processes in the model must be resolved, which in practice places limitations on the maximum allowable time-step. The biogeochemical time-step used is one hour, as compared to 13 minutes and one minute for the baroclinic and barotropic hydrodynamic time-steps respectively.

The advantage of direct coupling of physics and biochemistry is that the advection and diffusion dynamics present can be applied directly to the biochemical state variables to obtain the transport of these components. This circumvents the need to approximate transports via inverse or other methods as is typically the case in box-type transport models. The disadvantage is that model performance can be an order of magnitude or more slower. This is a significant issue for biogeochemical models where large computational effort must be applied to model calibration. The original five kilometre resolution grid proposed for the hydrodynamic modelling proved too slow for biogeochemical simulations and resolution was decreased to 20 km in the long-shore direction and 10 km in the cross shore direction. This grid was still nested within the larger 10 by 10 km regional grid so that the hydrodynamic boundary conditions could be prescribed, and was subject to the same hydrodynamic forcing as the five kilometre resolution hydrodynamic grid. The 10 by 10 km regional grid was itself nested in a global circulation model ACOM3 (Australian Community Ocean Model, e.g. Schiller, 2004) so that basin scale motion was propagated into the region. Temperature and salinity solutions in the biogeochemical grid were relaxed to ACOM3 output with a relaxation time of 20 days. This allowed the density structure to retain the integrity of larger scale motions propagating into the grid (e.g. Leeuwin Current flows) and compensated for not explicitly imposing a surface heat flux. The grid nesting configuration used for the biogeochemical model is illustrated in figure 3.1.2.

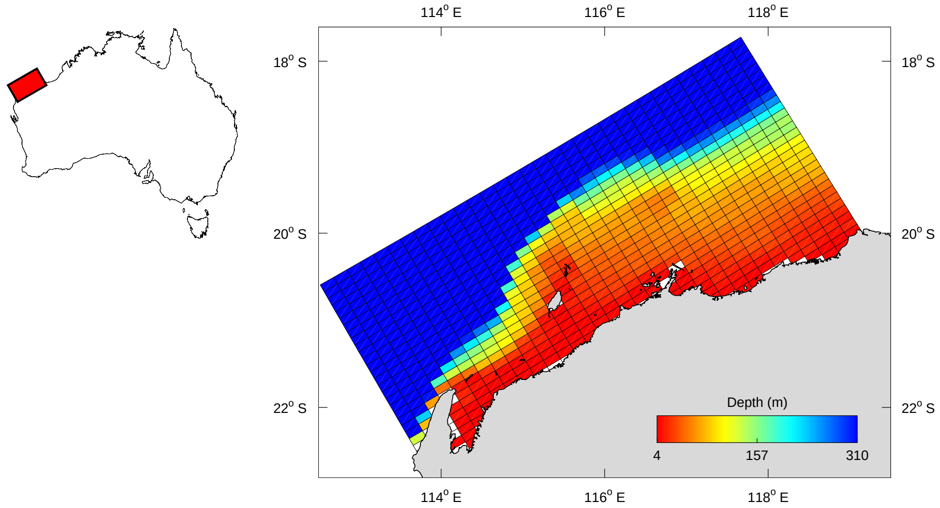

Figure 3.1.1: Biogeochemical grid domain.

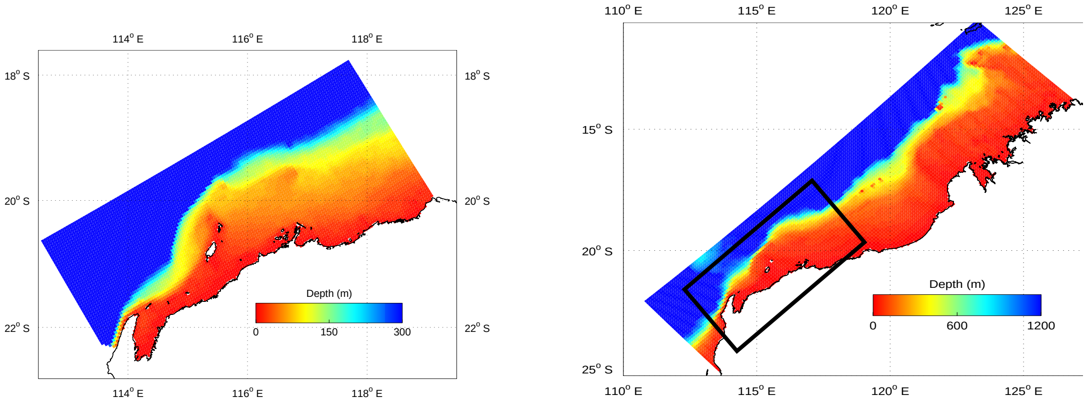

Regional 10 by 10 km grid

Nested 20 by 10 km grid

Figure 3.1.2: Biogeochemical grid configuration.

Values of some variables on the open boundaries of the biogeochemical grid were extracted from the CARS Climatology (Climatological Atlas of Regional Seas, Ridgway et al. 2002). These data are 1/8 degree gridded field output at 10 day intervals. The only variables included in this climatology relevant to forcing the biogeochemical model were nitrate, dissolved reactive phosphorus (phosphate) and dissolved oxygen. These variables were initialised and prescribed on the three open boundaries from the CARS climatology. Examples of the spatial and temporal distribution of NO_3 and PO_4 variables is displayed in figures 3.1.3 and 3.1.4.

The nutrient distributions prescribed from CARS represent a mean annual cycle. This was repeatedly cycled as the boundary condition for multi-year simulations. This obviously acts to suppress any interannual variability in multi-year simulations, and creates the risk of mis-match between physical boundary conditions from ACOM3 and the nutrient climatologies. It should also be noted that the climatology does not capture and mesoscale variability in the nutrient distributions.

It is readily observed from figure 3.1.2 that negligible nitrate is found in the mixed layer, below which concentration rapidly increases to significant values in deep water. The aquatic environment in the NWS region is oligotrophic with nitrogen being the limiting nutrient; in this context the NO_3 dynamics are of interest in preference to PO_4 and little discussion is subsequently given to phosphorus cycling in this report, although the biogeochemical model represents cycling of both phosphorus and nitrogen (Baird et al. 2003).

The absence of boundary data for the remaining state variables in the biogeochemical model required the prescription of plausible boundary conditions for these variables. We found that the standard no-gradient, or ‘zero flux’ condition commonly applied in these instances performed poorly due to positive feedbacks or instabilities which appeared to result from interactions between local transport and non-linear biology. Prescribing particular values for unknown variables on the boundary was also undesirable, as low concentration fronts could be seen to propagate into the model interior under inflow conditions.

A scheme was developed whereby a subregion at the boundary was defined over which the unknown state variables were sampled, and some form of statistic (e.g. mean, median, n^{th} percentile) was calculated and used as the boundary value. The subregion was defined on the basis of the magnitude of the normal velocity component decreasing to a defined threshold in the model interior. The statistic chosen was determined on a trial and error basis so as to produce smooth distributions without discontinuity across the open boundary, and in this case the 20 percentile value in the subregion was selected. This scheme proved quite successful in ensuring that the open boundaries became neither a source nor sink for state variables whose boundary values were not known.

This boundary scheme essentially forces values on the boundary to be similar to those observed in the interior of the model, in a given neighbourhood of the boundary. Given that the predominant inflow into the model domain occurs along shelf through the NE boundary, this boundary condition is equivalent to assuming that the shelf region upstream of the model boundary is behaving similarly to that inside the model domain.

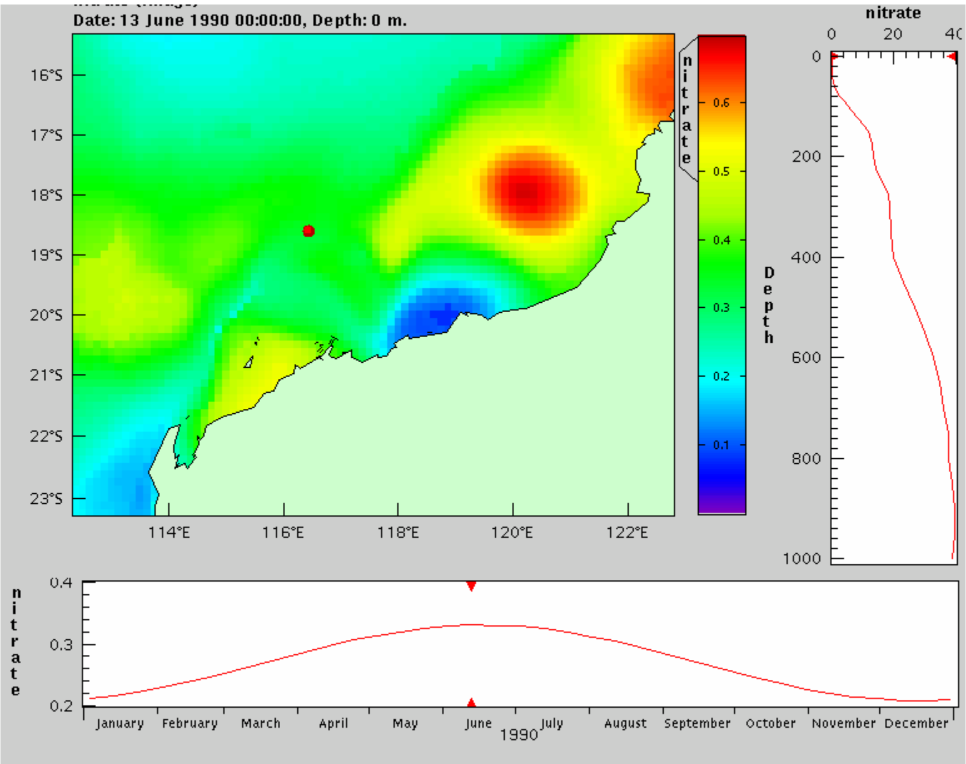

Figure 3.1.3: NO_3 distribution from CARS (micromolar). Depth profile and (surface) annual time series are taken at the location of the red dot.

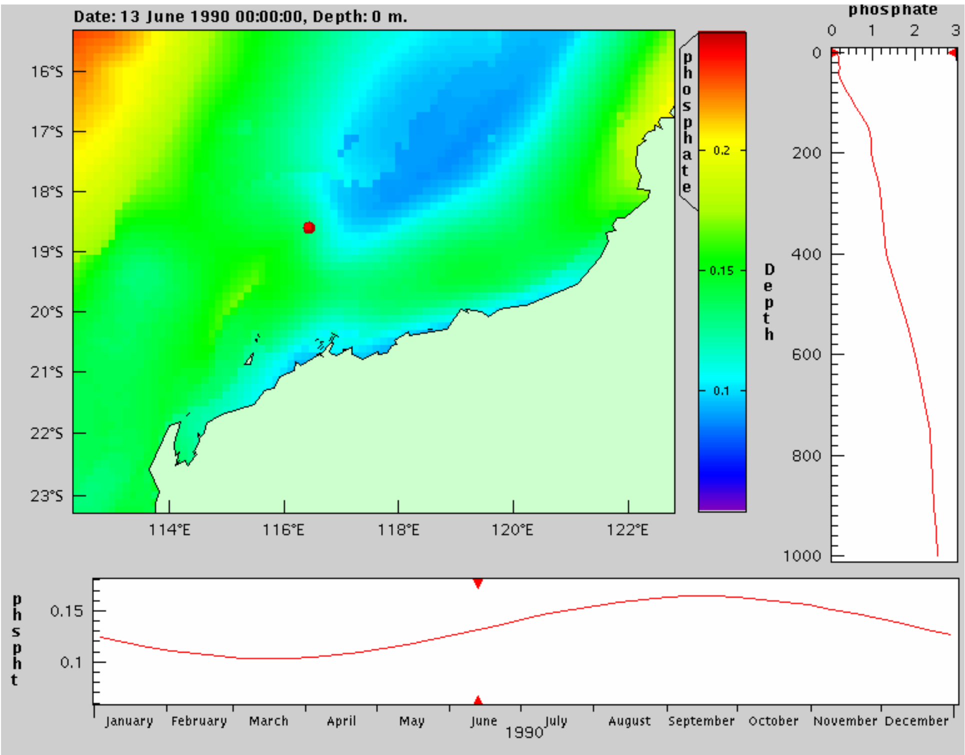

Figure 3.1.4: PO_4 distribution from CARS (micromolar).

3.2 Calibration

The lack of measured data in the North West Shelf region prevented the undertaking of a rigorous calibration procedure. Calibration was limited to comparing model output qualitatively, and where possible quantitatively, with the observations of Tranter and Leech (1987) and satellite imagery. Specifically, the objective was to produce a subsurface Chl*a* maximum (SCM) which lay below the mixed layer at approximately 70 m depth with concentrations of 0.5 to 2 μg/L and a corresponding surface signature of 0.1 to 0.5 μg/L. This maximum was required to remain roughly invariant over the seasonal cycle, but becoming more diffuse in the winter months. These features are evident in figure 3.2.1, reproduced from figure 11 of Tranter and Leech (1987), showing the seasonal and spatial distribution of *in vivo* chlorophyll fluorescence (IVF) measured in 'Turner Units', T.U. where μg Chl*a* L^{-1} ~ (4.8xT.U.) $x10^{-3}$ in summer and μg Chl*a* L^{-1} ~ (4.0xT.U.) $x10^{-3}$ in winter. Figures 3.2.3 and 3.2.4 show chlorophyll concentrations derived from *SeaWiFS* satellite imagery over the NWS. Surface concentrations over the shelf range form 0.2 to 1 μg/L and the difference between winter and summer distributions is not significant. Inshore the concentrations should be treated with caution due to contamination by suspended sediment. (Since the bulk of the phytoplankton biomass is expected to be found at depth satellite images are of limited use in analyses of phytoplankton dynamics on the NWS.)

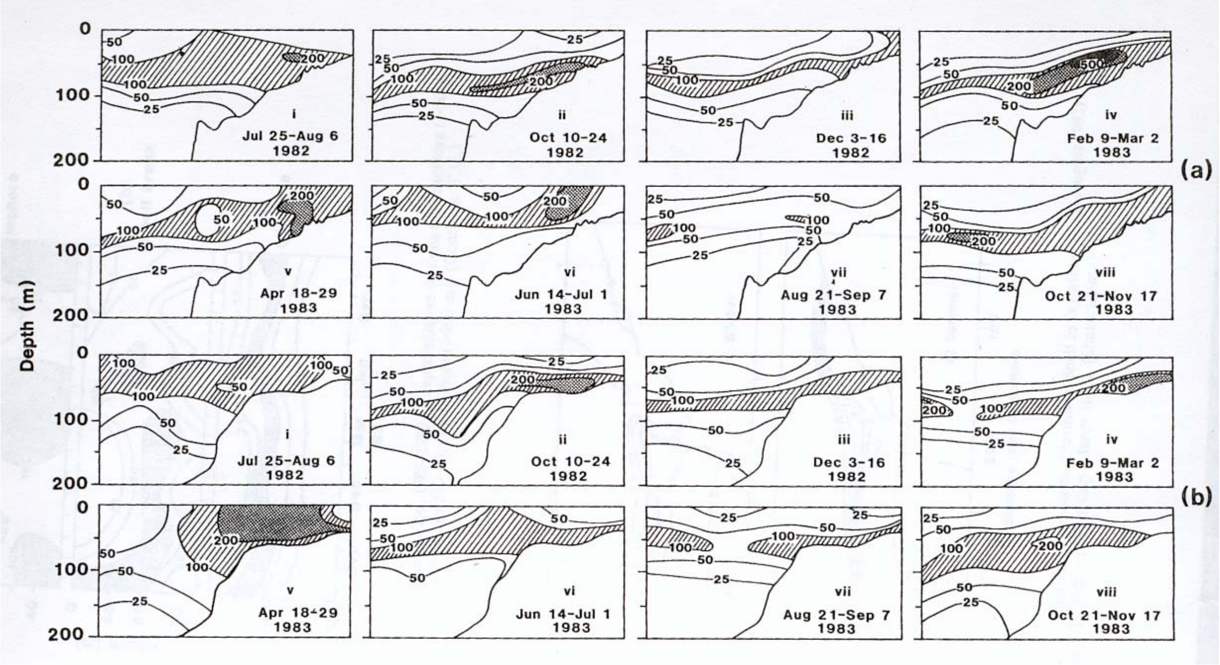

Figure 3.2.1: Seasonal and spatial distribution of IVF (T.U.), 1982 to 1983 taken along sections (a) ~200 km southwest of Port Hedland and (b) ~75 km northeast of Port Hedland. Taken from Tranter and Leech (1987), figure 11.

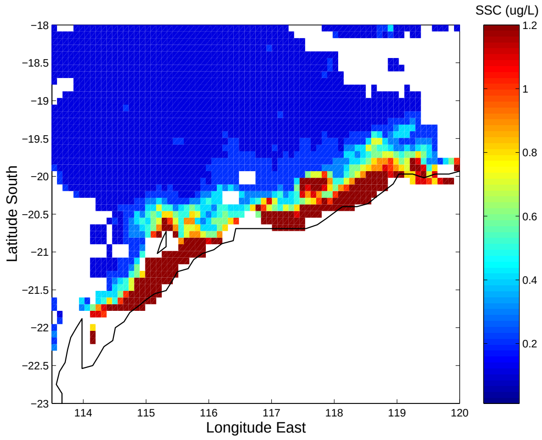

Figure 3.2.3: Summer Chl*a* (23/12/1997).

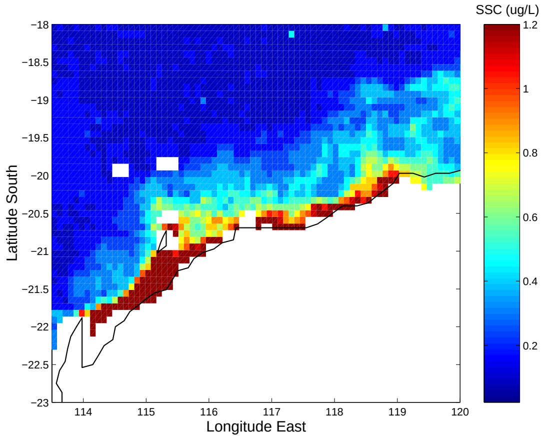

Figure 3.2.4: Winter Chl*a* (06/06/1998).

Nitrate was required to remain low in the surface mixed layer throughout the domain. The distribution of nitrate-N across the NWS is reproduced from figure 13 of Tranter and Leech (1987) as figure 3.2.5.

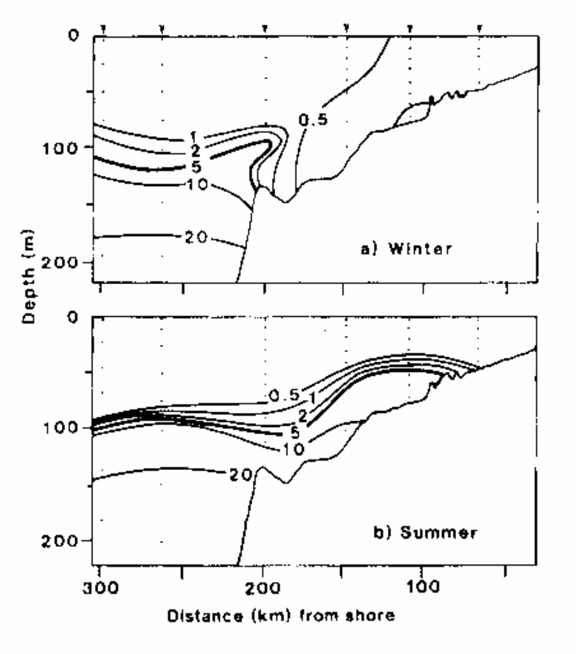

Figure 3.2.5: Nitrate-N (µg-at L^{-1}) distribution across the NWS for (a) winter (July to August 1982) and (b) summer (February to March 1983). Taken from Tranter and Leech (1987), figure 13.

Model output was compared with observations taken in the model domain during 1996 and 1999 and results are displayed in scattergram format in figures 3.2.6 and 3.2.7 for nitrate and dissolved inorganic phosphorus respectively. Large deviations in modelled values are apparent, especially during 1999 where the error can be 50% or more of the variable value. This is hardly surprising since the model is initialised and forced with the climatology, and effectively model results match observations to the degree that the climatology represents the actual nutrient distribution for a particular year. In this context model-observation comparisons are not particularly useful save for highlighting the fact that unless accurate forcing is applied accurate predictive capability is low. However, it is expected that the mean state of the NWS is well captured by forcing with climatology, and thus the model provides a basis for understanding general patterns and processes in NWS phytoplankton dynamics.

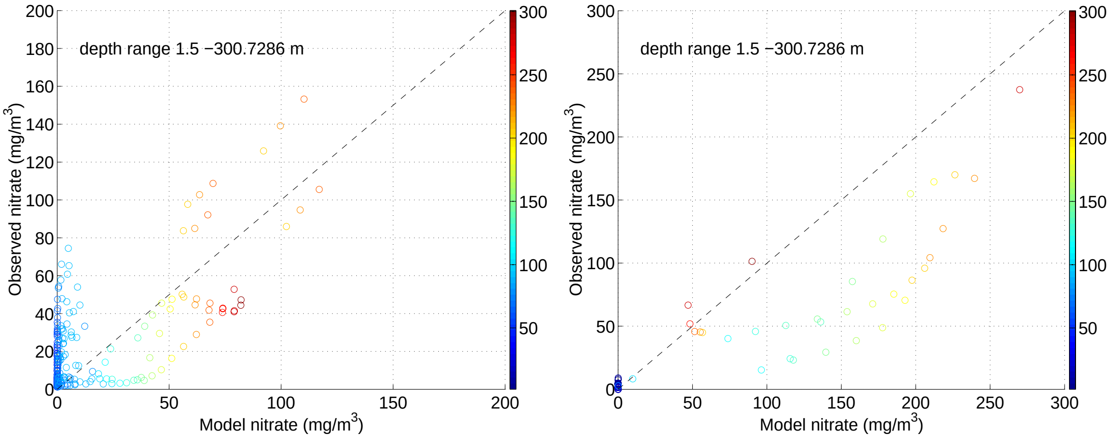

(a) 1996

(b) 1999

Figure 3.2.6: Nitrate model-observation comparisons.

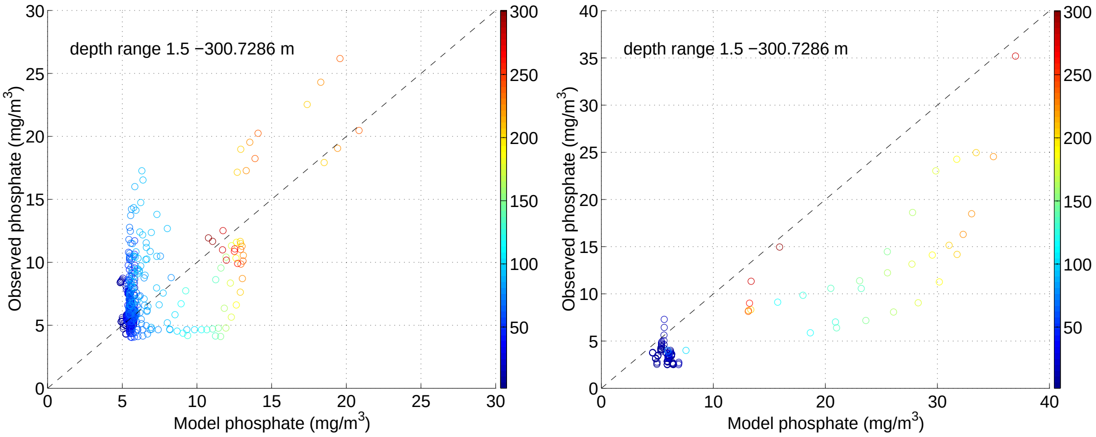

(a) 1996

(b) 1999

Figure 3.2.7: DIP model-observation comparisons.

A series of model experiments were conducted to identify which model parameters and processes extert most influence over the predicted spatial and temporal patterns of nutrients and phytoplankton biomass. Over the outer shelf and offshore, it was found that, for a given physical regime (section 4), the depth and magnitude of the SCM in the model is controlled by a relatively small number of key biological parameters and processes. It is worth noting that this model was originally developed for a relatively shallow (20 m) well-mixed coastal embayment (Murray & Parslow, 1999), although it has subsequently been applied to stratified coastal estuaries. It was not obvious a priori that the model structure and process formulation would adequately describe plankton dynamics and nutrient cycling in a continental shelf/slope ecosystem. In fact, the model formulation has proved quite robust under this offshore extension.

The representation of small and large (flagellate, microzooplankton and diatom, mesozooplankton) functional groups in the model was originally designed to allow coastal models to behave realistically under both nutrient limited and nutrient enriched conditions. The small flagellate functional group is subject to microzooplankton grazing control, forming a tightly coupled microbial loop which efficiently recycles nitrogen under N-limited conditions. The diatoms escape grazing control and form blooms under conditions of excess nutrient and light.

In the physical environment of the outer NWS, the model predicts a partial vertical separation of these functional groups, with the N-limited oligotrophic mixed layer dominated by small flagellates and microzooplankton, with low biomass but high turnover rates, and the SCM dominated by large phytoplankton (diatoms). In the model, the SCM exists as a local dynamical balance between upward fluxes of nutrient from below due to vertical mixing or advection, and downward fluxes of organic nitrogen as phytoplankton and detritus due to sinking. Phytoplankton in the SCM are subject to both light and nutrient limitation. Increases in vertical mixing or advection and nutrient supply tend to result in a shallower SCM, subject to higher light intensities, with increased phytoplankton biomass and increased growth rates. For fixed physical conditions, the depth and magnitude of the SCM in the model are most sensitive to the parameters controlling light and nutrient-dependence of large phytoplankton growth rates, large phytoplankton sinking rates, and to a lesser extent large zooplankton grazing rates. Conversely, chlorophyll levels in the mixed layer tend to be most sensitive to the microzooplankton grazing parameters.

In the model version used here, the representation of light and nutrient limitation has been modified to reduce the number of "tunable" parameters (Baird et al. 2003). The key parameter is cell radius, which scales capability for nutrient uptake and light absorption under limiting conditions. Zooplankton grazing or clearance rates are also scaled by cell/organism size, and by swimming speed. Large phytoplankton sinking rates, and maximum growth rates of both phytoplankton and zooplankton, are set independently. The values of these key model parameters after calibration are listed in tables 3.2.1 and 3.2.2. In general, these required little change from values obtained in calibration of coastal models. The large phytoplankton sinking rate is higher than values previously used in shallow coastal applications of the model, and the large phytoplankton maximum growth rate is lower and equal to that for small phytoplankton. A complete list of model parameters is provided in Appendix A.

Table 3.2.1: Phytoplankton.

Parameter	Large Phytoplankton	Small Phytoplankton
Maximum Growth Rate (d^{-1})	1.25	1.25
Radius (m)	10×10^{-6}	2.5×10^{-6}
Settling Velocity ($m\ d^{-1}$)	1.73	0

Table 3.2.2: Zooplankton.

Parameter	Large Zooplankton	Small Zooplankton
Maximum Growth Rate (d^{-1})	0.1	3
Radius (m)	500×10^{-6}	12.5×10^{-6}
Swimming velocity ($m\ s^{-1}$)	1×10^{-3}	2×10^{-4}

Sinking rate for labile detrital nitrogen = 5 m d^{-1}

4. RESULTS

4.1 General results

The predicted distributions of the major state and diagnostic variables are presented below. The surface Chl*a* distribution generally forms a band of higher concentration inshore of the 200 m isobath (e.g. figure 4.1.1; 24 April 1999) near the north-eastern boundary. This is not a boundary artifact, since the larger scale regional model also predicts increased chlorophyll at the same location (figure 4.1.2). Surface Chl*a* values are generally less than 0.5 mg Chl*a* m^{-3}, consistent with the satellite imagery (figures 1.5 and 1.6). The south-western portion of the domain is consistently associated with lower surface Chl*a* values. There exists a subsurface Chl*a* maximum at approximately 70 m, below the mixed layer, with concentrations of 1 to 1.5 mg Chl*a* m^{-3}. This band intersects the shelf at the location where the surface Chl*a* is maximum. This corresponds to the location where vertical turbulent diffusion is capable of mixing the SCM to the surface; typically the offshore extent of surface and bottom boundary layer overlap. The SCM is a feature present over the whole North West Shelf domain offshore of approximately the 70 m contour.

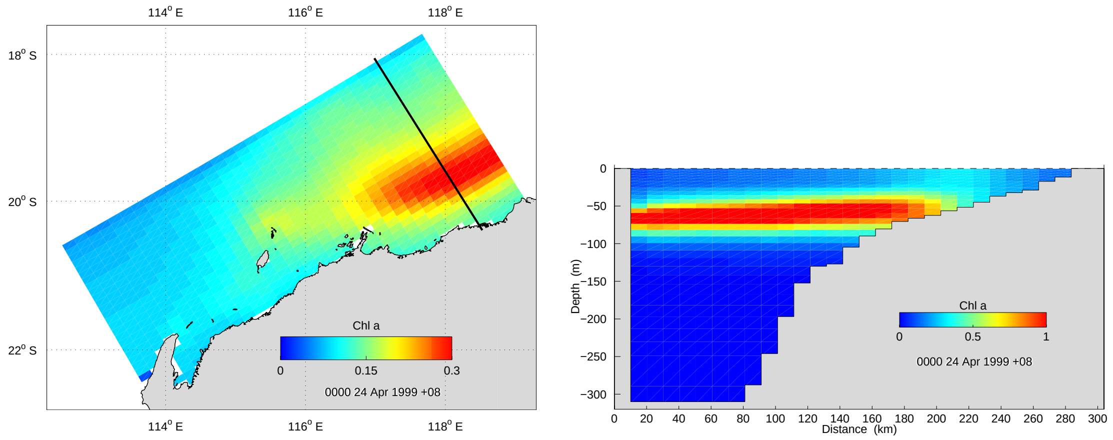

Surface Section

Figure 4.1.1: Chl*a* distribution (mg Chl*a* m^{-3}).

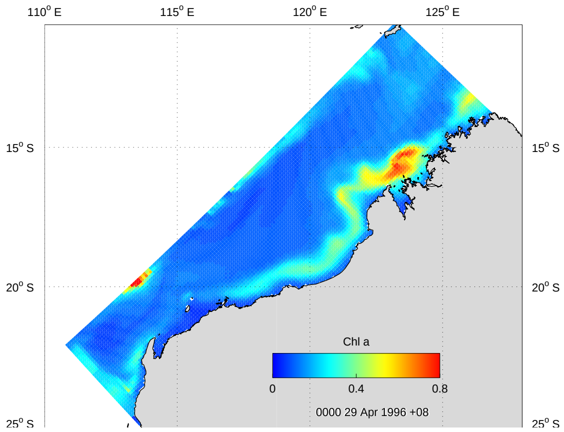

Figure 4.1.2: Chl*a* distribution on regional domain (mg Chl*a* m^{-3})

The SCM is comprised largely of the large phytoplankton size class (figure 4.1.3), the distribution of which closely mimics the Chl*a* distribution. The smaller size class or nanophytoplankton have a maximum concentration in the upper part of the SCM (figure 4.1.4), but are much more strongly distributed above the SCM and into the mixed layer. Large and small phytoplankton contribute about equally to the surface chlorophyll maximum near the NE boundary, where the SCM is mixed to the surface. However, over most of the domain, small flagellates dominate the surface (mixed layer) biomass.

The growth rate of nanophytoplankton is approximately 1 to 1.5 day^{-1} above and within the SCM, compared to <0.3 day^{-1} above and ~0.7 day^{-1} in the SCM for the large phytoplankton class (figures 5.1.5 and 5.1.6). The prediction of low biomass and high phytoplankton growth rates in the mixed layer is quite consistent with general observations and understanding of oligotrophic ocean behaviour. The predicted growth rates in the SCM are quite high, consistent with the relatively shallow depth, and suggest enhanced vertical mixing and nutrient supply compared with open ocean gyres (Mackey et al. 1997).

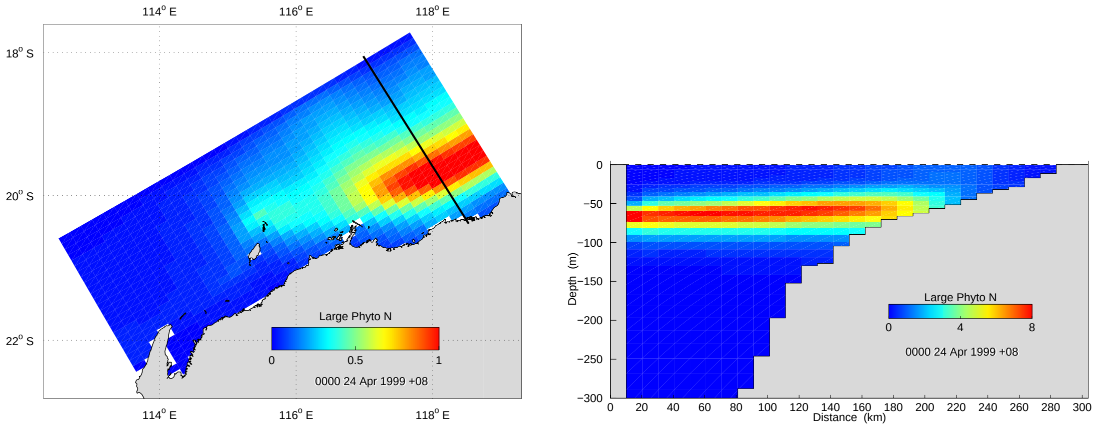

Surface

Section

Figure 4.1.3: Large Phytoplankton Nitrogen distribution (mg N m^{-3}).

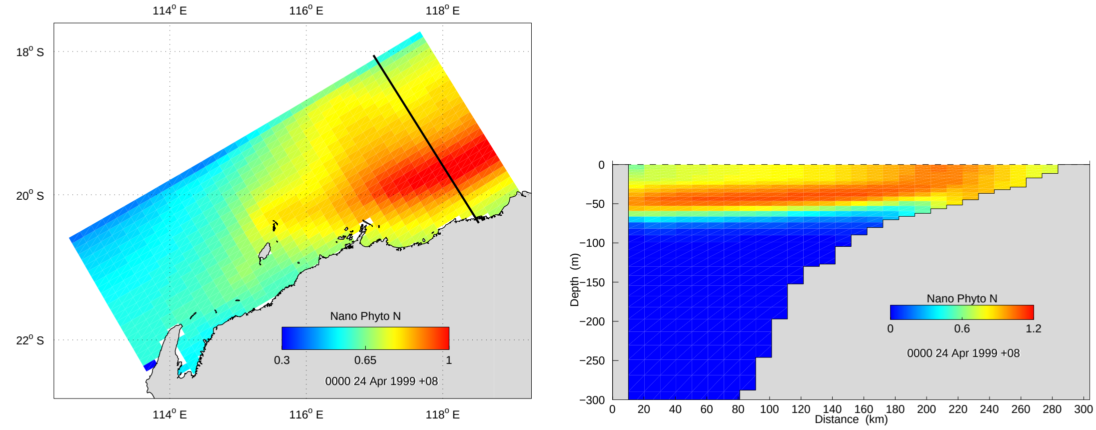

Surface Section

Figure 4.1.4: Nano phytoplankton Nitrogen distribution (mg N m^{-3}).

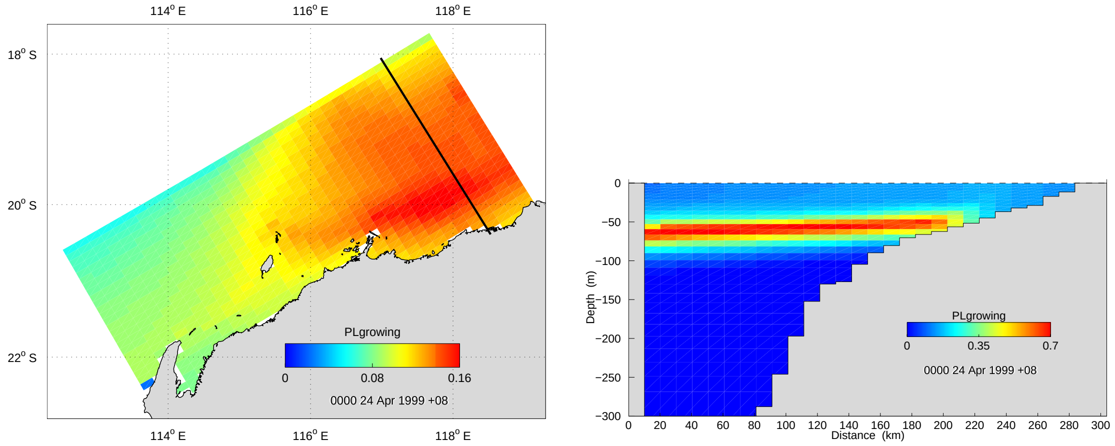

Surface Section

Figure 4.1.5: Large phytoplankton growth rate (day^{-1}).

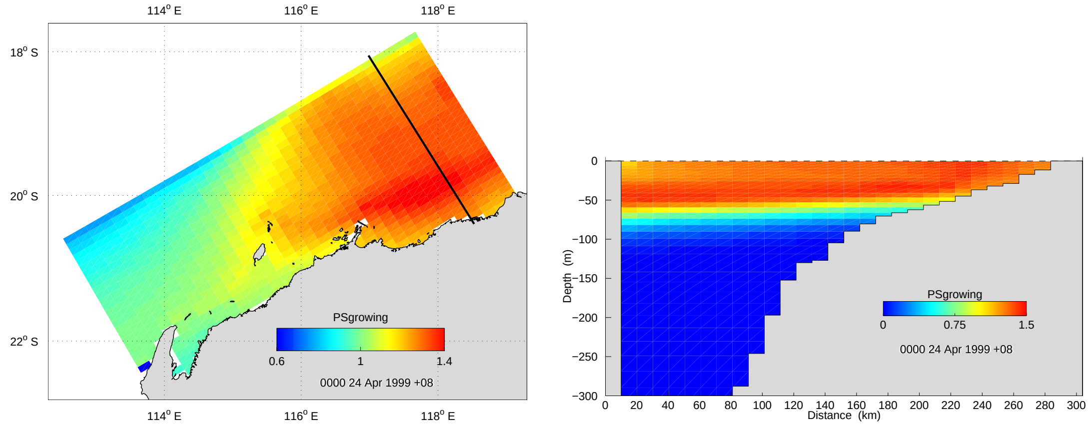

Surface Section

Figure 4.1.6: Nano phytoplankton growth rate (day^{-1}).

Dissolved inorganic nitrogen (DIN) values in the surface layer are low, with the largest values corresponding to the location of the surface Chl*a* maximum (figure 4.1.7), where strong column mixing allows DIN from below the SCM, or from sediment recycling, to reach the surface. DIN increases rapidly below the SCM to values of over 250 mg N m^{-3} below 200 m. This nitrogen is comprised predominantly of nitrate (NO_3) (figure 4.1.8), although ammonia (NH_3) is higher in the surface with a peak in the SCM (figure 4.1.9). The nitrate distribution over the shelf is comparable to the climatology, indicating the model reproduces the nutrient cycling satisfactorily. Locations of maximum surface nitrogen correlate well with location of maximum productivity; i.e. near the north-eastern boundary of the domain. The nitrate distribution exhibits a slight tendency to upwell onto the shelf, although as will be demonstrated later this is temporally variable.

The labile planktonic detrital nitrogen component (figure 4.1.10) consists of particulate nitrogen resulting from phytoplankton mortality and zooplankton excretion. The spatial distribution of labile detrital nitrogen again resembles that of Chl*a*. This component is broken down at a rate of 0.1 day^{-1} and recycled into ammonia and then possibly to nitrate via nitrification (Water column nitrification is represented simply in the model by a temperature and substrate-dependent conversion rate from ammonia to nitrate. The rate constant was adjusted to obtain realistic distributions for nitrate below the SCM.). More importantly, this fraction may sink through the SCM (settling velocity ~5 m day^{-1}) into deeper water and hence acts as an important vehicle for export of nitrogen from the upper layer. Nitrogen is also lost from the system as N_2 by denitrification of nitrate in sediments. In the steady state the amount of nitrogen supplied to sustain the SCM must be balanced by the export of nitrogen. There exists a refractory detrital nitrogen component that breaks down on longer timescales (0.0036 day^{-1}) and thus does not play a large role in controlling the vertical distribution of nitrogen within this system.

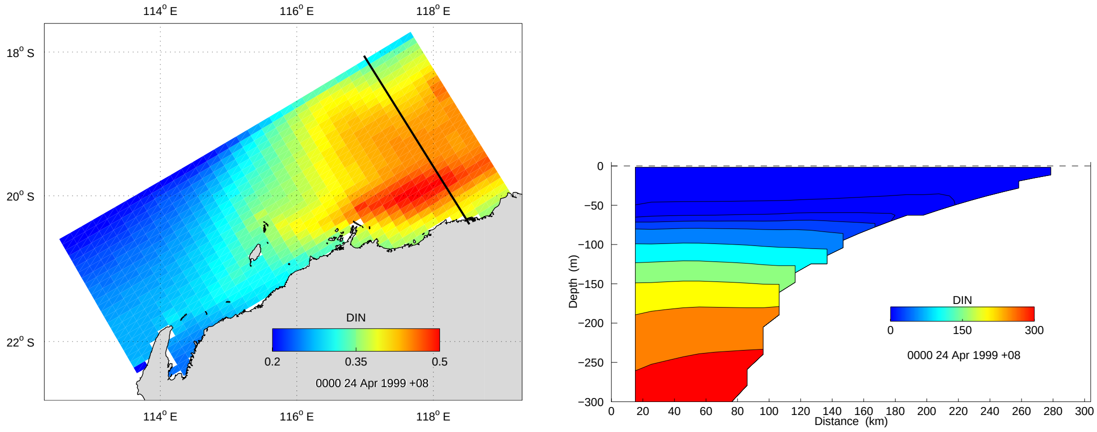

Surface Section

Figure 4.1.7: Dissolved inorganic Nitrogen distribution (mg N m^{-3}). Contours in the section are 0.1, 1, 10, 25, 50, 100, 150, 200, 250.

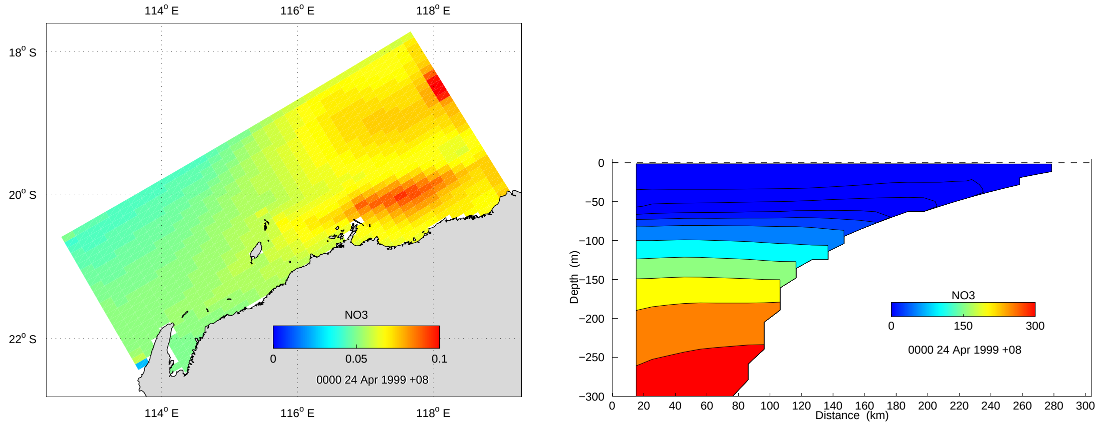

Surface Section

Figure 4.1.8: NO_3 distribution (mg N m^{-3}) Contours in the section are 0.01, 0.1, 1, 10, 25, 50, 100, 150, 200, 250.

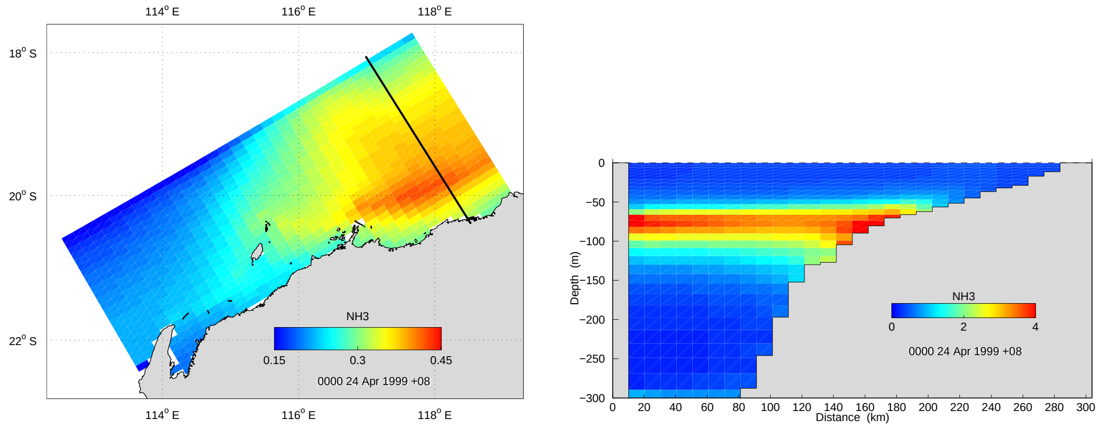

Surface Section

Figure 4.1.9: Ammonia distribution (mg N m^{-3}).

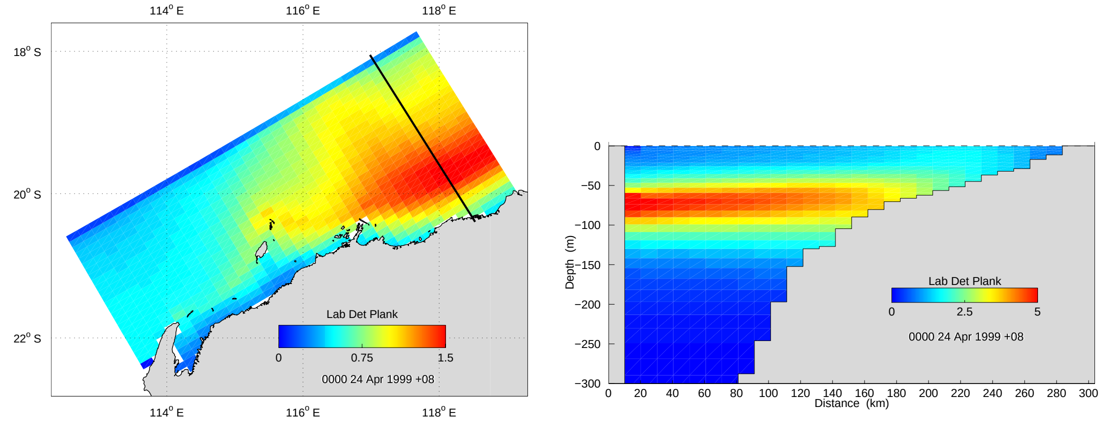

Surface Section

Figure 4.1.10: Planktonic labile detrital Nitrogen distribution (mg N m^{-3}).

Large and small zooplankton graze on large and small phytoplankton respectively. Their distributions resembles that of their food source, although large zooplankton are more dispersed in both the vertical and horizontal, reflecting their longer turnover time. The large zooplankton have maximum concentration in the SCM with a surface distribution spread over the north-eastern portion of the domain (figure 4.1.11). Micro-zooplankton possess a similar surface distribution, but are more evenly distributed throughout the mixed layer (figure 4.1.12). The growth rate of micro-zooplankton is an order of magnitude greater than large zooplankton at the surface, but the maximum growth rates are comparable (figures 4.1.13 and 4.1.14); the large zooplankton maximum growth rate occurring in the SCM.

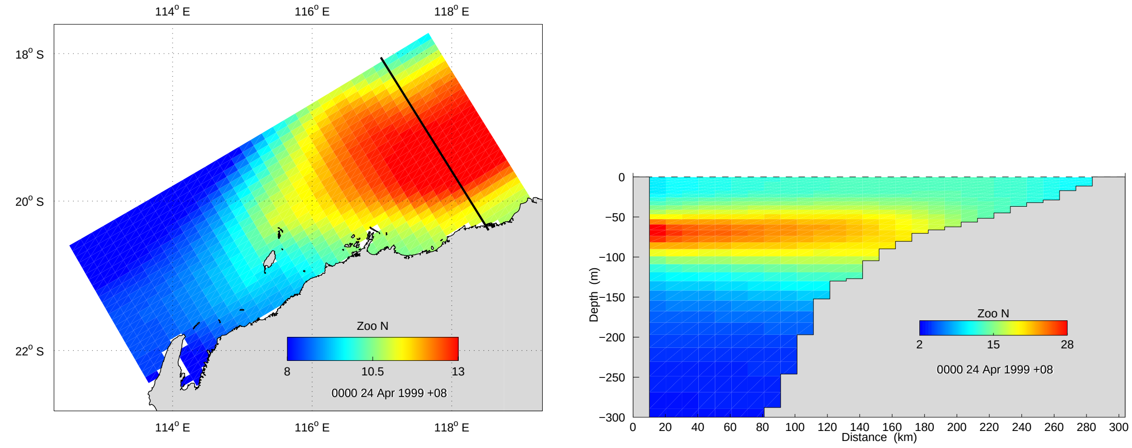

Surface　　Section

Figure 4.1.11: Large zooplankton distribution (mg N m^{-3}).

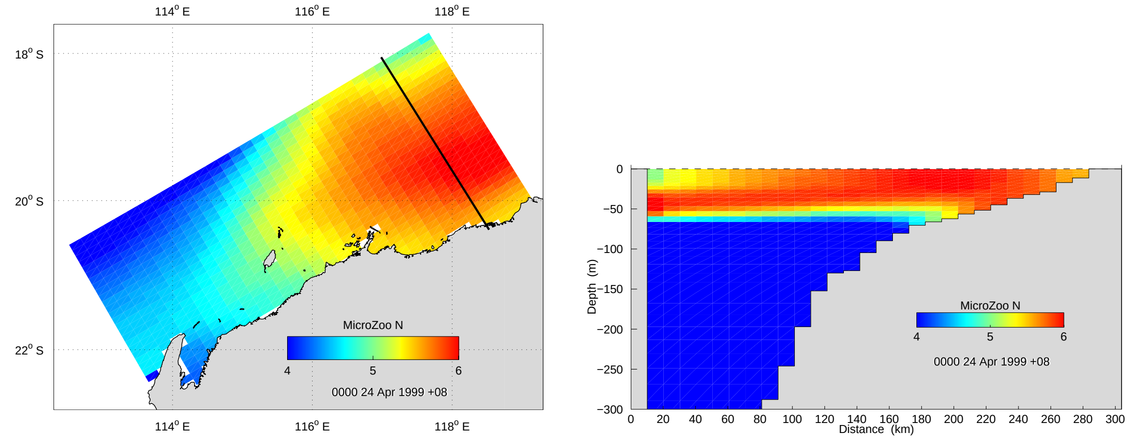

Surface　　Section

Figure 4.1.12: Micro zooplankton distribution (mg N m^{-3}).

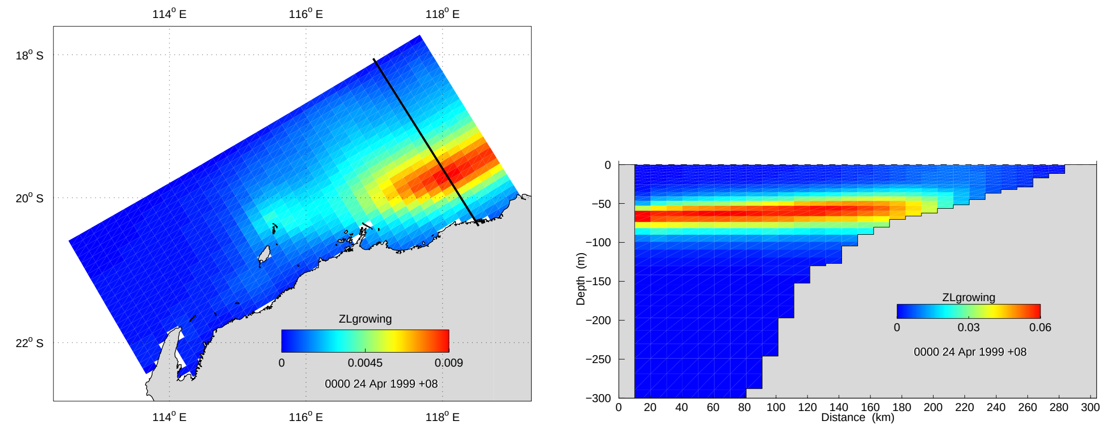

Surface Section

Figure 4.1.13: Growth rate of large zooplankton (day^{-1}).

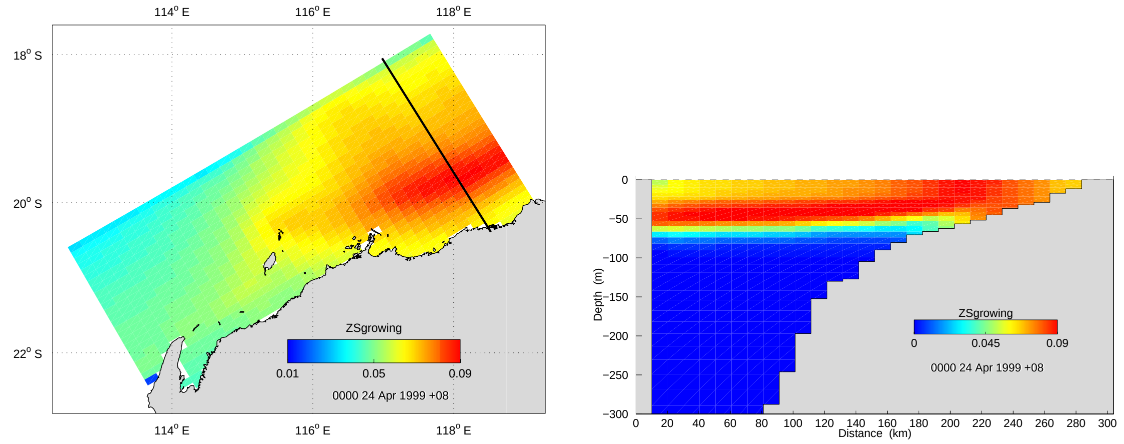

Surface Section

Figure 4.1.14: Growth rate of small zooplankton (day^{-1}).

The benthic and epibenthic biota generally reach equilibrium on longer time scales than the plankton. Biomass distributions are presented for macroalgae and seagrass at the end of the four year simulation (figures 4.1.15 and 4.1.16), when distributions have adjusted to light and nutrient availability. Macroalgae has maximum concentration in a band along the 90 m isobath. Macroalgae in the model use dissolved inorganic nitrogen in the water column. They are strongly nitrogen-limited inshore of 90 m, and light limited offshore. Seagrass is maximum at approximately 60 m, with lower biomass inshore of this depth. Seagrass utilise DIN in pore water, so their distribution is primarily controlled by light availability, with low biomass in deeper water where light levels are low. Inshore lower seagrass biomass is found due to attenuation of light from suspended sediments. These predicted distributions should be taken as indicative only. The model assumes substrate is suitable for macroalgae and seagrass everywhere. In practice, seagrass will only be found on reasonably stable soft sediments, whereas macroalgae in general require hard substrate. The patterns in figures 4.1.15 and 4.1.16 indicate where light and nutrient availability favour macrophytes.

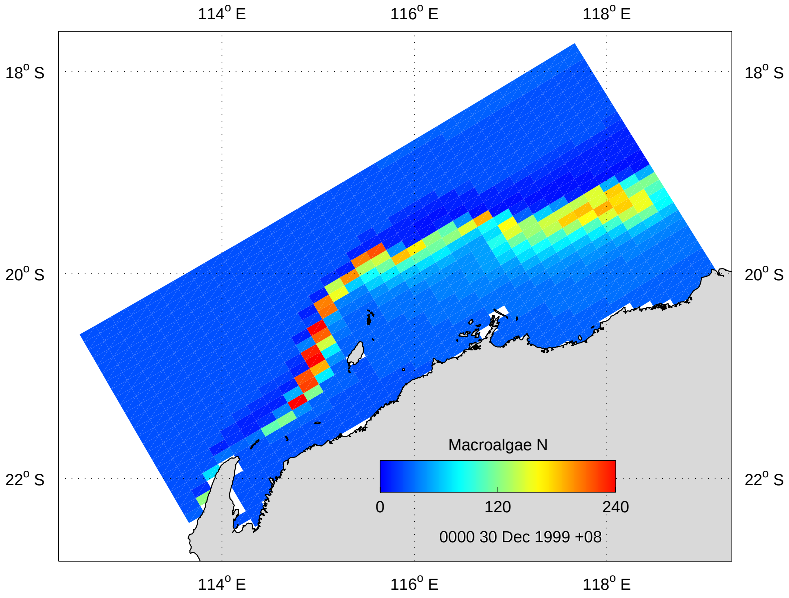

Figure 4.1.15: Macroalgae distribution (mg N m^{-2}).

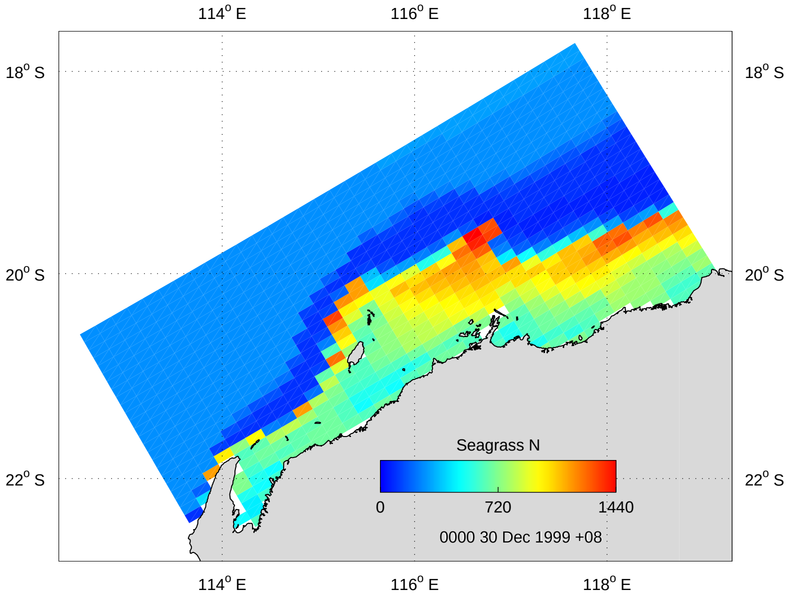

Figure 4.1.16: Seagrass distribution (mg N m^{-2}).

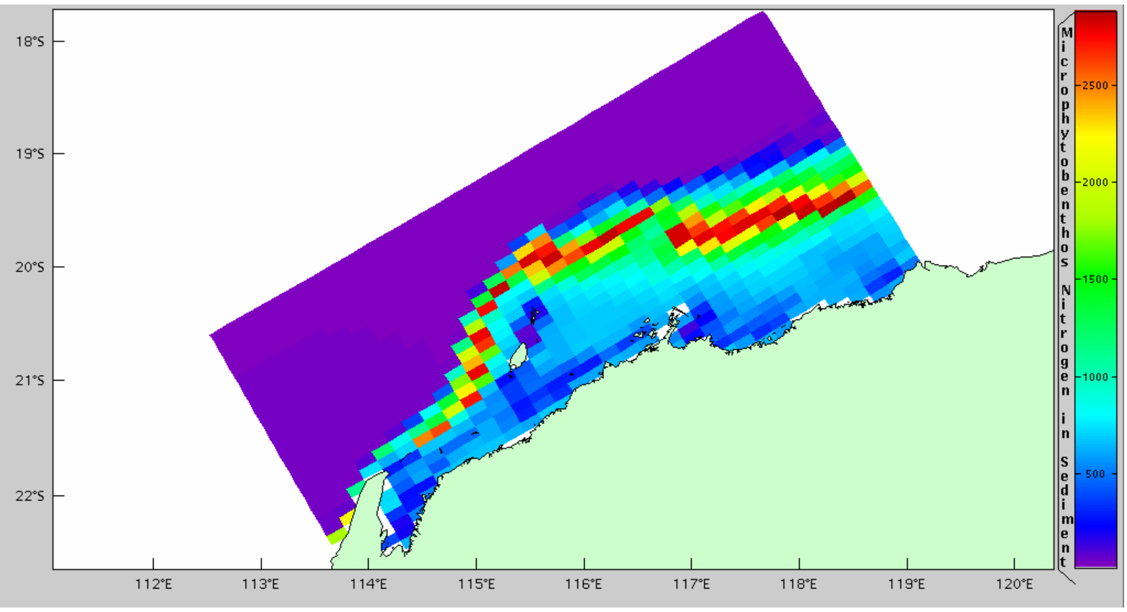

Figure 4.1.17: Microphytobenthos distribution (mg N m^{-2}).

4.2 Factors controlling the SCM

A distinctive feature of the solutions presented above is the presence of the subsurface chlorophyll maximum (SCM). The SCM is maintained through a balance between light and nitrogen limitation. Dissolved inorganic nitrogen concentrations in surface waters are generally very low and limiting to phytoplankton growth, whereas solar irradiance there is saturating. At depths where nitrate concentrations are high and saturating, light levels are inadequate to support growth. The maximum Chl*a* concentration is found at a depth where phytoplankton can maximise growth by minimising light and nitrate limitation. The photic zone extends to ~100 m and nitrate is depleted in the mixed layer to approximately 50 m, hence the SCM results at depths between 50 and 100 m. A decrease in light or increase in nitrate supply will make the SCM shallower. The SCM removes dissolved nitrogen from the water column and converts it into organic nitrogen as phytoplankton biomass. A flux of nitrate into the SCM is therefore required to maintain the vertical nitrate profile. In the steady state (i.e. constant phytoplankton concentration), and ignoring horizontal advection, the vertical flux of DIN upward through a surface just below the SCM is required to be balanced by an equivalent export of particulate nitrogen, in the form of particulate detrital nitrogen via sinking. If the supply of nitrogen is increased via increased mixing rates or increased DIN gradients below the SCM, then the concentration of phytoplankton in the SCM will increase, and vice versa.

Large zooplankton exert grazing pressure on the large phytoplankton in the SCM. In the equilibrium situation the consumption must equal production. If consumption of phytoplankton by grazers were to increase, this implies that production must also increase. The only way production may be regulated is by adjustment of the light regime, i.e. the vertical position in the water column. Therefore if production is to increase, exposure to higher light levels must occur, resulting in the SCM shifting higher in the water column. Similarly, if grazing were to decrease the SCM shifts lower in the water column. Because of these interactions with grazing, increases in nutrient input and SCM biomass and production typically also result in shallowing of the SCM.

In the mixed layer the concentration of nano phytoplankton is low but productivity is high. These smaller phytoplankton have the ability to utilise nutrients at a faster rate and achieve higher growth rates. This biomass is just as quickly consumed by micro-zooplankton, which is subsequently recycled back to ammonia via mortality and excretion. The ammonia is then available again for uptake by the nano phytoplankton. Nitrogen is cycled with high but not 100% efficiency in the mixed layer, and losses due to net export of detrital matter must ultimately be balanced by weak inputs of DIN from below. This balance determines the concentration of total nitrogen in the mixed layer. The partitioning of this nitrogen between phytoplankton, zooplankton and detritus is determined by zooplankton grazing and mortality and detrital sinking rates.

This vertical steady-state analysis almost certainly represents an over simplification of processes in the numerical model and in the real world. It’s possible that mixing of DIN through the SCM and into the mixed layer is dominated by intermittent events such as wind mixing or spring neap tidal variation. The cyclone scenario discussed below represents an extreme example of such an event. It’s also likely that vertical exchanges do not occur uniformly over the domain, so that vertical fluxes are concentrated in some areas. In particular, the zone where bottom and surface boundary layers join is a site where nutrients are readily mixed into surface waters. If sufficient nutrient is injected into the mixed layer, it is likely in the model (and in the real world) to result in a transient diatom bloom, which will lead in turn to enhanced export of nitrogen out of the mixed layer. However, given that part of the nitrogenis captured and recycled in the microbial loop, it may lead to increased biomass which persists and is advected away from the site of injection. This effect can be seen in comparing the broader surface distribution of nanophytoplankton (figure 4.1.4), with large phytoplankton (figure 4.1.3).

These concepts are captured in the schematic of primary production illustrated in figure 4.2.1.

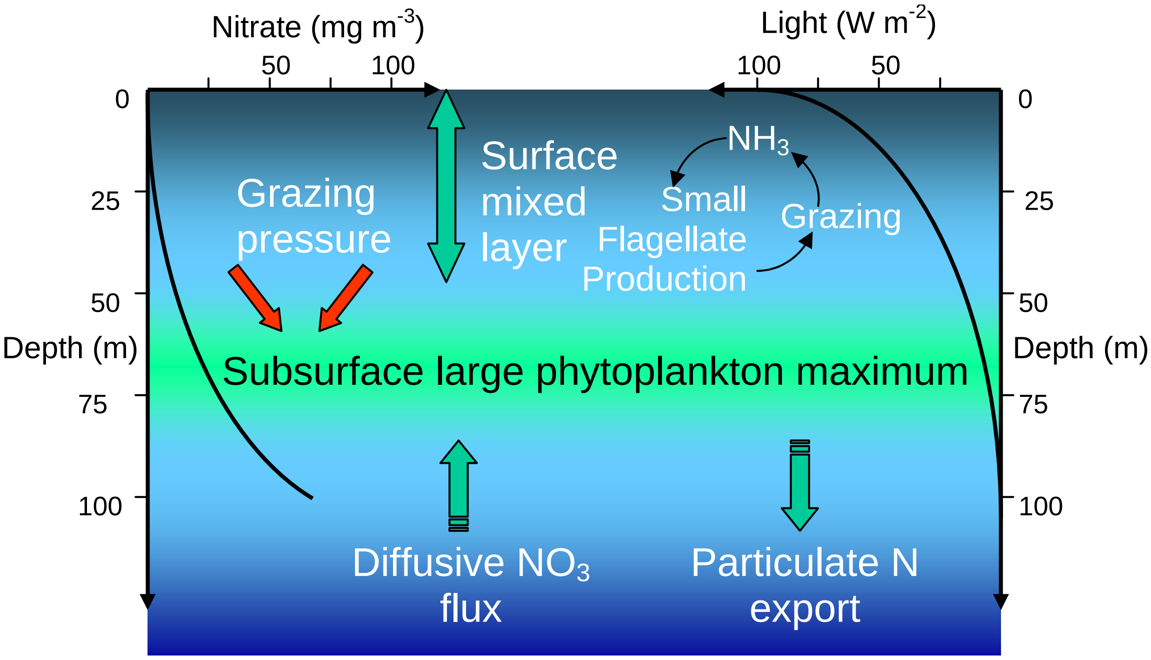

Figure 4.2.1: Primary productivity schematic.

4.3 Source of Nitrate

The source of nitrogen responsible for maintaining the productivity on the North West Shelf has been investigated by Holloway et al. (1985). The findings of Holloway et al. (1985) point to a variety of mechanisms that may potentially act as a nitrogen source. These authors estimated that the upper bound for supply of nitrogen required to maintain productivity is 0.11 g N m^{-2} day^{-1}. This figure is estimated to be 30 to 40% of the total nitrogen required, with the remaining 60 to 70% being made available through regeneration by zooplakton. It was also acknowledged that nitrogen regeneration from the benthos may contribute to primary production. There exists little terrestrial input of nitrogen (Holloway et al. 1985 estimated <0.03% is terrestrial), hence the nitrogen supply is confined to oceanic sources. Holloway et al. (1985) estimate that ~80% of the nitrogen required to sustain productivity can be made available from advection onto the shelf by the semidiurnal tide and longer period (greater than 35 h) upwelling events. These upwelling events are found to occur in summer when the Leeuwin Current is weak and wind forcing is capable of reversing the flow. The passage of tropical cyclones were found to contribute small amounts of nitrogen via vertical advection and mixing. Horizontal mixing from the barotropic and internal tide could potentially transport nitrate onto the shelf from deeper waters. The internal tide is believed to degenerate into bores and solitons while propagating over the shelf which are capable of pumping deep water onto the shelf through the generation of vertical mixing resulting from energy dissipation.

These mechanisms are all valid and no doubt contribute to productivity. Given that there exists large amounts of nitrate at depths greater than 100 m, in the modelling context the nitrogen flux supporting primary productivity reduces to mechanisms whereby this nitrogen is made available to the SCM. Since the primary uptake of new nitrogen is by phytoplanton within the SCM, the movement of nitrate onto the shelf or into surface waters (mixed layer) is not vital for maintaining primary productivity; it is only required for a nitrate flux to exist into the SCM below the mixed layer. As noted earlier, the SCM actually acts as a barrier to prevent any nitrate from entering the mixed layer through vertical motion. However, increased rates of supply of nitrate through upwelling or increased mixing will lead to increased production through shallowing and intensification of the SCM. If this vertical flux increases sufficiently, the SCM will shallow to the point where it merges with the mixed layer and a surface bloom results. There is little evidence of surface blooms on the NWS, except in the zone where bottom and surface boundary layers meet.

Three mechanisms are proposed as nitrogen supply mechanisms to the SCM, vis. horizontal advection (long-shore and cross shelf), vertical advection and vertical diffusion. Three scenarios were performed in order to gauge the relative contributions of horizontal advection and vertical diffusion. The first scenario ran the model for 1999 using the initial condition from 1998 (i.e. three years spin up) and used a no-gradient (i.e. zero flux) open boundary condition throughout the water column on all open boundaries for nitrate only. This removed any advective source of nitrate through the open boundaries; the only supply of nitrogen being at depth from the initial condition. The second scenario was the same as the first except the open boundaries were forced with the CARS climatology below 80 m (approximately the bottom of the SCM). This effectively removed any direct horizontal flux of nitrogen into the SCM and mixed layer. The third scenario did not perform vertical diffusion on nitrate, removing the vertical diffusive flux of nitrate into the SCM.

Firstly, the chlorophyll distribution at the end of 1999 is displayed in figure 4.3.1 for reference. The chlorophyll results from the scenarios are displayed in figures 4.3.2 to 4.3.4. Cross section views are taken at approximately the middle of the domain and the plan views are taken at the depth which corresponds to the base of the SCM.

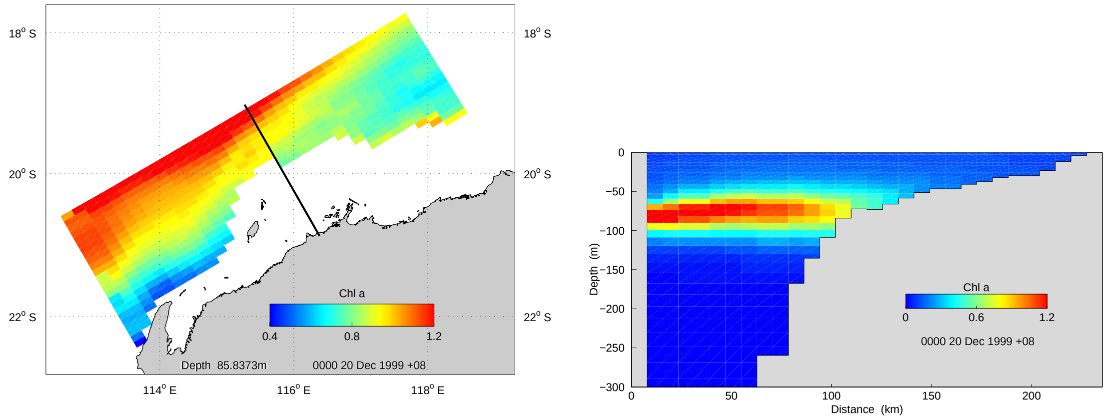

(a) Plan (b) Section

Figure 4.3.1: Chl*a* concentration at 20 December 1999.

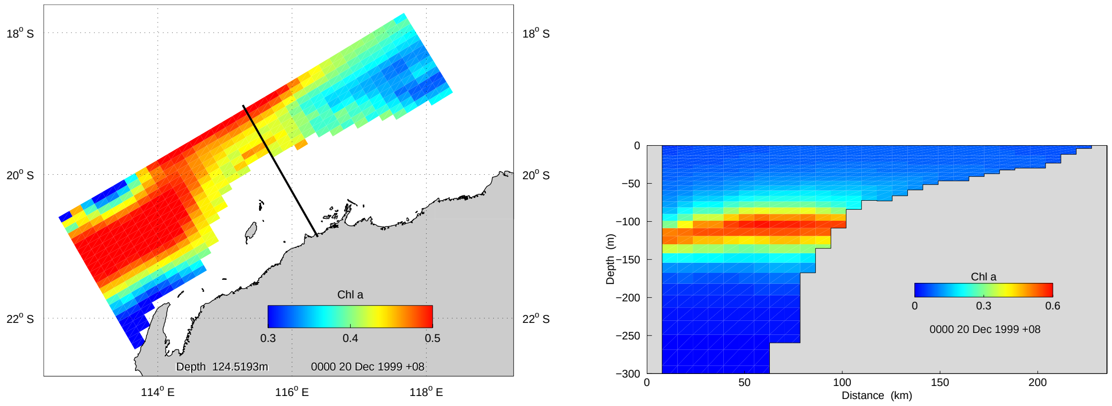

(a) Plan (b) Section

Figure 4.3.2: Chl*a* concentration at 20 December 1999: no advection.

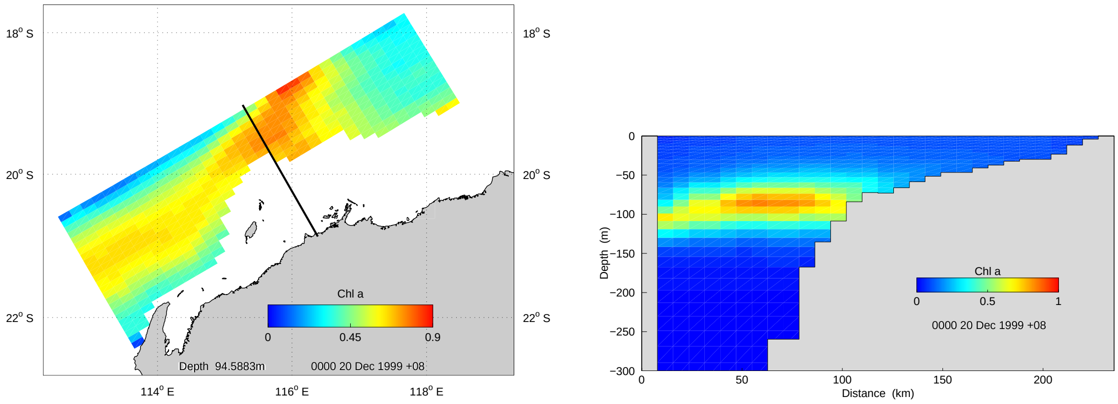

(a) Plan (b) Section

Figure 4.3.3: Chl*a* concentration at 20 December 1999: no advection above 80 m.

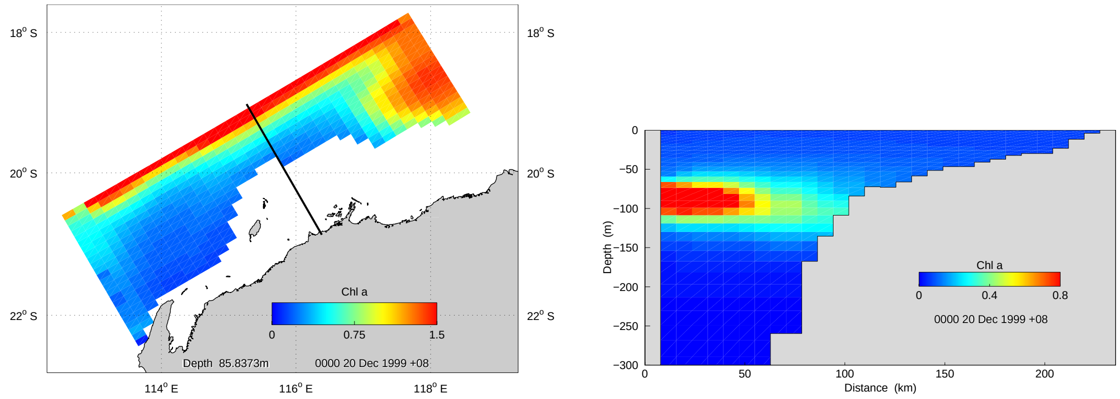

(a) Plan

(b) Section

Figure 4.3.4: Chl*a* concentration at 20 December 1999: no vertical diffusion.

Analysis of these scenarios provides a clue as to the source of nitrate. Removing the horizontal advective nitrate flux at the open boundaries through the whole water column results in a decrease in Chl*a* concentration in the SCM by a factor of approximately two (figure 4.3.2). The SCM deepens to below 100 m depth (figure 4.3.2 (b)) and the base of the SCM corresponds to ~125 m in figure 4.3.2 (a), with Chl*a* concentrations in this region again less than half that of the reference case. The nitrate concentration at depth is decreasing over the course of the year (figure 4.3.5) due to nitrate losses into the SCM sustained by vertical fluxes. The SCM is maintained by nitrate from the initial condition and it is anticipated that as nitrate at depth is depleted further with time the SCM will slowly erode.

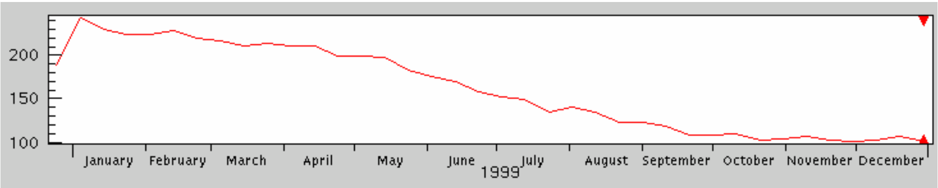

Figure 4.3.5: Nitrate time series at mid-domain, 200 m depth (mg N m^{-3}).

When nitrate fluxes through the open boundaries into the deep layer are allowed (figure 4.3.3), the Chl*a* distribution is similar to the reference distribution. The SCM is at approximately the same depth with slightly lower concentration (figure 4.3.3 (b)). This suggests that direct horizontal advection of nitrate into the SCM is not the dominant mechanism for maintaining the SCM, rather horizontal advection into the deeper layers is required, which is then fed to the SCM via vertical processes. Nitrate concentrations on the open boundaries that may potentially be directly advected into the SCM vary from 1 to ~55 mg m^{-3}, depending on the location on the boundary and time of year.

Preventing vertical nitrate diffusion (figure 4.3.4) resulted in an overall decrease in Chl*a* concentration to a steady state. Maximum concentrations in the SCM near the shelf edge decreased from ~1 mg m^{-3} at 75 m to ~0.4 mg m^{-3} at 104 m (i.e. 60% reduction, figure 4.3.4 (b)). The depth of the SCM generally deepened by 20 to 30 m, and productivity in the SCM decreased. Closer to the open boundaries the decrease in maximum SCM concentration was not as great (~20% reduction) and the SCM was ~10 m shallower due to direct advection of nitrate through the open boundaries supporting productivity; e.g. figure 4.3.4 (a) shows that in the interior of the domain away from influence of open boundaries the Chl*a* (and nitrate, figure 4.3.6) concentration in the SCM is low without the vertical diffusive source of nitrate. A decrease in nitrogen supply results in a deeper SCM (section 4.2), hence when the diffusive flux of nitrate is absent the SCM responds by deepening. Existing nitrate is depleted as the SCM moves lower in the water column until a new equilibrium is established where existing nutrient fluxes can again support the SCM.

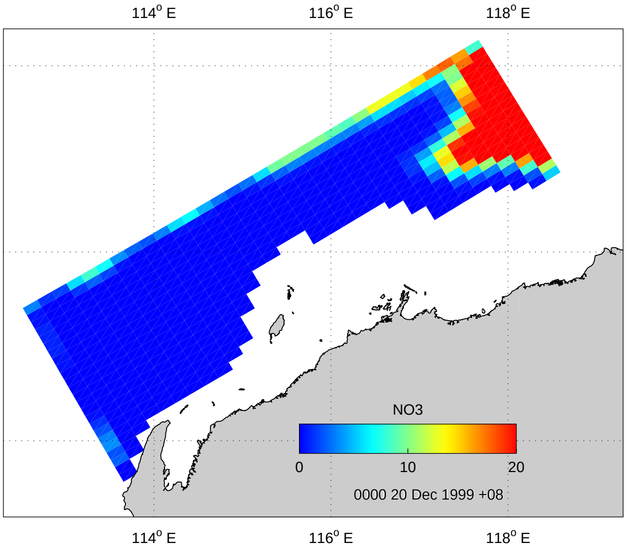

Figure 4.3.6: Nitrate concentration (mg N m^{-3}) at 20 December 1999 at 85 m depth: no vertical diffusion scenario.

The fluxes of nitrate due to horizontal advection through each boundary from the surface to 80 m and vertically through the 80 m layer due to advection and diffusion were computed. These are presented as normalised fluxes (i.e. the fluxes per m^2 of boundary) through each boundary over the year (figure 4.3.7) and an arbitrary spring neap cycle (figure 4.3.8). The nitrate fluxes are observed to undergo large fluctuations on time scales of the semidiurnal tide, spring neap cycle and to a lesser extent the seasonal cycle. Fluxes through the north-eastern boundary (NEB) are the largest followed by the offshore boundary (OB). The south western boundary (SWB) and vertical advective (VA) fluxes are much smaller in comparison and the vertical diffusive (VD) flux is almost negligible. It should be noted, however, that the VD flux is always positive (nitrate supplied to the surface) and does not undergo oscillation. When averaged over tidal cycles or spring neap cycles this component is guaranteed of supplying nitrate to the SCM whereas the advective components may not, thus the fluxes should be temporally averaged to provide a clearer picture of the net supply of nitrate to the SCM. Also, localised nitrate supply may be important rather than net areal means.

The mean normalised (per m^2 of boundary, mg N m^{-2} s^{-1}) and total (through each boundary area, mg N s^{-1}) fluxes over the simulation period 1999 are presented in table 4.3.1. Note that a positive flow indicates flow out of NEB, into OB and into SWB.

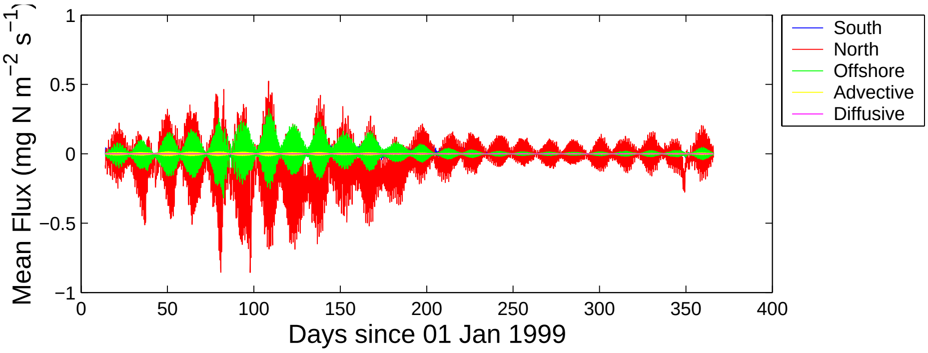

Figure 4.3.7: Normalised fluxes through each boundary, January to December.

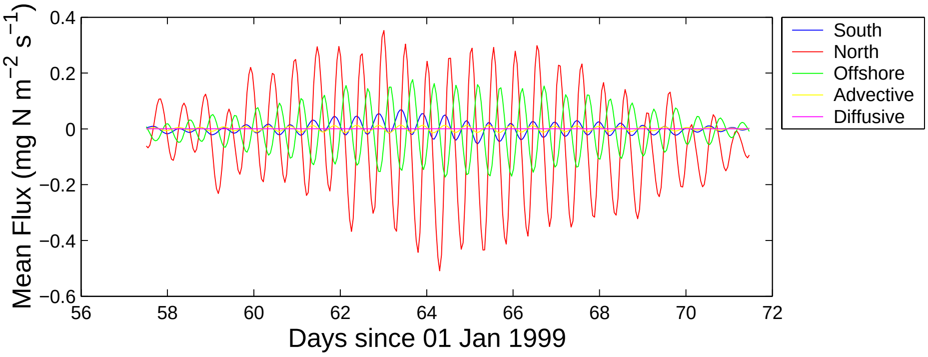

Figure 4.3.8: Normalised fluxes through each boundary, spring neap cycle.

Table 4.3.1: Mean fluxes through each boundary. Units for normalised fluxes are (mg N m^{-2} s^{-1}) and for total fluxes are (mg N s^{-1}).

	NEB	OB	SWB	VA	VD
Normalised	-5.59×10^{-2}	-7.79×10^{-4}	-6.24×10^{-2}	2.62×10^{-5}	4.77×10^{-4}
Total	-9.54×10^{5}	-4.22×10^{4}	-1.05×10^{6}	2.51×10^{6}	4.56×10^{7}

The mean fluxes integrated over each boundary indicate that, horizontally, nitrate is enters the region through the NEB and leaves through the SWB. Horizontal exchange through the offshore boundary is small. This can be seen in figures 4.3.9 and 4.3.10 which show (a) plan views through 80 m and (b) sections along the boundary of the distribution of mean flux along the NEB and OB. Note that these figures represent the mean flux of nitrate in each grid cell, with units of mg N s^{-1}, hence flux magnitude is dependent on the cross sectional area of the cell and thus direct comparisons between plan and section views are not meaningful.

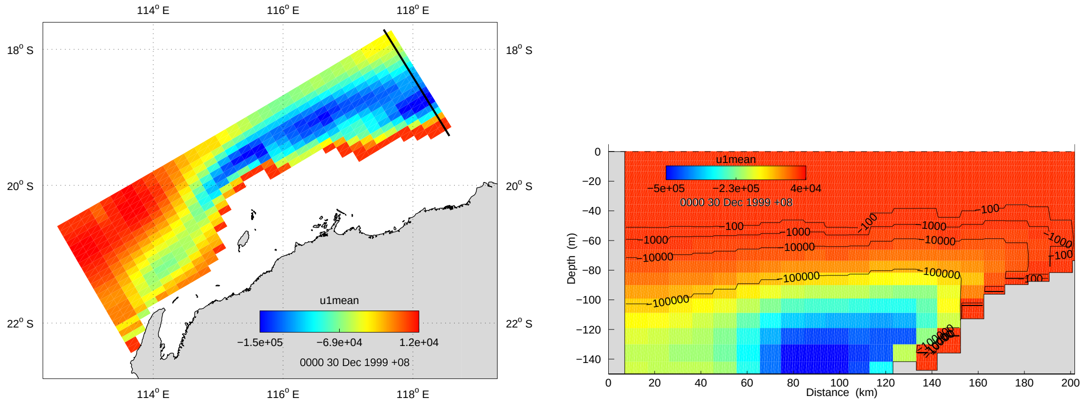

(a) Plan view through 80 m (b) Section through the NEB

Figure 4.3.9: Mean flux in the long-shelf direction (mg N s^{-1}).

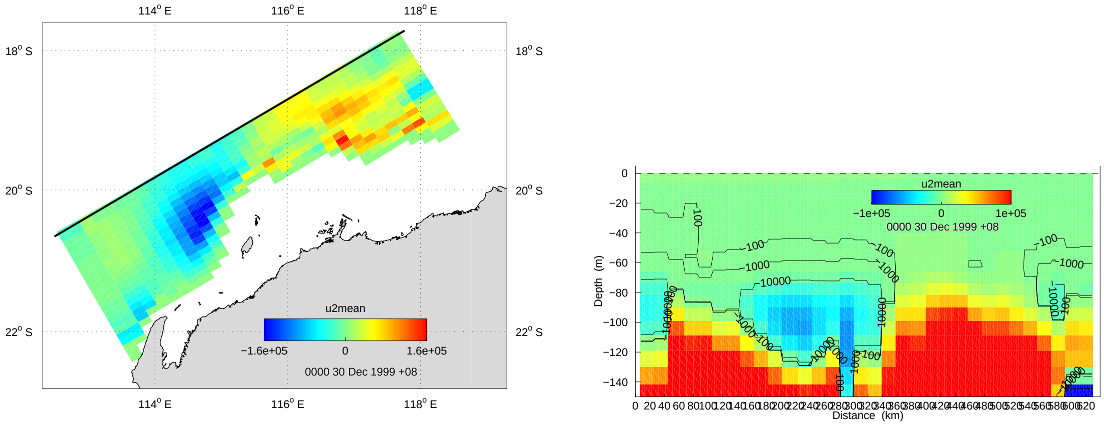

(a) Plan view through 80m (b) Section through the OB

Figure 4.3.10: Mean flux in the cross shelf direction (mg N s^{-1}).

The section through the NEB, figure 4.3.9 (b), exhibits nitrate flux into the domain along the entire boundary, with the flux increasing with depth (advective nitrate flux scales linearly with concentration, and nitrate is approximately increasing linearly with depth). The NEB plan view, figure 4.3.9 (a), shows a flux plume of nitrate entering through the NEB and following the shelf edge to the SWB. This correlates with the OB plan view, figure 4.3.10 (a), which shows onshore flux in the south western end of the domain where the flux plume flows towards the shore, and offshore flux in the north eastern end where flow along the shelf edge moves in an offshore direction. The section through the OB, figure 4.3.10 (b), exhibits two cells corresponding to this offshore and onshore flow.

Table 4.3.1 indicates that the net mean flux of nitrate from all boundaries is negative, i.e. more nitrate leaves the region through the open boundaries above 80 m than enters. Larger fluxes leaving the domain through the SWB must occur above 80 m depth, since the flux plume is observed to diminish towards the SWB in figure 4.3.9 (a). More importantly, since the net mean open boundary flux is negative, vertical processes must be the dominant mechanism responsible for nitrate supply into the SCM in the domain under consideration, with vertical diffusion providing 17 times more than vertical advection. This vertical input must be balanced by particulate export of nitrogen and a small amount of horizontal advection through the SWB. This NO_3 supply mechanism is consistent with the scenario experiments, where the removal of nitrogen supply via vertical diffusion resulted in significant decreases in SCM concentration in the model interior. In the absence of vertical diffusion, the SCM adjusts to a new equilibrium position which appears to be maintained by vertical advection in the interior (total VA through 104 m is 2.98×10^6 mg N s^{-1} in the absence of VD) and horizontal advective fluxes near the NEB and OB.

The spatial distributions of vertical nitrate fluxes are illustrated in figures 4.3.11 and 4.3.12 for VD and VA respectively. Vertical diffusion is responsible for the largest time-averaged supply of nitrogen in localised zones (figure 4.3.11 (a), up to 4×10^5 mg N s^{-1} 200 km^{-2}). This occurs predominantly near the north-eastern side of the domain near the shelf slope, with mean diffusive fluxes near the SWB approximately half that near the NEB. This flux is always directed into the SCM. Vertical mixing is large at the shelf slope due to the bottom boundary layer, and sufficient nitrate is present at depth to drive a larger flux in this region. Further offshore the flux is reasonably uniform over the domain. While the flux is locally enhanced at the shelf slope, the diffusive flux over the rest of the domain is sufficiently large that it dominates the total area-integrated vertical flux through the 80 m plane. In comparison, large variability exists in space with the vertical advective fluxes (figure 4.3.12). Large positive (upwards) mean vertical advective fluxes are confined to very localised areas (magnitudes up to 1.8×10^5 mg N s^{-1} 200 km^{-2}), with negative fluxes of the same magnitude often in close proximity, particularly in the north-eastern section of the domain.

Instantaneous VA fluxes show a strong semidiurnal and spring neap periodicity while the VD flux is always directed into the SCM (figure 4.3.13). The vertical advective flux at 80 m may be large (during maximum spring flood tides over the shelf break) in comparison with the vertical diffusive flux due to the tidal heaving of the nutricline through the 80 m depth level. The SCM also heaves with the tide, hence any increased flux observable at a fixed depth due to this mechanism is not necessarily available for uptake within the SCM. The mean advective flux displayed in figure 4.3.12 averages out this oscillatory motion, and accounts for any nitrate that may be uptaken on timescales of tidal upwelling.

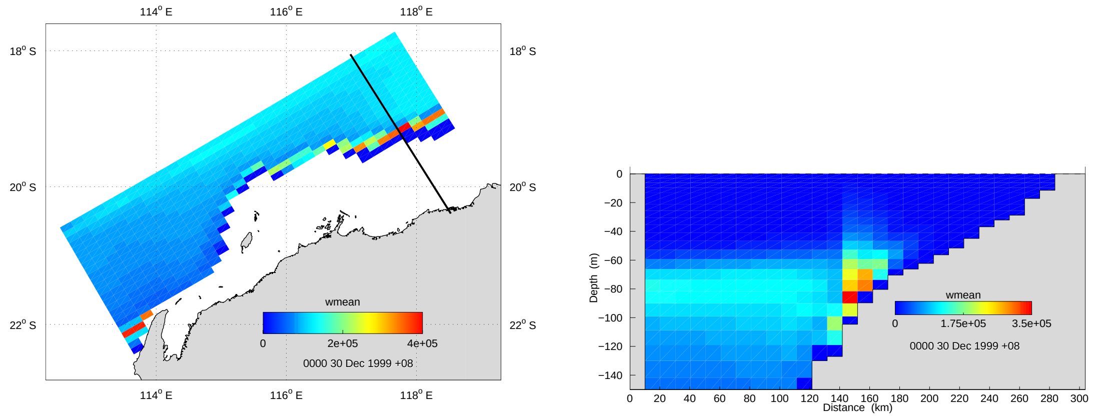

(a) Plan view through 80 m (b) Port Hedland section

Figure 4.3.11: Mean vertical diffusive flux (mg N s^{-1}).

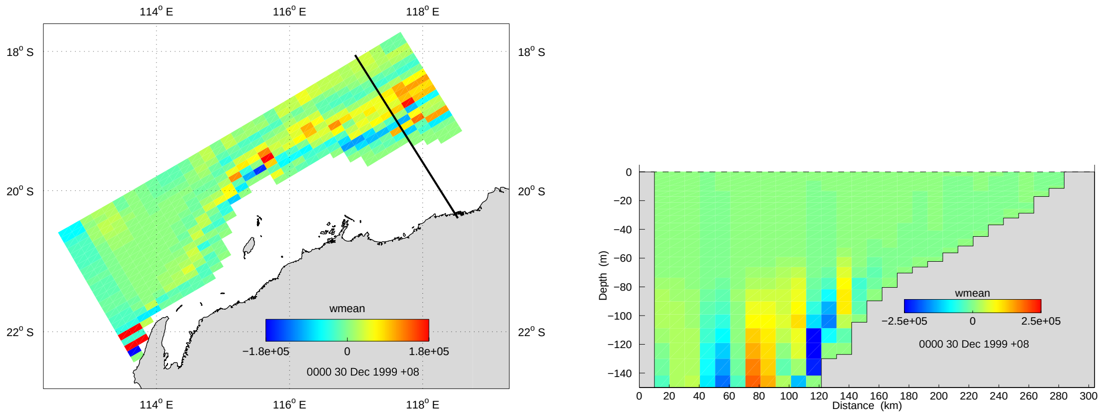

(a) Plan view through 80 m (b) Port Hedland section

Figure 4.3.12: Mean vertical advective flux (mg N s^{-1}).

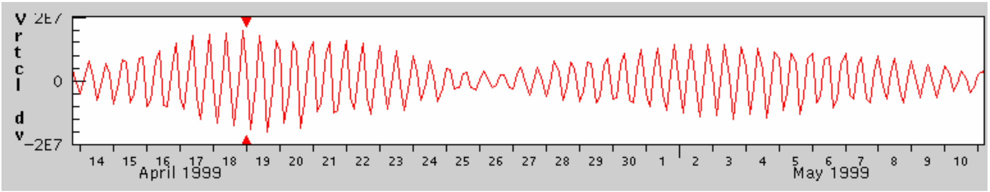

Figure 4.3.13 (a): Sample maximum instantaneous vertical advective flux through 80 m depth. This time series was taken at 250 m depth on the Port Hedland section.

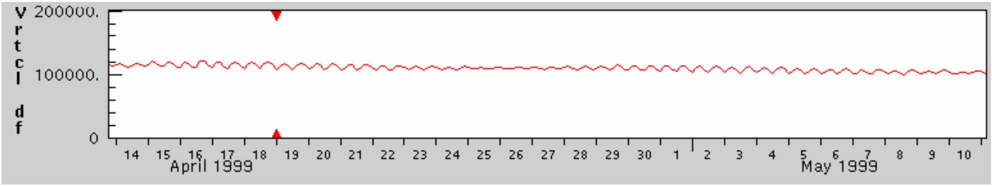

Figure 4.3.13 (b): Maximum instantaneous vertical diffusive flux through 80 m depth (mg N s^{-1}) at the same location as (a).

This analysis suggests that the SCM is maintained by nitrate supplied through vertical diffusion and advection, with diffusion responsible for the bulk of nitrate supply and vertical advection capable of locally increasing nitrate flux into the SCM. The horizontal fluxes are, however, important for maintaining the deep pool of nitrate that may be made available to the SCM via vertical processes. If the system is perturbed so that the SCM establishes a new equilibrium position in the water column, then the balance of nitrate flux contributions may also alter. The mean vertical flux through 80 m from table 4.3.1 is 43 mg N m^{-2} d^{-1}, or a little less than half the upper bound of 110 mg N m^{-2} d^{-1} estimated for vertical nitrate supply by Holloway et al. (1985). Given that the model phytoplankton biomass matches observed magnitudes, and model phytoplankton growth rates in the SCM are relatively high, it seems unlikely that the model is underestimating phytoplankton production.

There are a variety of mechanisms that may potentially generate large positive vertical velocities or enhance vertical diffusion. The dissipation of energy by internal solitons, as suggested by Holloway et al. (1985) would certainly increase vertical diffusion, however these processes are unable to be captured by the model in its current form. The strong barotropic currents generated by the tide interacting with the bottom can generate a deep bottom boundary layer, enhancing diffusion in this region. Divergences of flow in the bottom boundary layer, driven by the tide, may result in Ekman pumping out of the bottom boundary layer, enhancing vertical flow. Ekman pumping due to the wind is another potential mechanism for generating large vertical velocities The exact mechanisms responsible for generating the vertical dynamics require further investigation.

The long-shore fluxes in this analysis are somewhat compromised by the prescription of the CARS climatology for nitrate at the boundary. Whenever flow is into the domain (i.e. south-westwards) water having a concentration specified from this climatology enters the domain. If processes were occurring upstream of this boundary such that nitrate were depleted, then the actual flux through the north-eastern boundary into the domain would be less than that specified by CARS. In particular, the deep shelf always acts as a source for the NEB, even though, in reality, the region north of this boundary would be undergoing the same vertical nitrate export processes as the modelled region. In this context it can only be the offshore boundary that is capable of continuously supplying nitrate to the deep shelf waters, assuming an inexhaustible supply exists in the deep ocean interior.

Table 3.4.1 indicates that the total mean nitrate supplied via hydrodynamic process is 10^4 to 10^7 mg N s^{-1}, or up to 10 kg N s^{-1}. This is large in comparison to terrestrial sources of nitrate. The phosphorus load from the Pilbara Rivers is roughly estimated as 0.34 kT P yr^{-1} (Water and Rivers Commission, pers. comm.). Assuming Redfield ratios this translates to approximatly 2.38 kT N yr^{-1}. There exist 11 rivers comprising the Pilbura system, with a total annual flow of ~2390 GL.

The nitrogen flux equates to ~0.075 kg s^{-1}, which is insignificant in comparison to the oceanic fluxes. Groundwater supply of nitrogen along the Pilbura coast is addressed by Appleyard (2000). The Pilbura region was divided into six zones with different characteristics of aquifer. Groundwater discharge of all zones is estimated as ~138 x 10^6 m^3/yr along a total length of coastline of 860 km. The total load of all aquifers is ~0.044 kg s^{-1}, which can again be assumed to be negligible in comparison to the oceanic fluxes. Although these fluxes are small, they are fed directly into the shallow coastal zone that receives little nitrate from oceanic processes. The terrestrial inputs may therefore be important for biota dependent on nitrate in the coastal zone.

4.4 Spring neap tidal cycle

The chlorophyll signature at the surface exhibits an oscillation on the time scale of the spring neap tidal cycle that is indicative of more complex subsurface phenomena. Surface Chl*a* increases to maximum concentrations at, and shortly after the peak spring tide, particularly in a band near the north-eastern open boundary. Surface Chl*a* then decreases during the neap tide (figure 4.4.1). Often the band of high Chl*a* concentration resides offshore as a mid shelf Chl*a* maximum during the spring tide (figure 4.4.2 (a)), then weakens and/or moves shoreward during the neap tide (figure 4.4.2 (b)).

(a) Sea level (m)

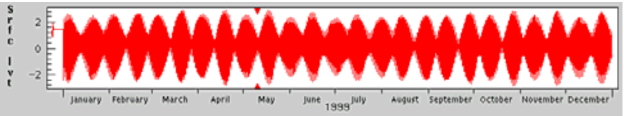

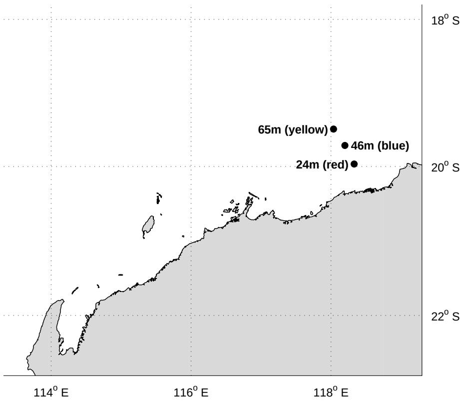

(b) Chlorophyll (mg m^{-3})

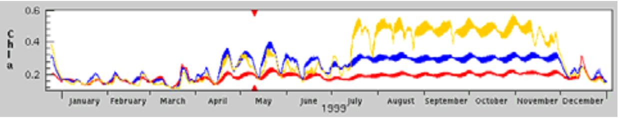

Figure 4.4.1: Spring neap chlorophyll oscillation; (a) sea level and (b) Chl*a*. Time series are taken at the surface locations indicated; the depths quoted correspond to the bottom depth.

This cycling of the surface Chl*a* concentration is related to turbidity levels in the coastal zone. During the neap tide the barotropic tidal currents are relatively weak, generating weak bottom stress which results in lower resuspension of fine sediment. The fine sediment (e.g. silt 250 µm particle size) concentrations in the water column are therefore low (figure 4.4.3 (a)). This results in little attenuation of light (figure 4.4.3 (b)) allowing a horizontally uniform light distribution in the water column. The light regime has little effect on the cross shelf distribution of phytoplankton production, allowing the SCM to intersect the slope at ~75 m (figure 4.4.3 (c)). Any nitrate undergoing vertical motion must pass through the SCM, where nitrate is consumed by phytoplankton. This makes it difficult for nitrate rich water to reach the coastal zone, as the SCM forms an effective barrier isolating the nitrate depleted shallow waters from the nitrate rich deeper water (figure 4.4.3 (d)).

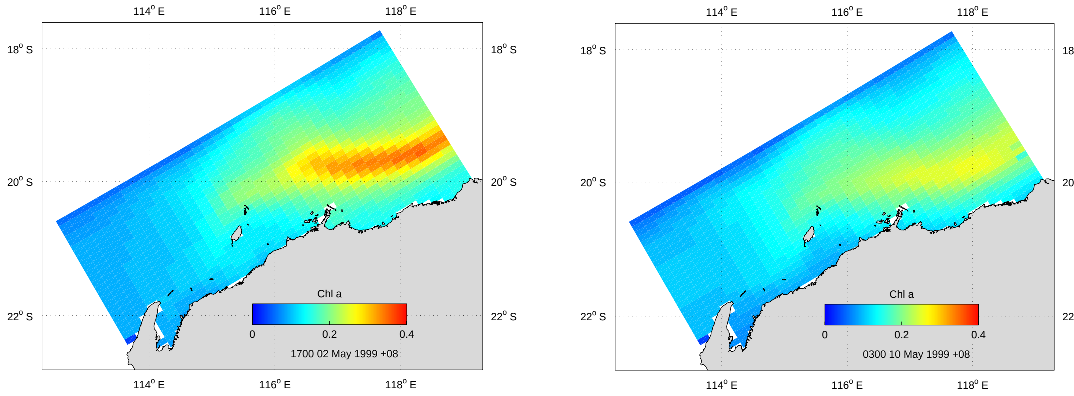

(a) Spring tide

(b) Neap tide

Figure 4.4.2: Surface Chl*a* (mg m^{-3})

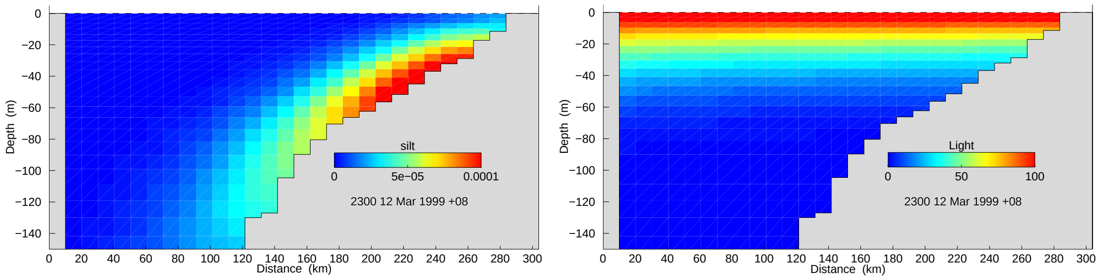

(a) Silt concentration (kg m^{-3})

(b) Light distribution (W m^{-2})

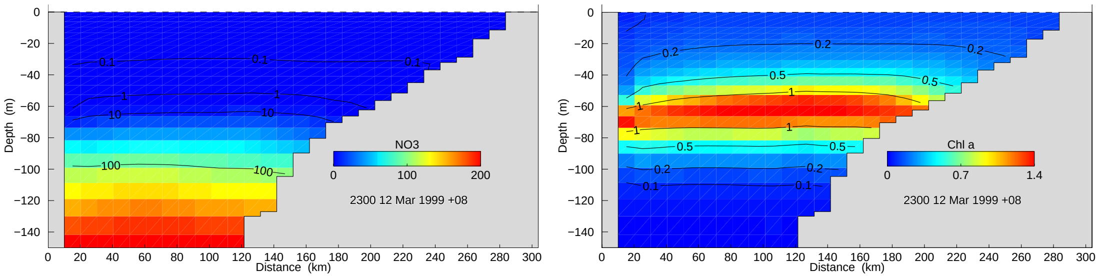

(c) Chl*a* concentration (mg m^{-3})

(d) NO$_3$ concentration (mg N m^{-3}).

Figure 4.4.3: Neap tide sections originating from Port Hedland.

The tidal velocities are much greater during the spring tide, resulting in larger bottom stress and sediment resuspension. As a consequence the silt concentrations in the water column are significantly larger (figure 4.4.4 (a), up to two orders of magnitude greater inshore), leading to significant attenuation of light inshore (figure 4.4.4 (b)). As noted earlier, when light availability decreases the SCM be comes shallower and a shoreward decrease in the depth of the SCM is evident (figure 4.4.4 (c)). When the SCM enters the mixed layer phytoplankton are mixed to the surface, pushing the surface Chl*a* signature offshore. The SCM no longer intersects the slope, creating a pathway that nitrate may potentially follow to the inshore zone without having to pass through the SCM (figure 4.4.4 (d)). This results in elevated nitrate levels in the coastal zone, e.g. nitrate is between 0.1 and 1 mg N m^{-3} in water depths less than 40 m during the spring tide but less than 0.1 mg N m^{-3} during the neap tide. This supply of new nitrate is available to fuel growth. As fine sediment concentrations become larger inshore (e.g. through lower critical shear stress for some sediment fractions) this effect becomes more pronounced, even if all other physical processes (e.g. tidal range, vertical mixing) remain constant.

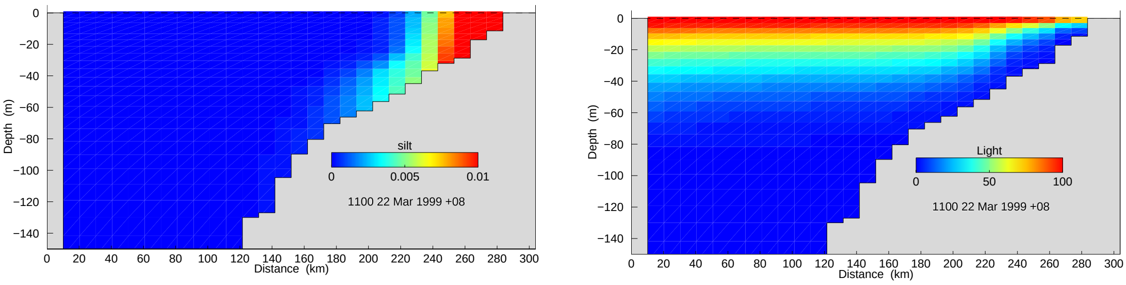

(a) Silt concentration (kg m^{-3}) (b) Light distribution (W m^{-2})

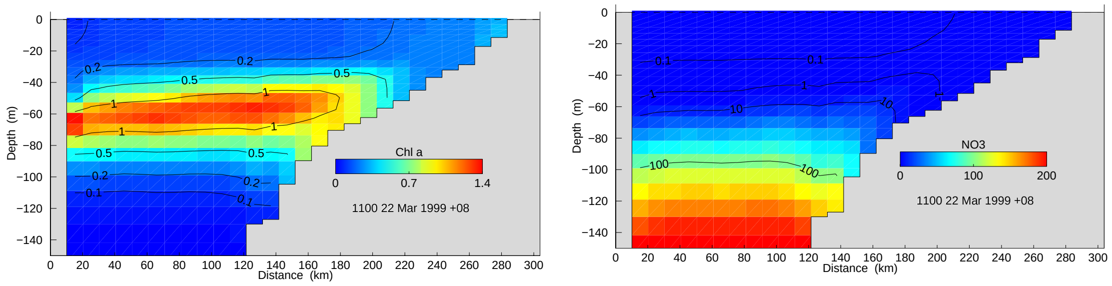

(c) Chl*a* concentration (mg m^{-3}) (d) NO_3 concentration (mg N m^{-3})

Figure 4.4.4: Spring tide sections originating from Port Hedland.

The shelf break at 50 to 80 m depth appears to be the zone where greatest variability occurs in biomass, suspended sediments, light and nutrients. This is related to the vertical mixing regime in the water column. A surface boundary layer exists with depths ranging from ~20 to 60 m, depending on the forcing conditions. Below this the pycnocline exists followed by a region where vertical gradients of water properties may be maintained. Near the sea floor a well mixed bottom boundary layer exists with thickness ~3 to 8 m, again depending on the ambient forcing (the large barotropic tides on the NWS are capable of generating bottom boundary layers much larger than this).

As the depth of the sea floor decreases to zero towards the coast, the surface and bottom boundary layers converge up to a point where they intersect, or overlap, and the water column is well mixed from the surface to the bottom. This boundary intersection zone is associated with mixed water columns that are deeper than either the surface or bottom mixed layers in isolation. This overlap phenomena is illustrated in figure 4.4.5, where the vertical diffusivities (proportional to vertical mixing) are displayed in a section originating from Port Hedland.

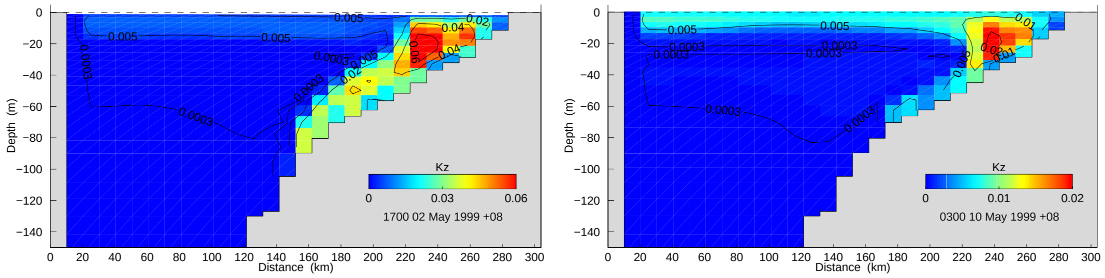

(a) Spring tide (b) Neap tide

Figure 4.4.5: Vertical diffusivities ($m^2 s^{-1}$).

The surface and bottom boundary layers are easily identified in this figure, as is the overlap zone extending ~80 km offshore with very large maximum diffusivities of ~0.06 $m^2 s^{-1}$ during the spring tide and smaller maximum diffusivities of ~0.02 $m^2 s^{-1}$ during the neap tide. The typical diffusivities in the mixed layer offshore are 5 x 10^{-3} $m^2 s^{-1}$ near the surface and ~3 x 10^{-4} $m^2 s^{-1}$ above ~70 m. Note that the SCM lies below this zone at 70 to 80m. Even though the SCM lies below the surface mixed layer, as soon as it encounters the boundary overlap zone, mixing to the surface results. This region is thus associated with the band of maximum surface biomass, as is illustrated in figure 4.4.6 (a). The top of the SCM lies at ~40 m and intersects the boundary overlap zone ~80 km offshore where mixing to the surface results. The smaller diffusivities generated during the neap tide result in less Chl*a* mixed to the surface and a corresponding lower surface biomass concentration (figure 4.4.6 (b)). Inshore of the boundary overlap region (i.e. less than ~30 m depth) biomass is low as a result of nitrate limitation. Consumption of nitrate in the SCM and overlap zone strips nitrate from any water transported inshore and thus prevents an accumulation of nitrate in the shallow coastal zone (figure 4.4.7).

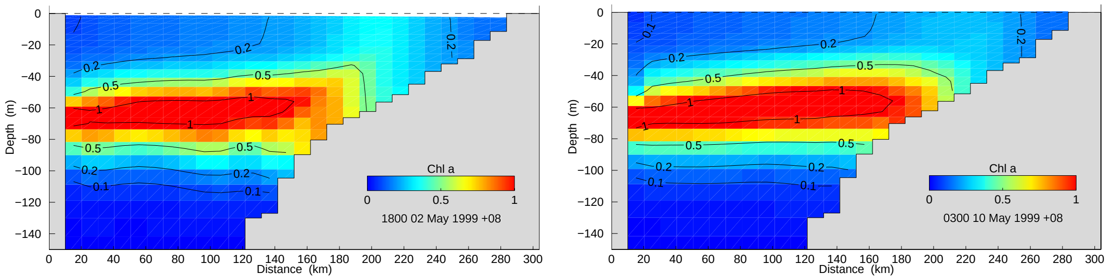

(a) Spring tide (b) Neap tide

Figure 4.4.6: Chlorophyll sections originating from Port Hedland (mg m^{-3}).

Primary productivity appears to have the greatest variability near the north-eastern open boundary. In this region the continental slope has the most gentle gradient, allowing the zone of surface and bottom boundary layer overlap to extend offshore to the greatest extent. Any variation in boundary layer thickness will therefore manifest as much larger horizontal changes in the offshore extent of the boundary overlap zone, contributing to variability of all variables dependent on this zone. This is more evident in inter-annual variability rather than in the spring neap cycle.

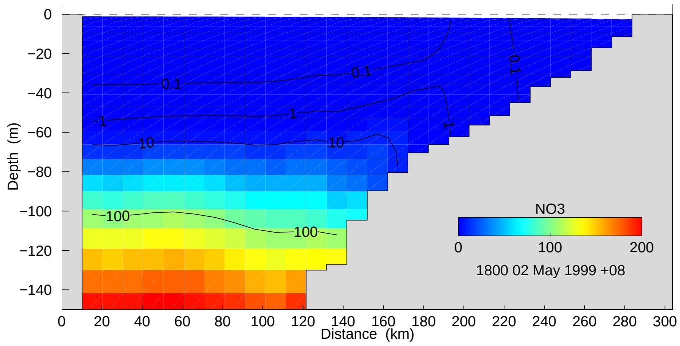

Figure 4.4.7: Nitrate sections originating from Port Hedland at spring tide (mg N m^{-3}).

The spring neap oscillation appears to be a combination of two process; vis. an offshore movement of the SCM and associated surface Chl*a* signature due to greater turbidity, and an increase in surface Chl*a* concentration due to greater mixing in the boundary overlap zone during the sprig tide. Nitrate is capable of bypassing the blocking effect of the SCM and entering the coastal zone when resuspension of fine sediment pushes the SCM offshore. At other times nitrate concentration remains low in the shallow regions, hence phytoplankton concentration is low due to severe nitrogen limitation. These observations generally agree with the findings of Tranter and Leech (1986) who found that mixed layer Chl*a* concentration during sprig tides was twice as high as that during neap tides. Also, shoreward of the 50 m isobath the SCM was not evident as a distinct peak, surface and depth integrated biomass was low and this area was rarely affected by high nitrate intrusions (>5 µg at L^{-1}).

4.5 Seasonal variability

Time series of Chl*a* concentration for the years 1996 to 1999 at the locations depicted in figure 4.5.1 are displayed in figures 4.5.2 (a) to (d). These time series are created from data output at 10 day intervals and therefore do not contain high frequency (e.g. tidal) variations.

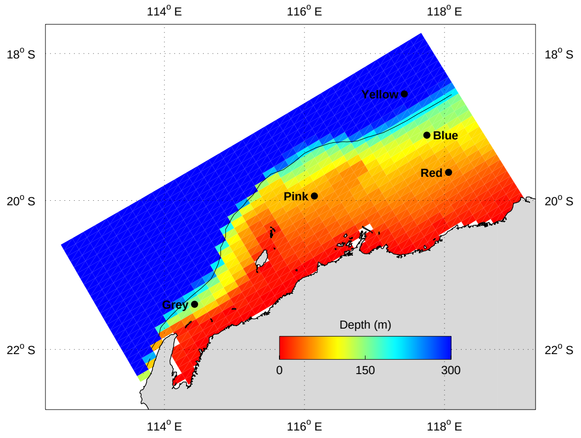

Figure 4.5.1: Locations of Chla time series.

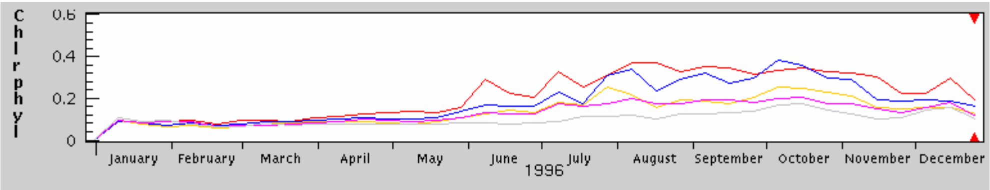

Figure 4.5.2 (a): Surface Chlorophyll *a* concentration (mg m^{-3}): 1996.

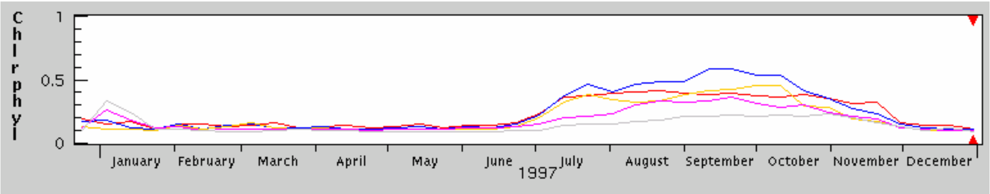

Figure 4.5.2 (b): Surface Chlorophyll *a* concentration (mg m^{-3}): 1997.

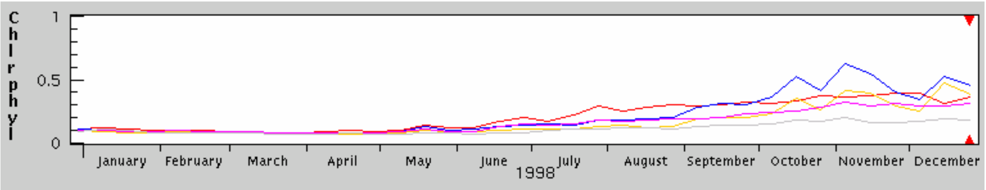

Figure 4.5.2 (c): Surface Chlorophyll *a* concentration (mg m^{-3}): 1998

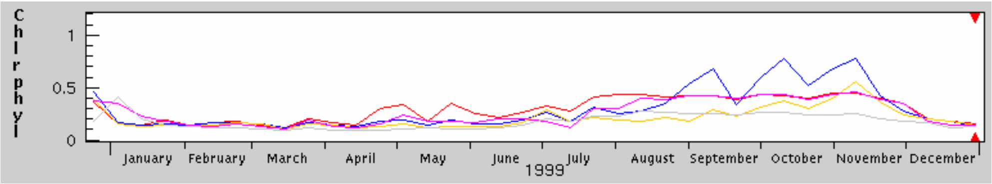

Figure 4.5.2 (d): Surface Chlorophyll a concentration (mg m^{-3}): 1999.

All the years simulated exhibit a tendency for elevated surface Chl*a* in the latter part of the year, particularly near the north-eastern open boundary. This elevated Chl*a* begins in around June and lasts until December. The North West Shelf region is essentially subject to only two seasons; the wet when the northeast monsoon activity is in effect lasts from approximately January to April and the dry season is subject to the southeast trades from May to October. In the wet season the maximum surface Chl*a* is low (~0.2 mg m^{-3}) and resides closer to the coast with the SCM being more concentrated (figure 4.5.3) whereas in the dry season the surface Chl*a* is greater (~0.6 mg m^{-3}), lies further offshore and the SCM is more diffuse (figure 4.5.4). Both figures 4.5.3 and 4.5.4 are taken at the high spring tide, hence differences are due to seasonal variability.

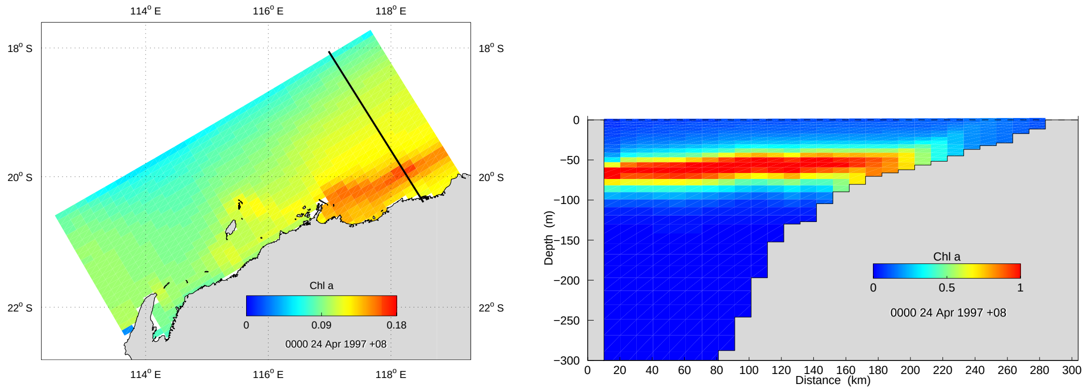

Figure 4.5.3: Wet season Chl*a* surface distribution (mg m^{-3}).

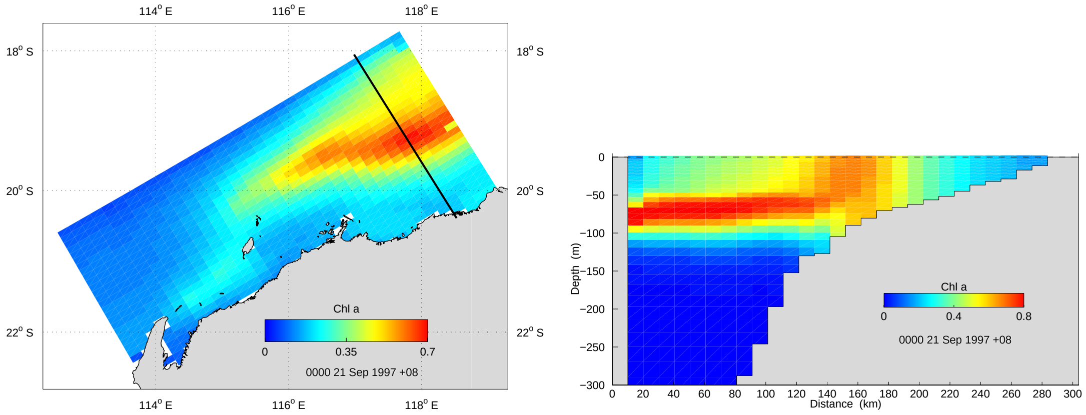

Figure 4.5.4: Dry season Chl*a* surface distribution (mg m^{-3}).

Tranter and Leech (1986) identified a seasonal pattern described as a ‘phytoplankton-dispersed’ phase during winter where the SCM was more vertically diffuse and a ‘phytoplankton-stratified’ phase during summer where the SCM was a concentrated band below the mixed layer. These authors defined summer as the pre-monsoon and monsoon period (October to March, encompassing the wet season) and winter as April to July (encompassing the dry season). The timing of these findings differs a little to the ‘diffuse’ and ‘stratified’ phases evident in the simulations. These authors also found the greatest seasonal variability in phytoplankton concentration occurring at the shelf break, with low concentration and seasonal variability inshore from 50 m and a permanent SCM at approximately 75 m beyond the shelf break. This appears consistent with the model output.

The seasonal variability evident in the model results is due to a deeper mixed layer in the dry season pushing the zone of boundary layer overlap (hence the region where the SCM is mixed to the surface) offshore. The vertical diffusivities for wet and dry seasons are displayed in figure 4.5.5, from which it is observed much larger surface mixing is taking place in the dry. The boundary overlap zone is pushed offshore ~140 km during this season, compared to ~70 km in the wet. Significantly larger mixing is taking place off the shelf from the surface to 40 m depth (e.g. Kz > 0.02 m^2 s^{-1}).

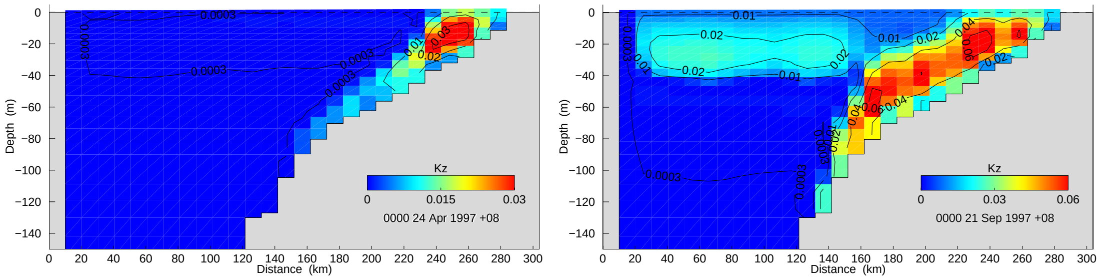

(a) Wet season (b) Dry season

Figure 4.5.5: Vertical diffusivity (m^2 s^{-1}).

The mixed layer depth was calculated on the basis of when the turbulent kinetic energy exceeds a certain threshold (10^{-5} W kg^{-1}; Buchard et al. 1999, p26). The mixed layers are displayed for the wet and dry seasons in figure 4.5.6. Maximum mixed layers are in the zone of boundary overlap, which is much deeper and further offshore for the dry season. There is considerable variability in these mixed layer depths on time scales of the diurnal and spring neap tidal cycle (figure 4.5.7) and thus mixed layers do vary about the snapshots presented in figure 4.5.6. However, the general seasonal trend of larger mixed layers in the dry is observed in figure 4.5.7.

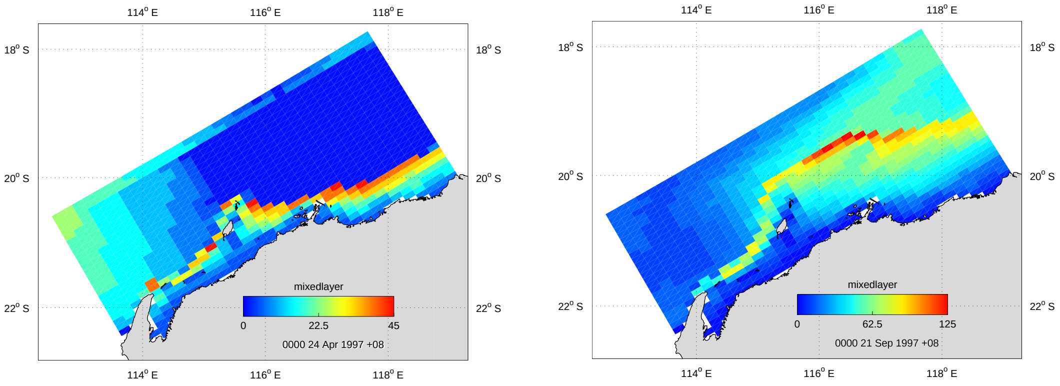

(a) Wet season (b) Dry season

Figure 4.5.6: Mixed layer depth (m).

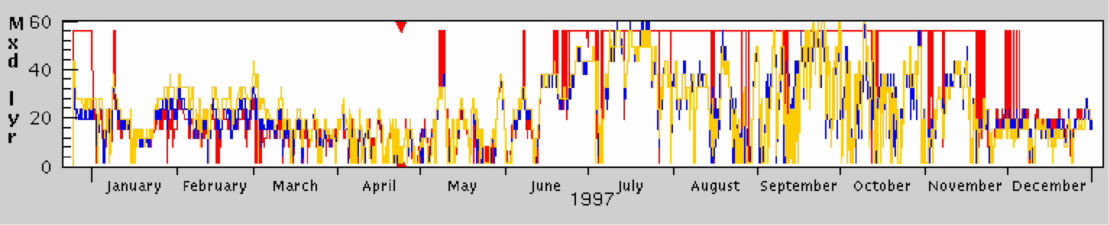

Figure 4.5.7: Timeseries of mixed layer depth (m) for 1997 taken at the red, blue and yellow locations depicted in figure 4.5.1.

The vertical mixing scheme used in the model is the k-ε scheme (e.g. Burchard et al. 1998). In this scheme the vertical diffusivity is proportional to the product of the square root of turbulent kinetic energy (TKE $m^2\,s^{-2}$) and the turbulence length scale, which is in turn proportional to TKE and the normalised dissipation rate, ε ($m^2\,s^{-3}$). TKE is treated as a non-conservative tracer undergoing advection and vertical diffusion with source terms of shear and buoyancy production and a sink of dissipation where;

$$P = V_z \left[\left(\frac{\partial u_1}{\partial z}\right)^2 + \left(\frac{\partial u_2}{\partial z}\right)^2 \right] \qquad 4.1$$

is the shear production with u_1 and u_2 velocity components and V_z the vertical viscosity, and;

$$B = -K_z N^2 \qquad 4.2$$

is the buoyancy production were N^2 is the Brunt-Vaisala frequency and K_z is the vertical diffusivity. An increase in mixed layer depth due to increased vertical diffusion is basically a result of either increased TKE production (P or B) or a decrease in dissipation, ε. The wind stress applied at the surface has a major impact on the shear within the surface Ekman layer, however the windspeed exhibits no clear strengthening in the dry season (figure 4.5.8). Windspeeds peak at up to 10 m s^{-1} in June and July with a mean speed around 5 m s^{-1} during August to October. The vertical shear (i.e. P/V_Z) at 62 m in the water column is displayed in figure 4.5.9, again showing the lack of wet/dry season variability. The Brunt-Vaisala frequency (figure 4.5.10) does exhibit a clear decrease in magnitude during the dry season, which results in the larger vertical diffusivities in this season. A decrease in N^2 is indicative of a decrease in stratification. As mentioned in section 3, the temperature and salinity distributions were relaxed to output from a global model (ACOM3), and the decrease in stratification evident in the biogeochemical model stems from a deepened mixed layer in the global model solution. The biogeochemical model mixed layer therefore attempts to mirror that of the global model through regulation of the buoyancy production. Profiles of temperature and salinity from ACOM3 at a location in the biogeochemical model grid (19°16'S, 118°12.5'E) are displayed in figure 4.5.11. It is observed that both temperature and salinity are uniform to a depth of ~20 m in February, indicative of a 20 m mixed layer depth, but deepen to ~100 m in September. The deepening of the mixed layer in the dry season in ACOM3 output is essentially the result of atmospheric forcing, specifically larger zonal wind stress in the dry in conjunction with heat loss in the dry (leading to convective mixing) and net heat gain in the wet (Schiller, pers. comm.).

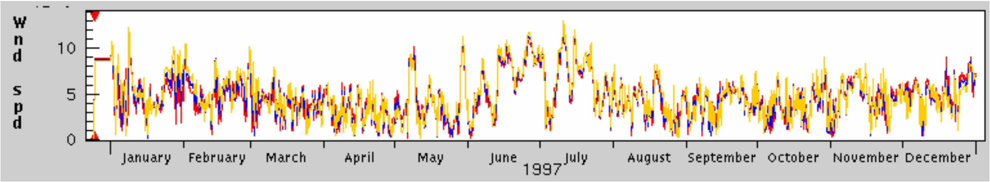

Figure 4.5.8: Annual cycle of windspeed (m s^{-1}) for 1997 taken at the red, blue and yellow locations depicted in figure 4.5.1.

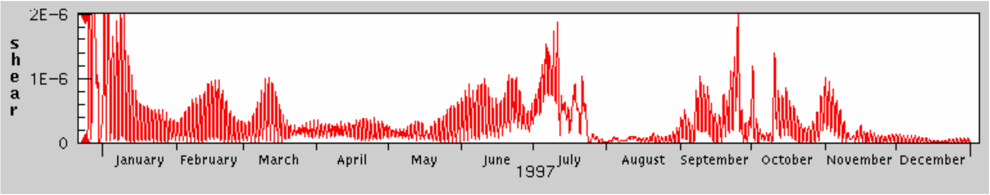

Figure 4.5.9: Annual cycle of vertical current shear (s^{-2}) at 62 m.

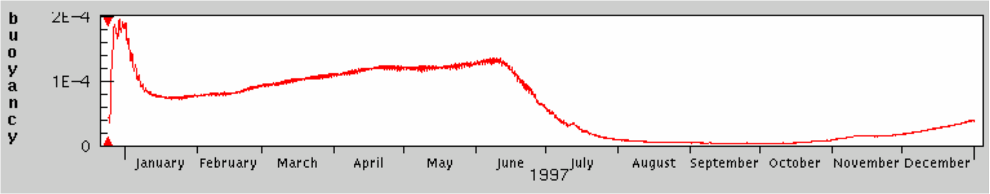

Figure 4.5.10: Annual cycle of Brunt-Vaisala frequency (s^{-2}) at 62 m.

The Chl*a* concentration for 1997 to 1999 taken at a depth of 56 m is displayed in figure 4.5.12 (a) to (c). This time series is output at 3 hour intervals, hence the spring neap oscillation is clearly observed. This oscillation appears stronger and is associated with larger biomass in the wet season, e.g. in 1997 the biomass peaks at ~1.5 mg Chl*a* m^{-3} in early March, but decreases to ~0.5 mg Chl*a* m^{-3} in July. This trend of decreasing biomass in the dry, or traditional winter season, is observed for all years at all locations across the shelf, although it is less pronounced at the furthest offshore site (yellow time series). As noted earlier, the wind is upwelling favourable during December to February (i.e. summer months), potentially leading to up-slope intrusions of nitrate rich water that may promote productivity. In winter when the Leeuwin Current lowers the pycnocline and the wind is less upwelling favourable, these intrusions are suppressed. This scenario appears to conform with the model output; wind direction is upwelling favourable in summer and early autumn (i.e. the dry; figure 4.5.13). The density profile indicates an upwelling situation in summer, with isopycnals sloping upwards toward the coast (figure 4.5.14). In winter the isopycnals have a downward slope characteristic of the Leeuwin Current situation, with isopycnals situated lower in the water column (e.g. the 1022.6 kg m^{-3} contour is up to 60 m deeper in winter). It is clear from figure 4.5.14 that the depths between 40 to 60 m are impacted by the up-slope intrusions during summer but not in winter, hence the seasonal variability observed at this depth in nitrate and productivity. The nitrate time series exhibits elevated levels during the dry season (figure 4.5.15) with much larger variability over the spring neap and semidiurnal tidal cycle. This variability is likely due to the upwelling favourable conditions interacting with the shallower mixed layers (and nutricline) in the wet season.

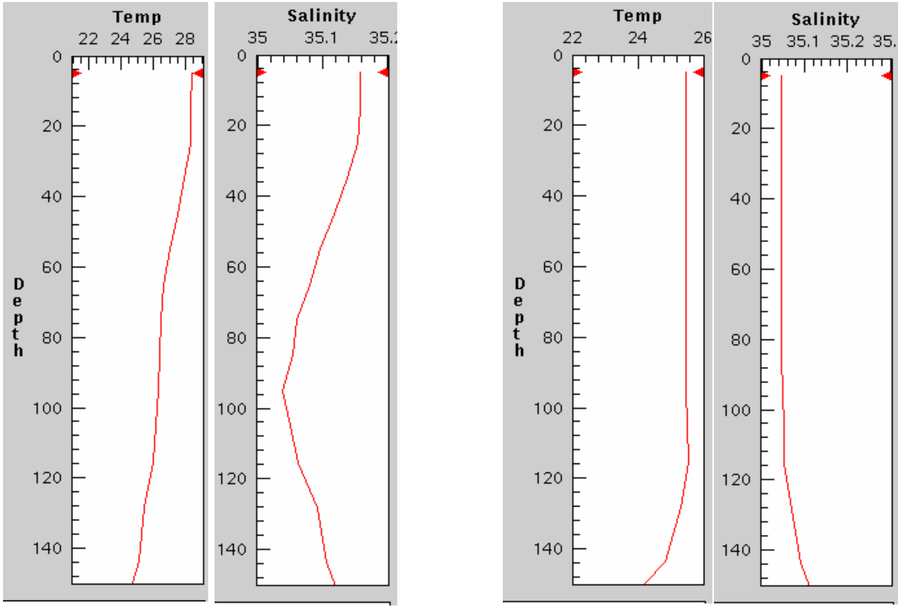

February September

Figure 4.5.11: Temperature (^{o}C) and salinity (psu) output from ACOM3.

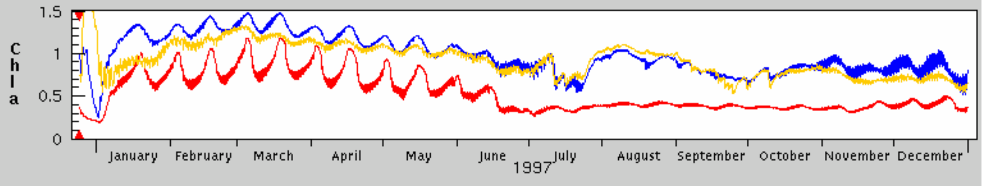

Figure 4.5.12 (a): Chlorophyll *a* concentration (mg m^{-3}) at 56 m: 1997.

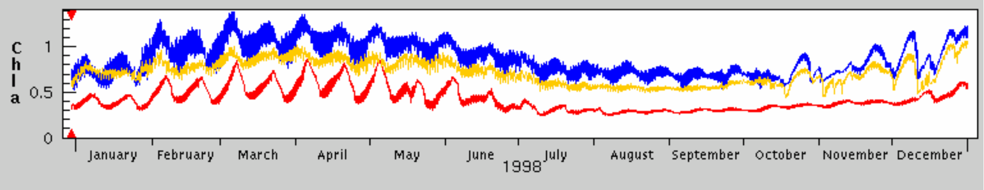

Figure 4.5.12 (b): Chlorophyll *a* concentration (mg m^{-3}) at 56 m: 1998.

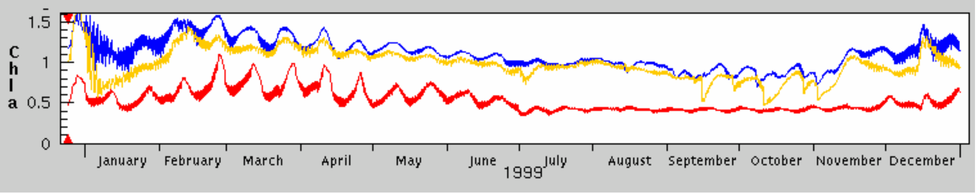

Figure 4.5.12 (c): Chlorophyll *a* concentration (mg m^{-3}) at 56 m: 1999.

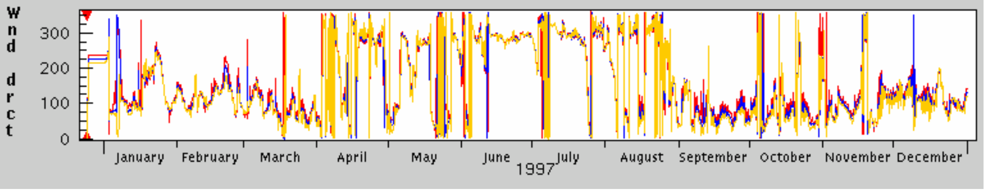

Figure 4.5.13: Wind direction for 1997 (ºT).70ºT~upwelling favourable; 250ºT~downwelling favourable.

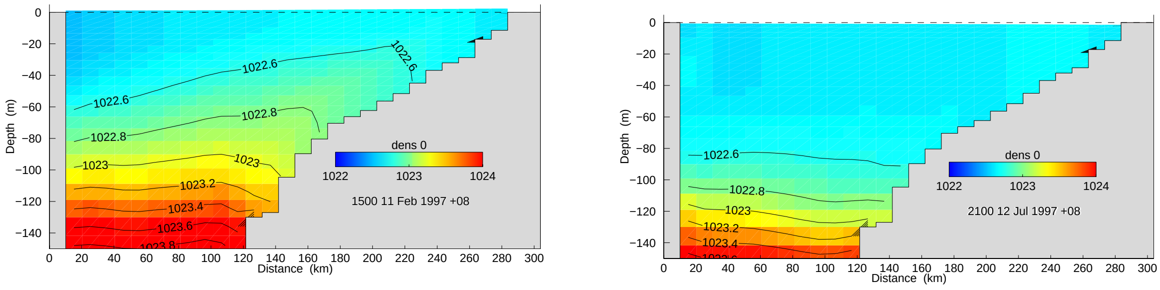

(a) Summer (b) Winter

Figure 4.5.14: Density section at the Port Hedland transect.

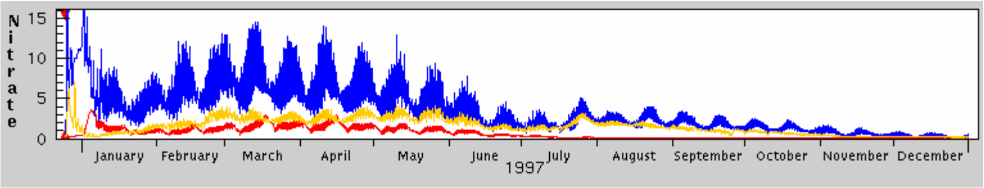

Figure 4.5.15 (a): Nitrate concentration (mg N m^{-3}) at 56 m: 1997.

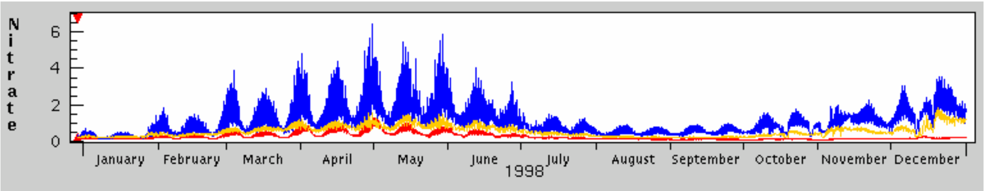

Figure 4.5.15 (b): Nitrate concentration (mg N m^{-3}) at 56 m: 1998.

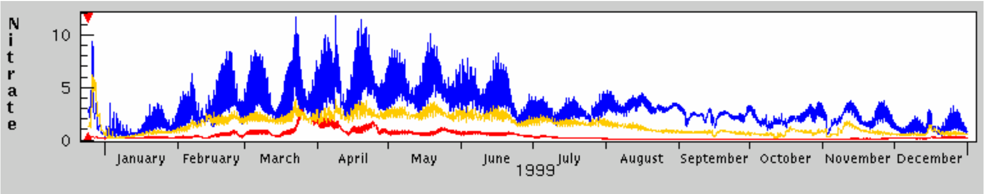

Figure 4.5.15 (c): Nitrate concentration (mg N m^{-3}) at 56 m: 1999.

4.6 Intraannual variability

A limited assessment of intraannual variability can be undertaken on the model output. Chlorophyll solutions show no dramatic variation from 1996 through 1999. Part of the reason for this is that although the physical parameters are allowed to evolve throughout this time period the major nutrient for productivity (nitrate) is not. This nutrient is forced on the open boundaries with the CARS climatology, which is repeatedly cycled for each year simulated, hence contains no intraannual variability.

4.7 Cyclones

A tropical cyclone was propagated through the domain in order to examine the impact of these systems on primary production. The first three months of 1995 were simulated, with Tropical Cyclone Bobby progressing through the region around 24 February. Tropical Cyclone Bobby enters the model domain in the northeast corner just after midnight on 23 February and proceeds in a southwest direction through the centre of the domain, exiting onto mainland Australia around midnight 25 February (figure 4.7.1). The timing of the cyclone passage provided approximately six weeks spin up of the biogeochemical model, in which a subsurface Chl*a* maximum was well established.

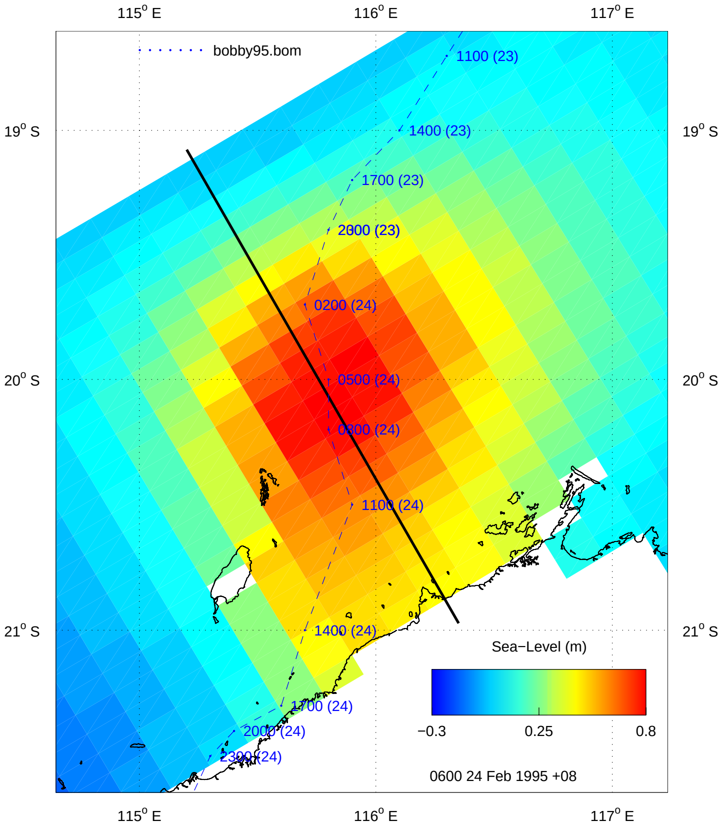

Figure 4.7.1: Path of Tropical Cyclone Bobby. The section line (black solid line) corresponds to the location of subsequent section illustrations (except for potential density and vertical advective flux). Tropical Cyclone Bobby intersects the section at 0600, 24 February.

The passage of a cyclone is characteristically associated with an increase in sea level, due to the inverse barometer effect. This sea level rise is of the order of 0.5 to 1 m (figure 4.7.2). The pycnocline responds in a scaled inverse manner to changes in sea level (Tomczak & Godfrey, 1994, p33) therefore a large increase in sea level results in a depression of the pycnocline under the centre of the cyclone. Figure 4.7.3 displays the potential density on 24 February at various stages of the cyclone progression. A downward displacement of the pycnocline of up to 50 m from its equilibrium position can be observed when the cyclone initially propagates over the region. Once the cyclone passes this perturbation results in a damped oscillation of the pycnocline in the form of a mode 1 baroclinic wave with a period of approximately 33 hours (figure 4.7.4) with the maximum upward displacement exceeding the initial downward displacement. Price (1981) documents this oscillation in temperature records measured below the mixed layer with near-inertial periods (the inertial period at 20^{o}S is ~35 hours). In addition, the large wind stress applied at the sea surface generates large velocity shear that promotes a deep mixed layer. Holloway (1983) reports that cyclones over the North West Shelf region are capable of generating deep mixed layers over the shelf but little vertical mixing is associated with the shelf break. This is observed in figure 4.7.5 where vertical diffusivities increase by an order of magnitude or more during the passage of the cyclone over the shelf region, with strong mixing to depths of ~70 m. The cyclonic circulation associated with tropical cyclones generates a zone of divergence at the cyclone centre which leads to upwelling in this region (Price, 1981). This potentially may transport nutrients into the surface layer. Holloway et al. (1985) estimate that this mechanism could sustain productivity for about nine days. Further from the cyclone path weak downwelling occurs.

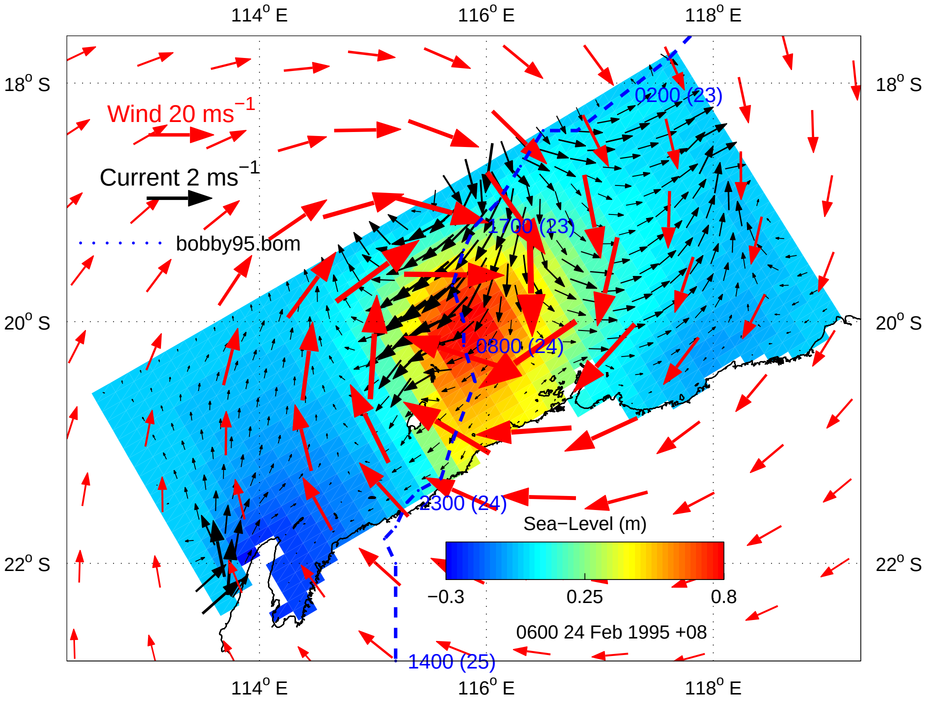

Figure 4.7.2 (a): Elevation and surface flow for Tropical Cyclone Bobby: 24 February 1995. The path of Tropical Cyclone Bobby is overlaid in blue.

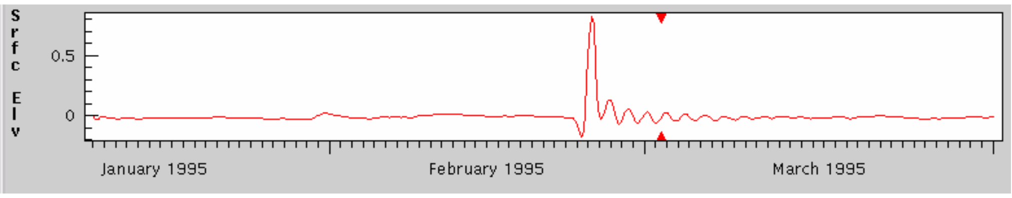

Figure 4.7.2 (b): Surface elevation (m) for 1995.

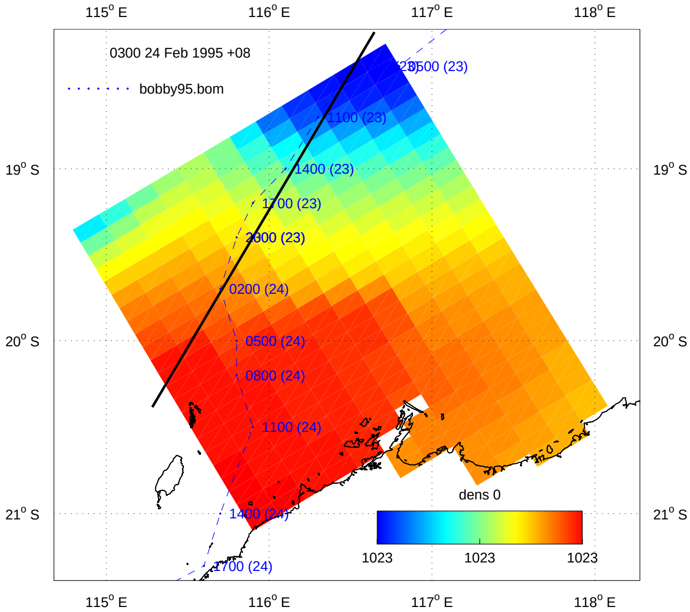

Figure 4.7.3 (a): Section orientation and cyclone passage for density sections. Note: 1800 hours corresponds to the cyclone centre approximately midway along the section.

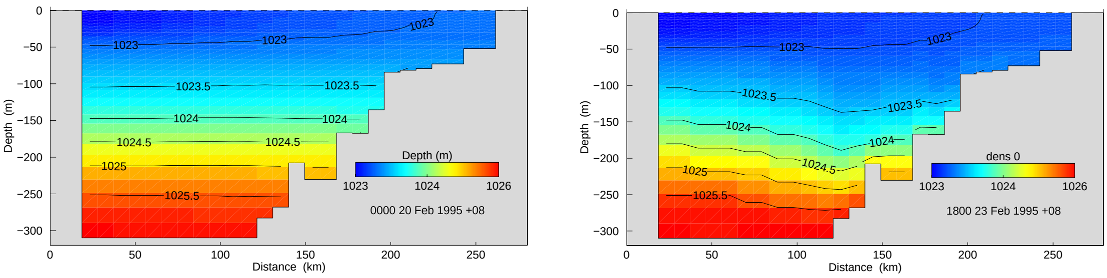

Pre-cyclone

During cyclone: 1800 hours

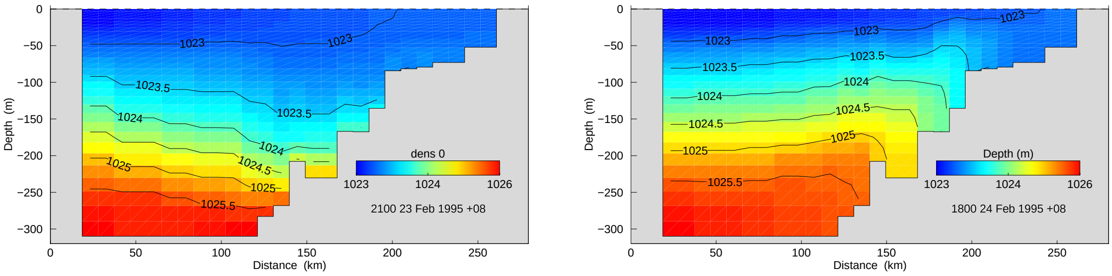

During cyclone: 2100 hours

Post-cyclone

Figure 4.7.3 (b): Potential density sections (kg m^{-3}).

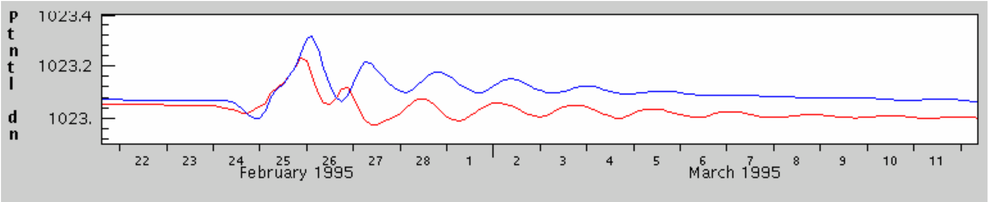

Figure 4.7.4: Potential density time series at the locations corresponding to the cyclone centre at 1400 (red) and 2000 (blue) hours, 23 February: 50 m depth.

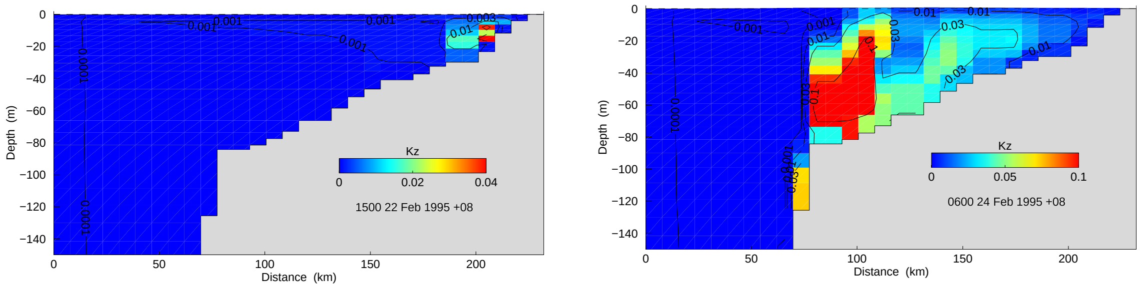

(a) Pre-cyclone

(b) During cyclone

Figure 4.7.5: Vertical diffusivity ($m^2\ s^{-1}$) along the section normal to the coast.

These physical mechanisms invoke two conflicting processes upon the nutrient dynamics. The deepening mixed layer and upwelling near the center tends to entrain more nitrate from below the nutricline into the surface layer, while the deepening pycnocline (and nutricline) acts to displace the zone of high nutrient concentration beyond the influence of the mixing. The net result is that productivity does not increase significantly for any length of time as a result of the passage of the cyclone. The surface chlorophyll response to the cyclone is minimal, consisting of a small increase peaking around 1500 26 February in two distinct zones (figure 4.7.6). The asymmetry in the surface response may be related to the SST bias observed during the passage of hurricanes (e.g. Price, 1981), although it is unclear why two zones exist in this case. This increase in Chl*a* concentration is small in comparison to the magnitudes encountered inshore during the spring neap cycle.

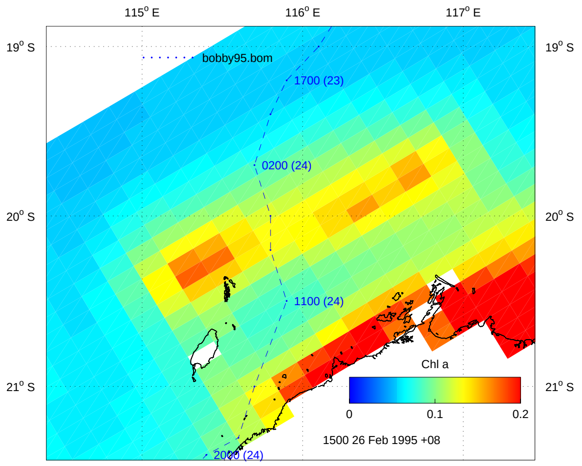

Figure 4.7.6 (a): Chl*a* (mg m^{-3}) with Tropical Cyclone Bobby track superimposed.

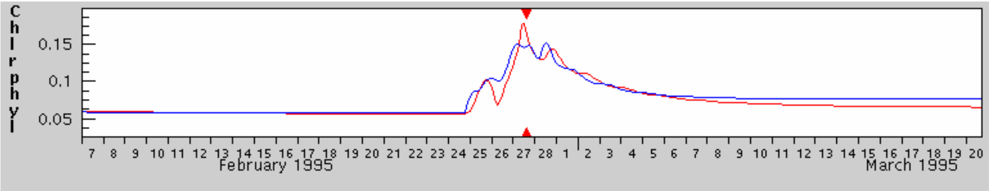

Figure 4.7.6 (b): Time series of Chl*a* concentration at the two centres in figure 4.7.6 (a). Red = left centre, blue = right centre.

The vertical diffusive flux of nitrate through 85 m initially exhibits a decrease in magnitude, followed by a distinct increase after the cyclone passes, with the post-cyclone flux being larger than pre-cyclone flux (figure 4.7.7). This flux also exhibits an oscillation in time, with a similar period to the nutricline oscillation (figure 4.7.8). The initial flux decrease indicates that the lowering of the nutricline negates the effect of increased mixing and actually decreases the overall diffusive flux. Once the cyclone has passed the nutricline begins to oscillate as a result of the initial perturbation, and when the nutricline is closer to the surface higher concentrations of nitrate are mixed upwards and the diffusive flux increases. Closer to the surface the diffusive flux is initially already small due to the nitrate depleted waters present and the initial decrease is absent; only an increase in the vertical flux observed after the cyclone has passed (figure 4.7.8 (a)). Deeper in the water column the initial decrease can be seen as the nutricline is lowered and post-cyclone fluxes are similar to pre-cyclone fluxes (figure 4.7.8 (c)).

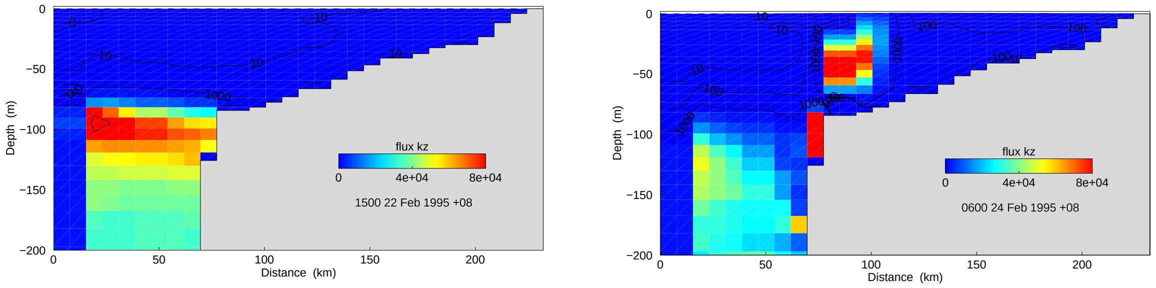

(a) Pre-cyclone (b) During cyclone

Figure 4.7.7: Vertical diffusive flux of nitrate (mg N s^{-1})

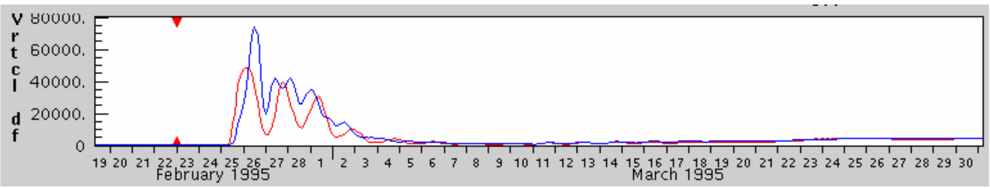

Figure 4.7.8 (a): Vertical diffusive flux of nitrate through 62 m (mg N s^{-1}). The red and blue curves are located at distances of 65 km and 95 km respectively from the shelf.

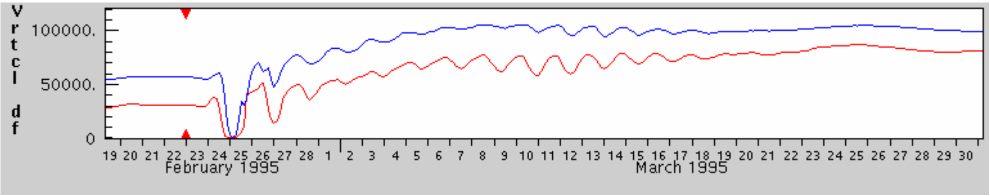

Figure 4.7.8 (b): Vertical diffusive flux of nitrate through 85 m (mg N s^{-1}). The red and blue curves are 25 km and 55 km respectively from the shelf.

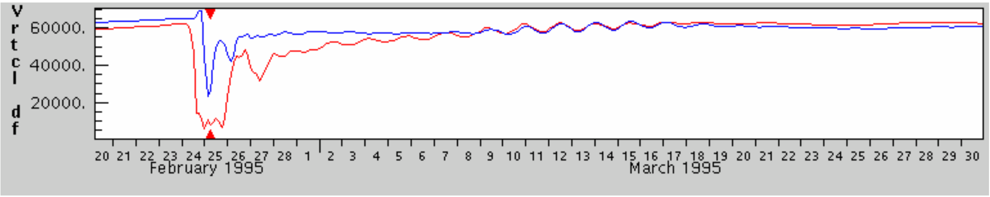

Figure 4.7.8 (c): Vertical diffusive flux of nitrate through 114 m (mg N s^{-1}). The red and blue curves are 15 km and 45 km respectively from the shelf.

The vertical advective flux of nitrate also undergoes a large oscillation corresponding to the heaving of the nutricline (figure 4.7.9), with downward fluxes beneath the cyclone centre and upward fluxes subsequent to the cyclone passage. The initial downward fluxes are of smaller magnitude than the upward fluxes, presumably because under the cyclone the vertical motion due to downward displacement of the pycnocline competes with upwelling due to divergence at the centre. The maximum downward flux under the cyclone center is located deeper in the water column than the post-cyclone upward flux. Both upward and downward fluxes are several orders of magnitude greater than the mean vertical fluxes of ~2.5 x 10^5 displayed in section 4.3. These advective fluxes exhibit an oscillation about the pre-cyclone levels after the cyclone has passed (figure 4.7.10). Depths shallower than the SCM (i.e. < ~90 m) show a very small decrease in the advective flux during the cyclone passage (due to lack of nitrate in this region) followed by a significant increase once the cyclone has passed (figure 4.7.10 (a,b)). The deeper layers show a small decrease in the advective flux corresponding to the depression of the nutricline as the cyclone passes, followed by large increases after the cyclone has passed (figure 4.7.10 (c)). The vertical advective fluxes reach their pre-cyclone levels within three to four days of the cyclone passage.

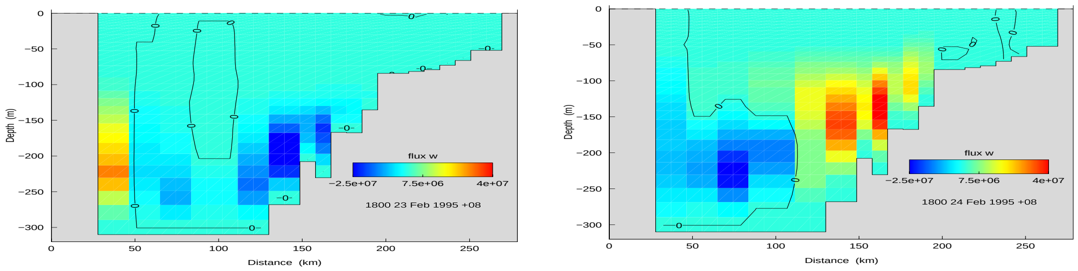

(a) During cyclone (b) Post-cyclone

Figure 4.7.9: Vertical advective flux of nitrate through 85 m (mg N s^{-1}). The section in this case is that corresponding to that depicted in figure 4.7.3 (a), where the cyclone centre on 1800 23 February is midway along the section.

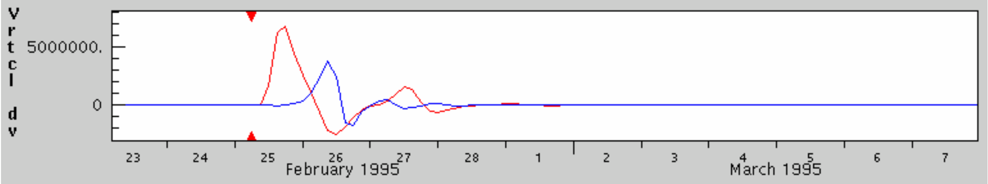

Figure 4.7.10 (a): Vertical advective flux of nitrate through 62 m (mg N s^{-1}). The red and blue curves are 65 km and 95 km respectively from the shelf.

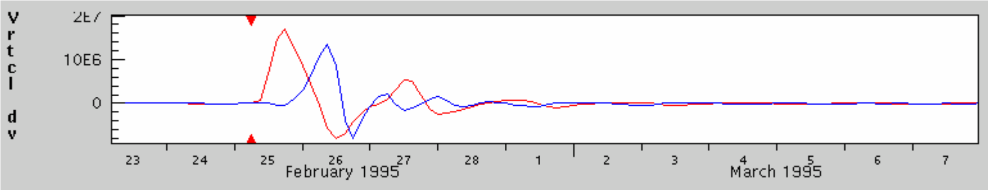

Figure 4.7.10 (b): Vertical advective flux of nitrate through 85 m (mg N s^{-1}). The red and blue curves are 25 km and 55 km respectively from the shelf.

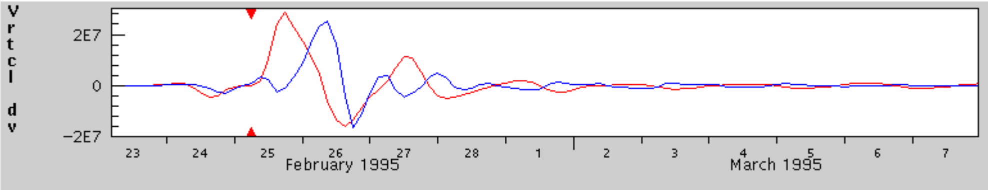

Figure 4.7.10 (c): Vertical advective flux of nitrate through 114 m (mg N s^{-1}). The red and blue curves are 15 km and 45 km respectively from the shelf.

The net effect of these fluxes on nitrate concentration in the pycnocline zone is to decrease the concentration during the cyclone passage then significantly increase the concentration after the cyclone has passed (figure 4.7.11). The nitrate concentration during the cyclone passage (24 Feb) actually decreases to zero before increasing. The increase in nitrate availability after the cyclone has passed results in an increase in primary productivity in the SCM (figure 4.7.12). Greater increases are observed further offshore. After about a month the SCM concentration reverts to the pre-cyclone levels. A section time series of nitrate and Chl*a* during the cyclone passage is displayed in figure 4.7.13.

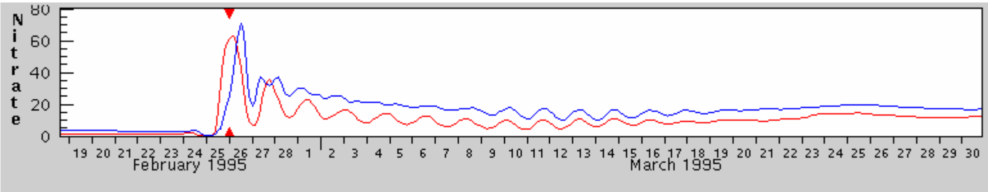

Figure 4.7.11: Nitrate (mg N m^{-3}) at 85 m. The red and blue curves are 25 km and 55 km respectively from the shelf.

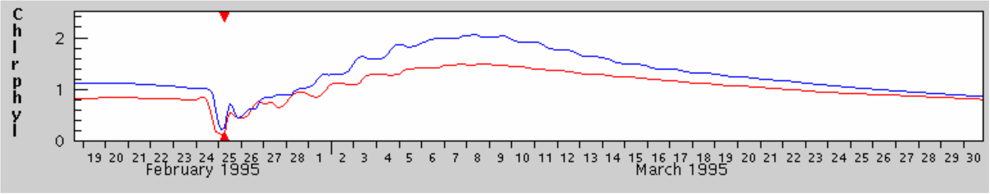

Figure 4.7.12: Chl*a* (mg m^{-3}) at 85 m. The red and blue curves are 25 km and 55 km respectively from the shelf.

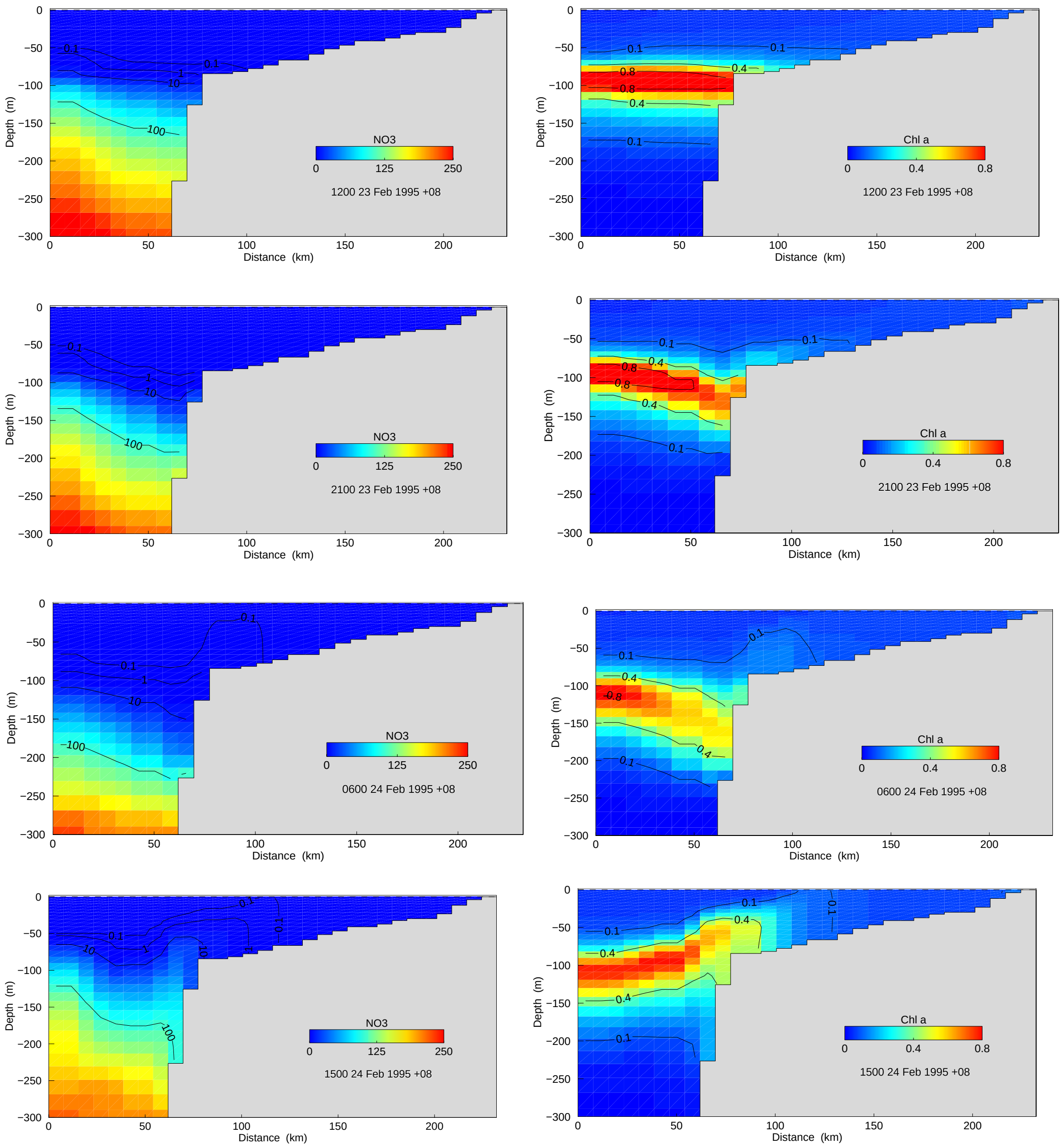

a) Nitrate (mg N m^{-3})

(b) Chl*a* (mg m^{-3})

Figure 4.7.13: Nitrate and Chl*a* during Tropical Cyclone Bobby.

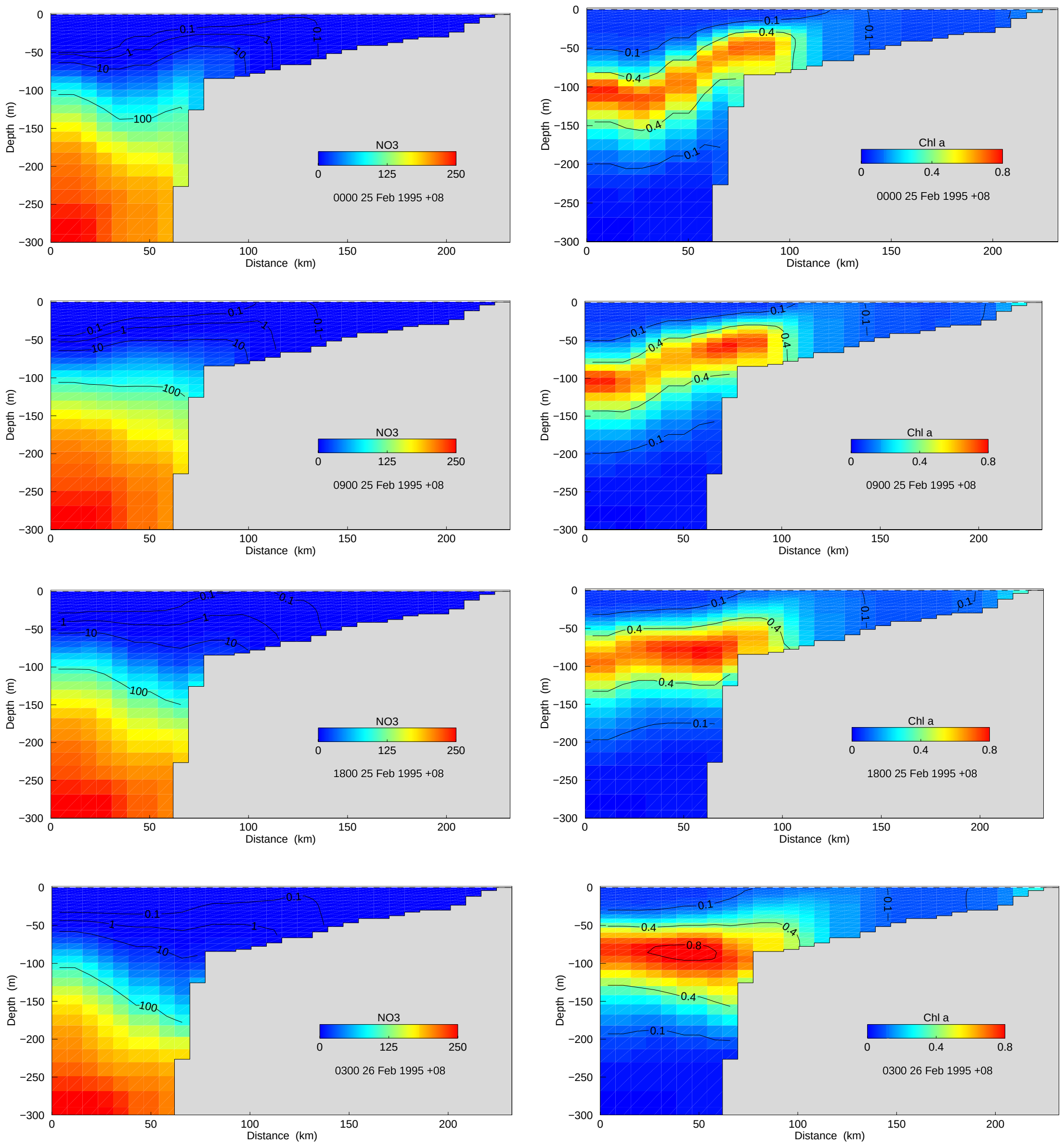

(a) Nitrate (mg N m^{-3})

(b) Chla (mg m^{-3})

Figure 4.7.13 continued: Nitrate and Chl*a* during Tropical Cyclone Bobby.

5. CONCLUSIONS

Primary productivity on the North West Shelf region is maximum in a distinct band lying below the mixed layer (the subsurface chlorophyll maximum, SCM). Chlorophyll a concentrations within the SCM are approximately 1 to 1.5 mg Chl*a* m^{-3}, and less than 0.5 mg Chl*a* m^{-3} at the surface. There exists very little nitrogen in the surface mixed layer, but below the SCM nitrate increases steadily up to ~250 mg N m^{-3} at depths of around 300 m. The model phytoplankton composition in the SCM is predominantly the larger size classes, e.g. diatoms. Nano phytoplankton dominate within the mixed layer with large turnover rates but low biomass, utilising predominantly recycled nitrogen (ammonia). Large zooplankton graze on the larger phytoplankton classes, and consequently large zooplankton biomass is also maximum in the SCM. Micro zooplankton graze on nano phytoplankton and have relatively larger biomass in the mixed layer than the large size class.

The SCM is maintained by a balance between phytoplankton nitrate uptake fed by fluxes into the SCM and nitrate export in particulate form. The SCM exists at a depth where light and nitrogen limited phytoplankton production is such that SCM phytoplankton uptake, organic N export as sinking particulates, balance vertical nitrate fluxes. A decrease in light availability or increase in nitrogen flux will move the SCM closer to the surface, and vice versa. At equilibrium the production of phytoplankton balances consumption by zooplankton. Any change in the grazing of zooplankton results in a change in production, regulated by light limitation via vertical displacement of the SCM in the water column.

The supply of nitrate into the SCM appears to be primarily due to vertical processes. The largest (temporal) mean flux of nitrate, or largest constant background flux, is due to vertical diffusive processes. Vertical advection is capable of locally increasing nitrate flux into the SCM. The horizontal advective fluxes of nitrate into the SCM (i.e. above ~80 m depth) do not appear to contribute much to sustaining the SCM but are important for maintaining the deep pool of nitrate. A net supply of nitrate is delivered to the SCM through the north-eastern and offshore open boundaries, but this is largely lost through the south-western open boundary.

The SCM and surface chlorophyll signature undergo variability on time scales of the spring neap tidal cycle. Greater turbidity during the spring can decrease light availability, allowing the SCM to become shallower. Mixing to the surface under these conditions pushes the zone of maximum surface biomass further offshore. During the neap tide the SCM lies at constant depth and intersects the continental slope at depths 70 to 80 m, acting as a barrier that strips any nitrate advected into the shallow coastal zone. As the SCM shallows during the spring tide a pathway is created for nitrate to enter the coastal zone (under favourable advective conditions). The bypassing of the SCM under these conditions can elevate nitrate in depths less than 40 m.

The region where top and bottom boundary layers overlap creates a well mixed water column from the surface to sea floor; the largest vertical mixed zone possible. Where the SCM intersects this zone, mixing to the surface results in the largest surface Chl*a* concentration. During spring tides the mixing in this zone is more vigorous and the surface Chl*a* concentration is consequently greater. The north-eastern side of the domain is associated with the least steep bottom slope, and is thus the region of greatest variability of boundary overlap zone, hence of cross shelf surface phytoplankton distribution. Generally, wide flat shelves will be associated with this characteristic.

Seasonal variability of biomass is evident, where the SCM is more distinct with a surface signature closer inshore in the wet season, and the SCM more dispersed with surface signature offshore in the dry. These differences stem from changes in mixed layer depth, and a corresponding shift offshore of the boundary layer overlap zone. The mixed layer deepening originates from processes captured by the global hydrodynamic model into which the biogeochemical model is nested, and is attributed to atmospheric forcing, particularly zonal wind stress and the surface heat flux. The summer and autumn months are characterised by upwelling favourable winds, which in the absence of the pycnocline lowering effect of the Leeuwin Current acts to bring nutrients into waters of depth 40 to 60 m and enhance productivity. Larger variability on time scales of the semidiurnal tide and spring neap cycle are observed in summer and autumn, probably due to the combined effects of a shallower mixed layer and upwelling favourable conditions.

The passage of tropical cyclones in the model increases primary productivity at the surface and in the SCM by small amounts. Mixing increases in strength and penetrates deeper under the cyclone, and elevation rises as a result of the inverse barometer effect, with an associated baroclinic adjustment of the pycnocline downwards. This downward adjustment also moves the nutricline downward, beyond the zone of increased mixing which results in little new nitrate being mixed to the surface. After the cyclone has passed, however, vertical motions result in significant upward fluxes of nitrate which leads to increases in nitrate concentration and productivity above and within the SCM. These elevated levels oscillate at the near inertial period and Chl*a* reverts to pre-cyclone levels within the SCM on time scales of about one month. Nitrate concentrations in the SCM and surface Chl*a* remain slightly elevated in comparison to pre-cyclone levels after one month.

REFERENCES

Baird, M. E., S. J. Walker, B. B. Wallace, I. T. Webster and J. S. Parslow (2003) The use of mechanistic descriptions of algal growth and zooplankton grazing in an estuarine eutrophication model. *Est. Coast. Shelf. Sci.*, 56, 685-695.

Burchard, H., K., Bolding and M.R. Villarreal (1999) GOTM, a general ocean turbulence model. Theory implementation and test cases. Technical Report EUR 18745EN, European Commission, 103pp.

Heyward, A.J., A.T. Revill and C.R. Sherwood (2006) Review of research and data relevant to marine environmental management of Australia's North West Shelf. NWSJEMS Technical Report No. 1. *CSIRO Marine and Atmospheric Research*.

Holloway, P.E, (1983) Tropical cyclone effects in shallow seas. In 'Proceedings: Inaugural Great Barrier Reef Conference'. (Eds J.T. Baker, R.M. Carter. P.W. Sammarco and K.P. Stark). Pp 441-446. James Cook University Press. Townsville.

Holloway, P.E, S.E. Humphries, M. Atkinson and J. Imberger (1985) mechanisms for nitrogen supply to the Australian North West Shelf. *Aust. J. Mar. Freshw. Res.*, 36, 753-764.

Holloway, P.E. and H.C. Nye (1985) Leeuwin Current and wind distributions on the southern part of the Australian Nort West Shelf between January 1982 and July 1983. *Aust. J. Mar. Freshw. Res.*, 36, 123-137.

Mackey, D.J., J. Parslow, H.W. Higgins, F.B. Griffiths, B. Tilbrook (1997) Phytoplankton productivity and the carbon cycle in the western Equatorial Pacific under ENSO and non-ENSO conditions. *Deep-Sea Res.,* I 44, 1239-1253.

Murray, A.G. and J. S. Parslow (1999) Modelling of nutrient impacts in Port Phillip Bay - a semi-enclosed marine Australian ecosystem. *Mar. Freshw. Res,* 50, 597-611.

Price, J.F. (1981) Upper ocean response to a hurricane. *J. Phys. Oceanogr.* 11, 153-175.

Ridgway K. R., J. R. Dunn and J. L. Wilkin, (2002) Ocean interpolation by four-dimensional least squares -Application to the waters around Australia, *J. Atmos. Ocean. Tech.*, **19**, 1357-1375.

Schiller, A. (2003) Effects of explicit tidal forcing in an OGCM on the water-mass structure and circulation in the Indonesian throughflow region. *Ocean Modelling*, 6, 31-49.

Tanter, D.J. and G.S. Leech (1987) Factors influencing the standing crop of phytoplankton on the Australian Northwest Shelf seaward of the 40m isobath. *Continental Shelf Research*, 7(2), 115-133.

Tomczak, M. and S. J. Godfrey (1994) Regional oceanography: an introduction. Pergamon Press, Oxford.

APPENDIX A: PARAMETER VALUES USED IN THE BIOGEOCHEMICAL MODEL

Parameter	Description	value
ZL_E	(Growth efficiency, large zooplankton)	0.38
ZS_E	(Growth efficiency, small zooplankton)	0.38
PhyL_mL	(Natural (linear) mortality rate, large phytoplankton (in sediment))	0.14 d^{-1}
PhyS_mL	(Natural (linear) mortality rate, small phytoplankton (in sediment))	0.14 d^{-1}
MPB_mQ	(Natural (quadratic) mortality rate, microphytobenthos)	3×10^{-5} d^{-1} (mg N m^{-3})$^{-1}$
ZL_mQ	(Natural (quadratic) mortality rate, large zooplankton)	5×10^{-4} d^{-1} (mg N m^{-3})$^{-1}$
ZS_mQ	(Natural (quadratic) mortality rate, small zooplankton)	0.005 d^{-1} (mg N m^{-3})$^{-1}$
ZL_FDG	(Fraction of growth inefficiency lost to detritus, large zooplankton)	0.5
ZL_FDM	(Fraction of mortality lost to detritus, large zooplankton)	0.5
ZS_FDG	(Fraction of growth inefficiency lost to detritus, small zooplankton)	0.25
ZS_FDM	(Fraction of mortality lost to detritus, small zooplankton)	0.5
F_LD_RD	(Fraction of labile detritus converted to refractory detritus)	0.2
F_LD_DOM	(Fraction of labile detritus converted to dissolved organic matter)	0.05
NtoCHL	(Nitrogen:Chlorophyll A ratio in phytoplankton by weight)	7.0
k_w	(Background light attenuation coefficient)	0.03 m^{-1}
k_DOR_N	(DOR_N-specific light attenuation coefficient)	9×10^{-4} m^{-1} (mg N m^{-3})$^{-1}$
k_DetL	(Detrital N-specific light attenuation coefficient)	0.001 m^{-1} (mg N m^{-3})$^{-1}$
k_TSS	(TSS-specific light attenuation coefficient)	30.0 m^{-1} (kg m^{-3})$^{-1}$
k_C_fw	(CDOM attentuation coefficient of freshwater)	0.0 m^{-1}
k_SWR_PAR	(fraction of incident solar radiation that is PAR)	0.43
Q10	(Temperature coefficient for rate parameters)	2.0
PLumax	(Maximum growth rate of PL at Tref)	1.25 d^{-1}
PLrad	(Radius of the large phytoplankton cells)	10e-06 m
PLabsorb	(Absorption coefficient of a PL cell)	50000 m^{-1}
PLsvel	(Settling velocity of PL)	2×10^{-5} ms^{-1}
PLSh	(Sherwood number for the PS dimensionless)	1
PLn	(Number of limiting nutrients)	3
PSumax	(Maximum growth rate of PS at Tref)	1.25 d^{-1}
PSrad	(Radius of the small phytoplankton cells)	2.5e-06 m
PSabsorb	(Absorption coefficient of a PS cell)	50000 m^{-1}
PSSh	(Sherwood number for the PL dimensionless)	1
PSsvel	(Settling velocity of PS)	0 m s^{-1}
MBumax	(Maximum growth rate of MB at Tref)	0.35 d^{-1}

Parameter	Description	value
MBrad	(Radius of the MB cells)	1.0e-05 m
MBabsorb	(Absorption coefficient of a MB cell)	50000 m^{-1}
MBSh	(Sherwood number for the PL dimensionless)	1
MBsvel	(Settling velocity of MB)	5.79x10^{-5} m s^{-1}
ZSumax	(Maximum growth rate of ZS at Tref)	3 d^{-1}
SGumax	(Maximum growth rate of SG at Tref)	0.1 d^{-1}
SGaA	(Nitrogen specific absorbtion cross section of SG)	1x10^{-4} m^{2} mg N^{-1}
ZSrad	(Radius of the small zooplankton cells)	12.5e-06 m^{-1}
ZSswim	(Swimming velocity for small zooplankton)	2.0e-4 m s^{-1}
ZLumax	(Maximum growth rate of ZL at Tref)	0.1 d^{-1}
ZLrad	(Radius of the large zooplankton cells)	500.0e-06 m^{-1}
ZLswim	(Swimming velocity for large zooplankton)	1.0e-3 m s^{-1}
TKEeps	(TKE dissipation in water column)	1.0e-6 m^{2}s^{-3}
cf	(drag coefficient of the benthic surface)	0.005
Ub	(velocity at the top of the ben. bound. layer)	0.1 m s^{-1}
ks	(sand-grain roughness of the benthos)	0.1 m
F_RD_DOM	(fraction of refractory detritus that breaks down to DOM)	0.05
r_floc	(rate at which TSS floculates above 10 PSU)	0.01 d^{-1}
r_DetPL	(Breakdown rate of labile detritus at 106:16:1)	0.1 d^{-1}
r_DetBL	(Breakdown rate of labile detritus at 550:30:1)	0.1 d^{-1}
r_RD	(Breakdown rate of refractory detritus)	0.0036 d^{-1}
r_DOM	(Breakdown rate of dissolved organic matter)	0.00176 d^{-1}
Tref	(Reference temperature)	15.0 ^{o}C
Plank_resp	(Respiration as a fraction of umax)	0.025
Benth_resp	(Respiration as a fraction of umax)	0.025
r_nit_wc	(Maximal nitrification rate in water column)	0.2 d-1
R_0_T15	(Sediment net respiration rate at which nitrification is zero)	200 mg N m^{-2} day^{-1}
R_D_T15	(Sediment net respiration rate at which denitrification is maximum)	10 mg N m^{-2} day^{-1}
Dmax	(Maximum denitrification efficiency)	0.7
mum_MA_T15	Maximum macroalgae growth rate	0.1 d^{-1}
KI_MA_T15	Light saturation for macroalgae	5 W m^{-2}
KN_MA	Half saturation constant for macroalgae growth on DIN	20 mg N
MAmax	Maximum macroalgae biomass	1e4 mg N m^{-2}
mL_MA_T15	Natural (linear) macroalgae mortality rate	0.00275 d^{-1}
mS_MA_T15	Bottom stress dependent macroalgae mortality rate	0 d^{-1} (N m^{-2})$^{-1}$
mum_SG_T15	Maximum seagrass growth rate	0.05 d^{-1}
KI_SG_T15	Light saturation for seagrass	60 W m^{-2}
KN_SG	Half saturation constant for seagrass growth on DIN	5 mg N
SGmax	Maximum seagrass biomass	2000 mg N m^{-2}
mL_SG_T15	Natural (linear) seagrass mortality rate	0.00275 d^{-1}
mS_SG_T15	DIN dependent seagrass mortality rate	0 d^{-1} (mg N m^{-3})$^{-1}$

ACKNOWLEDGMENTS

The following people and agencies have contributed significantly to the Study through the provision of technical expertise and advice, and historical data and information. The Study partners gratefully acknowledge their contribution.

Western Australian State agencies
Department of Environment and Conservation (Department of Conservation and Land Management and Department of Environment)
Department of Fisheries
Department of Industry and Resources (Department of Mineral and Petroleum Resources)
Department of Land Information
Department for Planning and Infrastructure (Department of Transport)
Pilbara Tourism Association
Shire of Roebourne
Town of Port Hedland
Tourism Western Australia
Western Australian Land Information System
Western Australian Museum

Commonwealth agencies
Australian Institute of Marine Science
Geoscience Australia (formerly Australian Geological Survey Organisation)

Consultants
Cognito Consulting
David Gordon International Risk Consultants
METOCEAN Engineers (formerly Weather News International, Perth)
Oceanica (formerly DA Lord and Associates)

Industries
Australian Petroleum Production Exploration Association (APPEA)
Apache Energy
BHP Petroleum
Chevron Australia
Dampier Salt
Hamersley Iron
Mermaid Marine
Woodside Energy

Individuals
Clay Bryce
Graham Cobby
Nick D’Adamo
Mike Forde
David Gordon
Andrew Heyward
Barry Hutchins
Bryan Jenkins
Di Jones

Ian LeProvost
Ray Masini
Mike Moran
Steve Newman
Eric Paling
Kelly Pendoley
Bob Prinz
Chris Simpson
Shirley Slack-Smith
Di Walker

Reviewers
Jim Greenwood
Mike Herzfeld

Editorial and publishing
Louise Bell – Graphics/cover design
Lea Crosswell – Webpage design
Rob McKenzie – Editor
Diana Reale – Webpage design
Linda Thomas – Editorial consultant/layout and design
Helen Webb – Editorial consultant/Project Manager

Front cover photos courtesy of:
Centre – Coral reef ecosystem, WA Museum, Clay Bryce
Aquaculture pearls, Department of Fisheries WA
Recreational fishing, Department of Fisheries WA, Jirri Lockman
Offshore petroleum platform, Woodside Energy Ltd
Commercial Fishing, Department of Fisheries WA
Tourism, CSIRO
Coastal development aerial photos, Hamersley Iron Pty Ltd